**Development of Two-dimensional Stark Spectroscopy for the Investigation of**

**Photosynthetic Charge Separation**


by


Anton D. Loukianov




A dissertation submitted in partial fulfillment
of the requirements for the degree of
Doctor of Philosophy
(Biophysics)
in The University of Michigan
2017




Doctoral Committee:

        Professor Jennifer P. Ogilvie, Chair
        Professor Ari Gafni
        Professor Eitan Geva
        Professor Kevin J. Kubarych

Anton D. Loukianov

[aloukian@umich.edu](mailto:aloukian@umich.edu)

http://orcid.org/0000-0002-1863-1033

*To my grandfather, Vladimir.*

# ACKNOWLEDGEMENTS

<p style="text-align:center">**TABLE OF CONTENTS**</p>

# LIST OF FIGURES

# LIST OF TABLES

# LIST OF APPENDICES

$S_{\text{NR}}^{(3)}$        2D non-rephasing signal $[48, 84, 85]$.

$S_{\text{2d}}^{(3)}$        2D real absorptive signal $[62, 85]$.

$S_{\text{RE}}^{(3)}$        2D rephasing signal $[48, 84, 85]$.

$S_{\text{TG}}^{(3)}$        transient-grating signal $[84]$.

$\rho$        charge density $[18]$.

$k_B$        Boltzmann constant $[31]$.

$\boldsymbol{J}$        current vector $[18]$.

$U_{\text{mat}}^{\dagger}$        density matrix space backward propagator $[37]$.

$U_{\text{mat}}$        density matrix space forward propagator $[37, 38]$.

$\hat{\rho}$        density operator $[17, 18, 29, 31\text{–}38]$.

$\hat{\rho}^{\text{I}}$        density operator in interaction picture $[34, 36]$.

$\boldsymbol{D}$        electric displacement $[18]$.

$\widehat{\boldsymbol{E}}_{\omega_s}$        complex electric-field amplitude $[22]$.

$E$        cartesian electric field component $[35\text{–}37]$.

$\widehat{\boldsymbol{E}}_{\omega_s}$        electric-field envelope centered near $\omega_s$ $[25]$.

$\widehat{\boldsymbol{E}}$        complex electric-field envelope $[22\text{–}25]$.

$\boldsymbol{F}$     local electric field [94].

$\boldsymbol{A}_{\omega_s}$     amplitude of electric field plane-wave [25].

$\boldsymbol{E}$     electric field vector [18–24, 28, 30, 31, 36, 43, 49–51, 56, 59, 61, 76, 79, 94].

$\boldsymbol{\epsilon}$     dielectric tensor [18, 21, 22].

$\epsilon_0$     vacuum electric permittivity [18–20, 23, 36–38].

$\boldsymbol{P}$     electric polarization vector [17–21, 23–25, 28, 29, 35–37, 43, 44].

$\widehat{\boldsymbol{P}}$     complex electric-polarization envelope [23, 25].

$\boldsymbol{P}^{(\mathrm{NL})}$     polarization components nonlinear in the incident field [23–25, 28].

$\boldsymbol{e}$     electric polarization vector of unit magnitude [27, 28, 38, 43, 46, 47, 56].

$\mathrm{e}$     electric polarization vector component [36, 37, 44].

$\boldsymbol{\chi}$     electric susceptibility tensor [20–24, 28, 51, 77].

$\widehat{Q}$     element of polarization operator [35–39, 41, 46, 51].

$\mathcal{E}$     energy [55–57, 94, 135–137].


$\widehat{H}$     a general system Hamiltonian [29–31, 39, 40, 49, 55, 56].

$\widehat{H}_{\mathrm{I}}$     interaction Hamiltonian [30, 40, 56].

$\widehat{H}_0$     time-independent system Hamiltonian [30, 31, 34, 55].


$S^{(1)}$     linear absorptive signal [62].

$\mathscr{L}_{\mathrm{int}}$     Liouville space interaction superoperator [31, 32, 34].

$\mathscr{L}_{\mathrm{int}}^{\mathrm{I}}$     Liouville space interaction superoperator in interaction picture [34, 36].

$\mathscr{L}_{\mathrm{mat}}$     Liouville space material superoperator [31–33].

$\mathscr{L}$     Liouvillian operator [31].

$\mathscr{U}_{\mathrm{mat}}^{\dagger}$     Liouville space backward propagator [33, 34].

$\mathcal{U}_{\mathrm{mat}}$      Liouville space forward propagator [32–34, 36, 37].

$\boldsymbol{H}$      magnetic field [18].

$\boldsymbol{B}$      magnetic induction [18].

$\boldsymbol{\mu}$      magnetic permiability tensor [18].

$\mu_0$      vacuum magnetic permiability [18, 19, 21, 23–25].

$\boldsymbol{M}$      magnetic polarization vector [18].

$\mathbb{K}$      anharmonic coupling matrix [55].

$\mathbb{J}$      harmonic coupling matrix [55].

$\hat{B}$      excitonic lowering (annihilation) operator in second quantization formalism [55, 56].

$\hat{\boldsymbol{\alpha}}$      polarizability operator [49–51, 56, 57, 61, 63, 64, 67, 72, 94, 98, 100, 140–142].

$\hat{Q}$      quantum-mechanical polarization operator [17, 28–31, 35, 36, 46, 47].

$\boldsymbol{r}$      cartesian position vector [22–25, 28, 29, 43].

$\hbar$      reduced Planck constant [29].

$\boldsymbol{R}$      time-domain material response function [17, 20, 21, 28, 38, 39, 44].

$R$      time-domain material response function component [36–38, 41, 51].

$\boldsymbol{E}_{\mathrm{s}}$      signal electric field [17, 20–23, 27–29].

$E_{\mathrm{s}}$      component of the signal electric field [27].

$c$          the speed of light in vacuum $[22, 24]$.

$\hat{\boldsymbol{\mu}}$          static dipole operator $[49\text{--}51, 56\text{--}58, 61, 63\text{--}66, 68\text{--}72, 94, 98, 116]$.

$T$          temperature of the bath $[31]$.

$\boldsymbol{k}$          wave vector $[38, 43\text{--}45, 48, 79\text{--}82]$.

$\boldsymbol{k}_s$          signal wave vector $[22, 25, 45, 46]$.

**ABSTRACT**

Charge transfer reactions are critical for the efficient function of photosynthetic enzymes. With growing energy demand, understanding the design principles of natural photosynthetic systems is important to aid efforts in developing sustainable energy sources that do not add to the carbon-dioxide burden of the atmosphere. Photosystem II is particularly interesting because it is an ideal model for artificial photovoltaic devices for energy applications: it is efficient, stabilizes the energized state for useful times, and is resilient to photo-damage. Despite decades of study, the mechanism of primary charge separation in this system is still under debate, primarily because the charge-transfer intermediates involved in these reactions do not have strong spectral signatures and are extremely short-lived.

I have developed a novel spectroscopy method called two-dimensional electronic Stark spectroscopy (2DESS) for the study of fast processes involving the movement of charge in photosynthetic proteins. It combines the high sensitivity of Stark spectroscopy to charge-transfer reactions and the high temporal and spectral resolution of two-dimensional electronic spectroscopy. In collaboration with Darius Abramavicius at Vilnius University in Lithuania, I simulated a charge-transfer dimer system similar to the "special-pair" chlorophylls found in PSII RC thought to be involved in the primary charge-separation process in this system. Based on these simulations, I demonstrated that the 2DESS and Stark spectra for CT states in the PSII do not follow typical Liptay models. There is also evidence to suspect that the parameters used to model the PSII is incorrect. I then demonstrated the experimental technique on an organic polymer often used for

photovoltaic applications, observing first-derivative lineshapes consistent with predictions. Following this demonstration, I observed spectral signatures consistent with charge-separation of the PSII RC. Work is underway to extend the simulations to a more complete model system, as well as utilize the experimentally-obtained data to verify proposed models of charge-separation in the PSII RC.

In combination with other spectroscopy techniques, 2DESS will allow us to obtain a complete description of the initial charge-separation kinetics in photosystem II and may suggest ways to mimic its extraordinary efficiency. We expect this technique to be applicable to other systems such as organic photovoltaics, in which the role of CT states is unclear or is hard to trace.

# CHAPTER 1

## Charge-transfer Reactions in Nature

### *1.1 Introduction*

As the global standard of living increases, the energy demand is rising steadily. Over the next century, the majority of the global energy demand will be in developing countries, and at this point is directly linked to increase in trade and health of the global economy[1]. Historically, the majority of this demand has been met with coal and gas energy, both non-renewable and highly polluting sources that pose significant environmental risks if their use continues unabated. In particular, the fraction of carbon-dioxide $CO_2$ in the atmosphere has been recognized as a major source of global warming which has been linked to industrial activity. Thus a major challenge of our times is the development of a environmentally benign, scalable, and efficient source of energy to meet growing demand.

Solar energy is the most sustainable and renewable source to meet growing energy demand, and many technologies have been developed to efficiently harvest it. Apart from powering industrial activity, it also provides the driving energy for the production of biomass through photosynthesis in plants, algae, and photosynthetic bacteria[2]. A recent review compared the efficiency of man-made photovoltaics and the photosynthetic reaction center of higher plants[3], and found that while the overall photon-to-stored-energy conversion is less efficient than in photovoltaics, the initial charge-separation process in photosynthesis has a near-unity quantum efficiency, significantly outperforming artificial devices. Understanding the design principles for efficient gen-

eration of charge-separation is a major motivating factor for photosynthetic research.

The protein-pigment complex photosystem II (PSII RC) is unique among photosynthetic reaction centers for forming and stabilizing a redox potential large enough to split water[4]. This potential is used by photosynthetic organisms to catalyze the production of biological energy carriers, evolving oxygen as a byproduct of this process. The wide availability of $O_2$ in the atmosphere enabled the evolution of aerobic respiration, a much more efficient way of utilizing carbohydrates for energy production, and was a critical for the proliferation of multicellular life[5,6]. While much of the basic science underpinning light harvesting and energy transfer leading up to primary charge separation is well understood, many questions remain before the efficiency of the RC may be mimicked. In particular, it is thought that short-lived charge-transfer intermediates play an important role in primary charge separation[7]. While high-spectral and temporal-resolution techniques such as transient-absorption and 2D electronic spectroscopy are available to study the fast movement of energy, these techniques are known to be insensitive to these critical CT states. The focus of this thesis is the theoretical modeling and experimental development of an optical technique called 2D electronic Stark spectroscopy (2DESS) that has enhanced sensitivity to the dynamics of charge-transfer states important in photosynthesis and the function of organic photovoltaics.

## 1.2 Role of Photosystem II in Photosynthesis

In plants, the photosystem II reaction center is found in an organelle called the chloroplast, responsible for harvesting solar energy and storing it as chemical potential (Figure 1.1). The group of proteins that comprise the photosynthetic machinery is housed in the thylakoid membrane, a folded lipid bilayer structure that stores chemical potential in the form of a proton gradient. The inner space enclosed by the thylakoid is called the lumen, while the outer space is the stroma.

The process of photosynthesis in plants proceeds by a "Z-scheme," illustrated pictorially in Figure 1.2. Solar excitation is gathered by antennae complexes located near photosystem II which
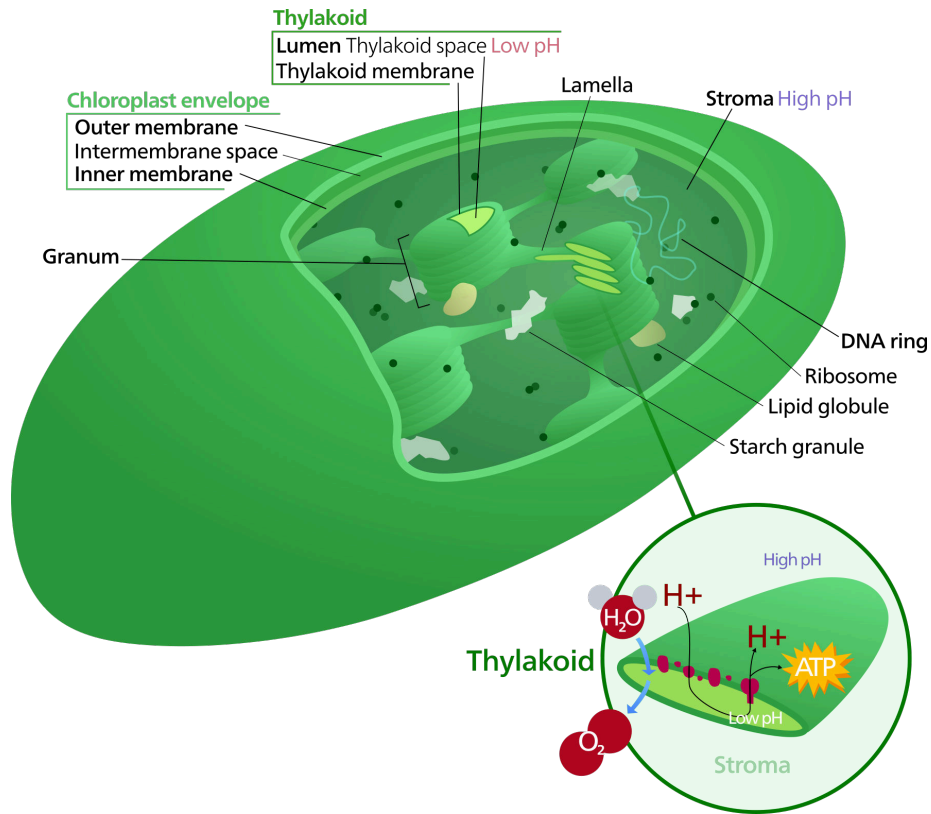
**Figure 1.1** The organization of the chloroplast. Figure adapted from[8].

funnel the excitation to a group of pigments in the center of the photosystem, called the reaction center (RC)[5]. After a series of ultrafast energy- and charge-transfer reactions, a charge separation is stabilized across the protein, with a quinone molecule acting as the final electron acceptor. The positive "hole" localizes in the so-called manganese-cluster in the oxygen evolution center (OEC)[9] domain of PSII. After four photon absorption events, the OEC catalyzes the reduction of $CO_2$ and evolution of oxygen $O_2$, acidifying the lumen in the process[5]. The reduced quinone molecules combine with protons near the stroma to form plastiquinol $PQH_2$ and are released into the membrane, forming a pool of lipid-soluble electron carriers for use by cytochrome $b_6f$. Electrons temporarily stored in plastiquinol as a result of PSII excitation are transferred to the photosystem I reaction center *via* cytochrome $b_6f$ and a water-soluble electron carrier protein

3
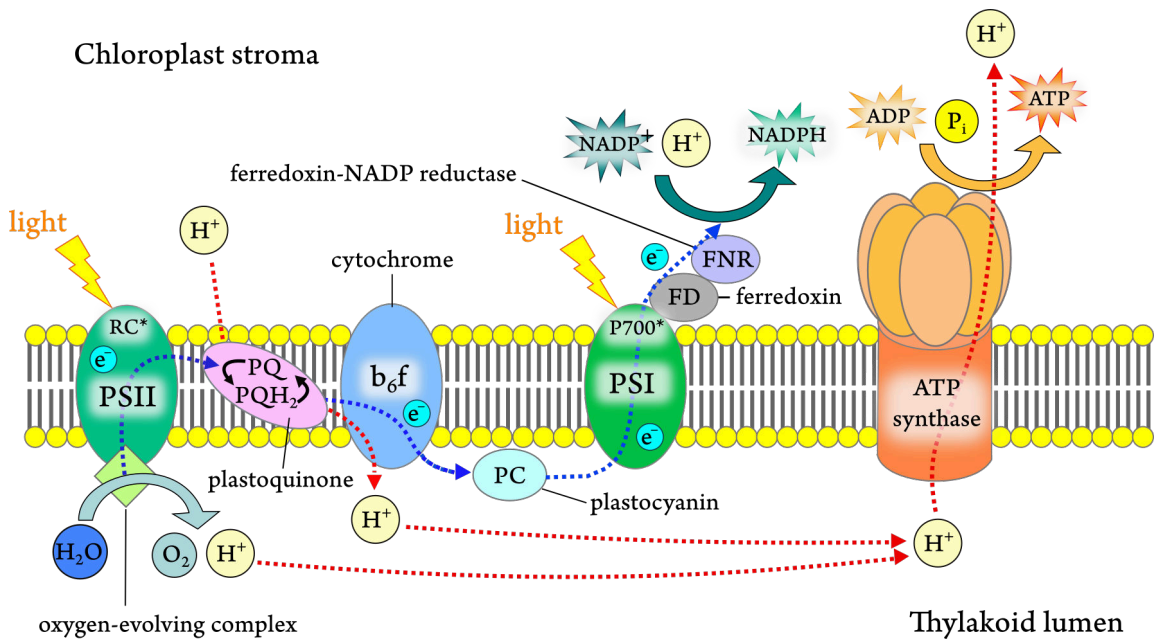
**Figure 1.2** Illustration of the Z-scheme of photosynthesis. The key proteins involved are photosystem II (PSII), photosystem I (PSI), cytochrome b$_6$f, and ATP synthase. Original figure from[10].

plastocyanin. This concurrent action of photosystems II and I is called *non-cyclic electron flow* and is accompanied by the production of NADPH from NADP$^+$ and proton-pumping into the lumen by the cytochrome. The proton gradient is utilized by ATP synthase for the efficient production of ATP by a mechanism called the Calvin cycle. In the *cyclic electron flow* process involving the photosystem I and cytochrome b$_6$f, only the ATP synthesis and proton pumping occur.

Apart from generating the largest naturally-occurring oxidative potential, photosystem II has evolved many supporting functions such as mechanisms for self-repair and regulation of activity[2]. For this work, we are particularly interested in the initial charge-separation reactions occurring in the PS II reaction center, prior to the electron transfer to quinones. To this end, it is important to discuss the structure of the RC that makes efficient charge-separation possible.

*Structure and Function of the Photosystem II Reaction Center*

Photosystem II is a 700 kDa protein complex[11], consisting of about 28 protein subdomains* that have been attributed to light-gathering, photoprotection, and oxygen-evolution functions. The majority of the light absorption by PSII is by chlorophyll a and b bound in antenna domains. Only a small number of these pigments are active in primary charge separation[12]. This was demonstrated by Nanba and Satoh, who were able to obtain a sub-complex consisting of the $D_1$ and $D_2$ proteins, the α and β subunits of Cyt $b_{559}$ and the *psbI* gene product, isolated from the spinach thylakoid[13]. This reaction center preparation came to be known as the $D_1D_2$ Cyt $b_{559}$ preparation and became a popular model system for the study of the primary charge separation processes in the photosystem II RC. A modification of the isolation procedure of $D_1D_2$ Cyt $b_{559}$ based on the work of Berthold et al. and Leeuwen et al. is discussed in Appendix A.

The photoactive pigments in the reaction center consist of six chlorophyll a (Chl), two pheophytin a (Pheo), and two β-carotene (Car) molecules held fixed in a precise orientation by the protein manifold, shown in Figure 1.3. The pigments are nearly-symmetrically positioned between the $D_1$ and $D_2$ subunits and are labeled by the domain to which they are bound. While the position and orientation of the photoactive pigments is now known to 1.9 Å resolution from X-ray studies[11], there is still debate as to the identity and kinetics of intermediate excited states involved in charge separation. One reason for this is the severe "spectral congestion" of the $Q_y$ region around 675 nm. Tracing the kinetics of charge-separation with time-resolved spectroscopies is hindered by the chemical similarity of the photoactive pigments: all eight chlorins contribute to a single broad $Q_y$ band in the linear absorption spectrum at room temperature shown in Figure 1.4. There are several significant contributions to the spectral broadening. The protein environment around each pigment causes electrochromic shifts[16]. Further, pigment-pigment interactions modulate the excitation energy of each pigment as compared to the monomer and delocalize excitations

---

*the number of domains varies among species
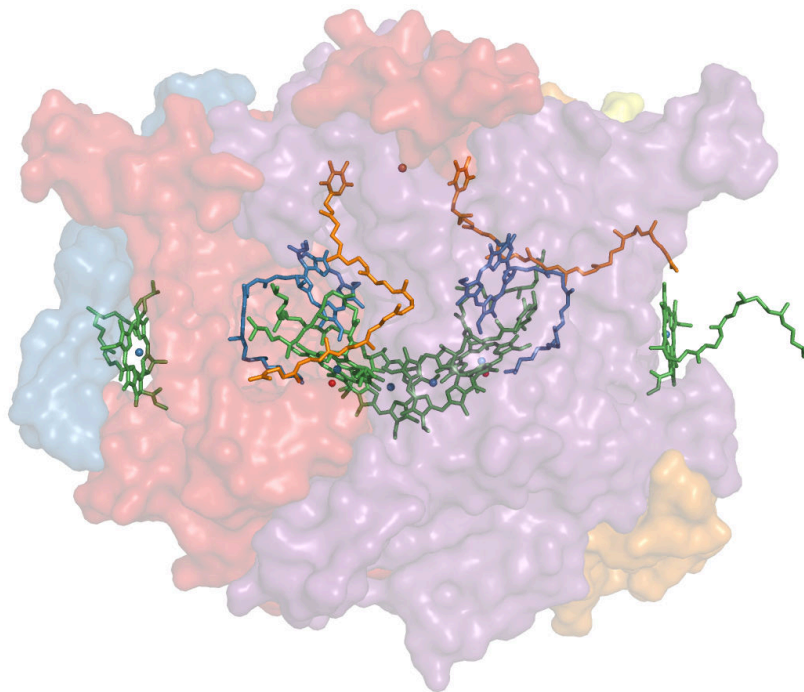
**Figure 1.3** Photosystem II reaction center $D_1 D_2$ Cyt $b_{559}$ preparation approximated from the full crystal structure. At this time, the structure of the isolated preparation is unavailable. The reaction center pigments are highlighted, with chlorophyll a shown in green, pheophytin in blue, and β-carotene in orange. Figure made using the 1.9 Å structure (PDB:3WU2) of *T. vulcanus*[11].

across several pigments[17]. These delocalized excitations are called *excitons* and are responsible for many of the unique features observed in reaction centers. The degree of delocalization and coupling is highly sensitive to the local protein environment. It has been suggested that this inhomogeneity is a design principle that allows efficient charge-separation in a variety of light and temperature conditions[18].

## 1.3 Spectroscopy of Photosystem II

In order to effectively utilize the solar excitation collected by monomeric Chl in antennae complexes, the charge separation processes must complete on a timescale 10 to 100 times faster[21]
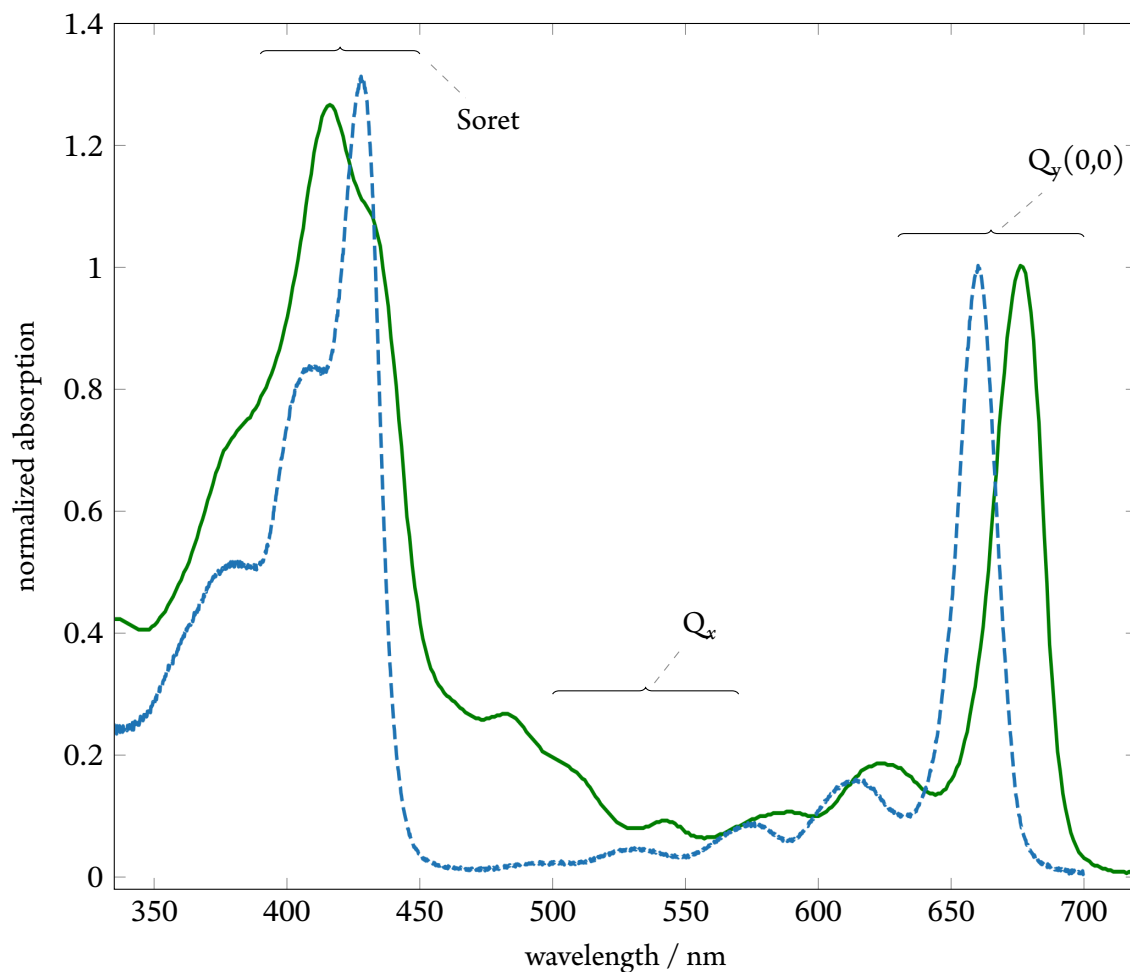
**Figure 1.4** Linear absorption spectrum of $D_1D_2$ Cyt $b_{559}$ preparation at room temperature (green solid line), compared with absorption of chlorophyll a in ether (blue dashed line). PSII RC was prepared as discussed in Appendix A. Chlorophyll a spectral data was extracted from PhotochemCAD[19]. The assignment of the Qx position is an active area of research; a review of the issues can be found in Reimers et al.[20].

than the roughly 5 ns fluorescence lifetime of chlorophyll. The development of ultrafast spectroscopic techniques brought new insight in the study of photosynthetic systems, with pump-probe and time-resolved fluorescence spectroscopy being the most popular approaches. Two-dimensional electronic spectroscopy[22], a technique uniquely sensitive to intermolecular couplings and energy transfer between electronic states, has also been successfully applied to observe energy transfer pathways in the photosystem II RC[23,24].

The historical perspectives[2,25] and current knowledge of the role and function of the PSII reaction center can be found in recent reviews[6,7,26]. Based primarily on theoretical modeling and the combination of linear, pump-probe and other spectroscopies, it is known that the charge separation reaction proceeds only on the $D_1$ branch of the PSII RC[25,27]. Upon photo-excitation, the charge separation reaction is initiated from the $Chl_{D1}$[17] or the $P_{D1}P_{D2}$ "special pair"[28] and after roughly 50 ps produces a charge-separated state $P_{D1}^+Pheo_{D1}^-$. The details of the mechanism during this time are still debated. This is primarily due to the fact that intermediate reactions involve charge-transfer (CT) states that have intrinsically low transition-dipole strengths, making them optically dark[7]. The positions and kinetics of these dark states must be inferred from kinetics of exciton states, all of which have spectrally congested signatures in the $Q_y$ region. Many previous approaches rely on a simultaneous fit to a large number of model parameters such as pigment site-energies, pigment-pigment couplings, and CT state energies[17,28,29]. The resulting spectra are also strongly dependent on the relaxation and system-bath coupling model used; finding an realistic and physically-justified theory to describe relaxation within photosynthetic systems remains an open research question. For these reasons the simulations have limited power to select particular kinetic pathways, which is reflected in the lack of consensus for the rates of formation of proposed CT states. Some workers explain this variation by attributing it to intrinsic distribution of rates due to static disorder of RCs, while others propose that multiple reaction pathways are active simultaneously[29]. There have also been concerns raised about the varying quality of preparation

used in PSII RC studies[30].

In order to differentiate the proposed models, researchers have turned to a variety of techniques to selectively trace the CT states involved in the charge-separation process. Transient-absorption and 2DES experiments on the proposed CT anion-bands have been attempted to observe the evolution of CT states[31,32]. This approach is challenging however, because the anion-bands are located in difficult spectral regions around 450 nm, 550 nm and 720 nm and further tend to be broad and very weak[33], overlapping with spectral signatures of excited states. For this reason, the signal-to-noise ratio of these experiments tend to be poor. Additional complementary measurements are highly desirable.

Stark spectroscopy* is a technique in which the absorption spectrum is measured when a large static electric field is applied to an immobilized, non-conducting sample, and then compared to the field-off absorption. While originally used to understand electrochromic shifts upon solvation of dyes[34] in the pioneering work of Liptay[35], the technique became an important way to uncover charge-transfer states in photosynthetic reaction centers and a variety of polymeric[36] and photovoltaic[37,38] systems. Typically, the original Liptay model of shifted eigenstates is used to analyze Stark data. However, theory work by Somsen et al.[39] and Novoderezhkin et al.[28] extended the modeling of Stark spectroscopy to the modified Redfield formalism. In both cases, the motivation for this was to explain deviations from "classical" first- and second-derivative line-shape behavior in excitonically-coupled systems. Such deviations are termed "non-classical" Stark effects, and have been observed in certain cases[40–42].

Based on a simultaneous fit of absorption, linear and circular dichroism, pump-probe, and Stark spectroscopy to the model developed in[28], Novoderezhkin et al. observed that both the $Chl_{D1}$ and $P_{D1}P_{D2}$ pathways give reasonable quantitative fits to the data. Based on this result, they proposed a two-pathway model depicted in Figure 1.5 where both pathways are active and are

---

*also commonly known as electro-absorption spectrocopy
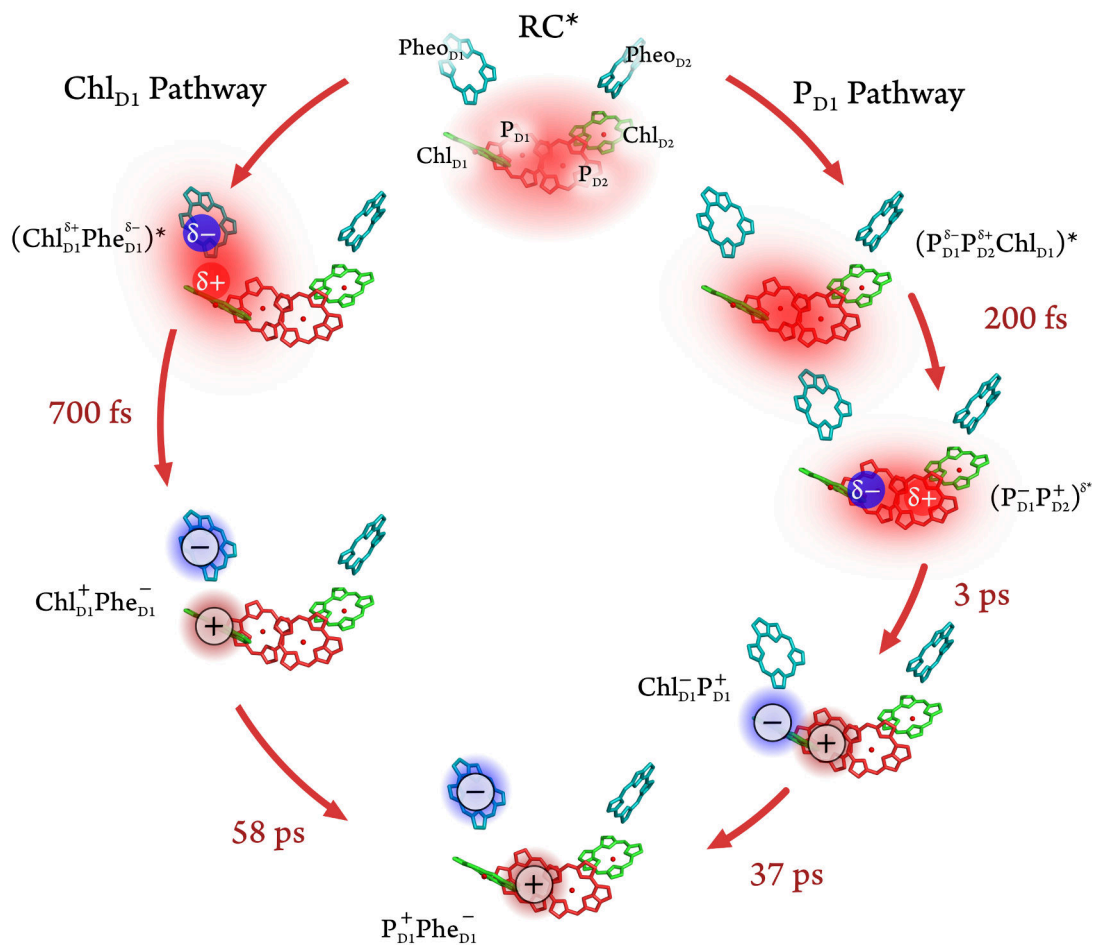
**Figure 1.5** Two-pathway model of charge-separation in the photosystem II reaction center. Timescales shown are from the original experimental paper[29], while the notation is updated to the current interpretation of Romero et al. In the figure, δ+ and δ- indicates charge-transfer character, while δ* is exciton character[26].

preferentially selected on the basis of static disorder. The authors recently performed a combined Stark spectroscopy/mutagenesis study on the PSII reaction center[43] and concluded that their previous two-pathway model is correct[29]. In this work they identified additional CT states.

While the model of Romero et al. does match typical timescales observed in other work, its construction relies on a significant number of fitting parameters such as site-energies and cou-

plings. Further, the dynamics of the crucial short-lived CT states are obtained from fits to transient-absorption and time-resolved fluorescence, which are relatively insensitive to CT states[44]. The remaining information is obtained from steady-state measurements which cannot directly inform the parameterization of the dynamics.

A more-direct measurement is desired to test the validity of the models of charge-separation in the photosystem II reaction center. In this thesis, I propose a method called two-dimensional electronic Stark spectroscopy (2DESS), that combines the high temporal and spectral resolution of 2D electronic spectroscopy with the CT-state sensitivity of Stark spectroscopy. As a superset of two-dimensional electronic spectroscopy, 2DESS promises to reveal the coupling between excitonic and CT states along the detection and excitation frequency axes, while the field-induced changes to kinetics of these states can be observed along the population axis. We expect that this technique can also be applied to other systems in which the role of transient CT states is hard to trace, such as in the function of organic photovoltaics and singlet-fission processes[45].

### 1.4    Outline of Thesis

In the following chapters I describe the development of the two-dimensional electronic Stark spectroscopy technique. The following chapter contains a review of optical spectroscopy with an emphasis on first- and third-order spectroscopies. In Chapter 3 I describe simulations of 2DESS and Stark spectra of a dimer/charge-transfer system inspired by the $P_{D1}P_{D2}$ "special-pair" of PSII in the modified Redfield model. After a discussion of the experimental implementation of 2DESS in Chapter 4, I demonstrate the 2DESS technique on TIPS – pentacene (Chapter 5). In Chapter 6, I show preliminary data on the photosystem II reaction center preparation $D_1D_2$ Cyt $b_{559}$. A summary of the results of this thesis as well as suggestions of future work are contained in the final chapter.

*References*

1.  IEA: World Energy Outlook 2016. Tech. rep. Paris: International Energy Agency, 2016. doi: 10.1787/weo-2016-en.

2.  T. J. Wydrzynski and K. Satoh, eds.: Photosystem II: the light-driven water:plastoquinone oxidoreductase. Dordrecht, The Netherlands: Springer, 2005.

3.  R. E. Blankenship et al.: Comparing photosynthetic and photovoltaic efficiencies and recognizing the potential for improvement. Science (New York, N.Y.) **332**(6031) (2011), 805–9. doi: 10.1126/science.1200165.

4.  R. E. Blankenship: Molecular Mechanisms of Photosynthesis. Cornwall, UK: Blackwell Science, 2002.

5.  J. Barber: Photosystem II: the engine of life. Quarterly reviews of biophysics **36**(1) (2003), 71–89. doi: 10.1017/S0033583502003839.

6.  T. Cardona et al.: Charge separation in Photosystem II: A comparative and evolutionary overview. Biochimica et Biophysica Acta - Bioenergetics **1817**(1) (2012), 26–43. doi: 10.1016/j.bbabio.2011.07.012.

7.  J. R. Reimers et al.: Challenges facing an understanding of the nature of low-energy excited states in photosynthesis. Biochimica et Biophysica Acta - Bioenergetics **1857**(9) (2016), 1627–1640. doi: 10.1016/j.bbabio.2016.06.010.

8.  Wikipedia: Chloroplast. Sept. 4, 2017. url: https://commons.wikimedia.org/wiki/File:Chloroplast%7B%5C_%7D(borderless%7B%5C_%7Dversion)-en.svg.

9.  K. N. Ferreira: Architecture of the Photosynthetic Oxygen-Evolving Center. Science **303**(5665) (Mar. 2004), 1831–1838. doi: 10.1126/science.1093087.

10. Wikipedia: Thylakoid Membrane. Sept. 4, 2017. url: https://commons.wikimedia.org/wiki/File:Thylakoid%7B%5C_%7Dmembrane%7B%5C_%7D3.svg.

11. Y. Umena et al.: Crystal structure of oxygen-evolving photosystem II at a resolution of 1.9 Å.. Nature **473**(7345) (2011), 55–60. doi: 10.1038/nature09913.

12. R. V. Danielius et al.: The primary reaction of photosystem II in the D1-D2-cytochrome b-559 complex. FEBS Letters **213**(2) (1987), 241–244. doi: 10.1016/0014-5793(87)

81498-9.

13. O. Nanba and K. Satoh: Isolation of a photosystem II reaction center consisting of D-1 and D-2 polypeptides and cytochrome b-559. Proceedings of the National Academy of Sciences of the United States of America **84**( January) (1987), 109–112. doi: 10.1073/pnas.84.1.109.

14. D. A. Berthold et al.: A Highly Resolved, Oxygen Evolving Photosystem II Preparation from Spinach Thylakoid Membranes. Federation of European Biochemical Societies Letters **134**(2) (1981), 231–234.

15. P. J. van Leeuwen et al.: Rapid and simple isolation of pure photosystem II core and reaction center particles from spinach. Photosynthesis Research **28**(3) (1991), 149–153. doi: 10.1007/BF00054128.

16. A. W. Rutherford et al.: Back-reactions, short-circuits, leaks and other energy wasteful reactions in biological electron transfer: Redox tuning to survive life in O2. FEBS Letters **586**(5) (2012), 603–616. doi: 10.1016/j.febslet.2011.12.039.

17. G. Raszewski et al.: Theory of Optical Spectra of Photosystem II Reaction Centers: Location of the Triplet State and the Identity of the Primary Electron Donor. Biophysical Journal **88**(2) (2005), 986–998. doi: 10.1529/biophysj.104.050294.

18. E. Romero et al.: Two different charge separation pathways in photosystem II. Biochemistry **49**(20) (2010), 4300–4307. doi: 10.1021/bi1003926.

19. J. M. Dixon et al.: PhotochemCAD 2: a refined program with accompanying spectral databases for photochemical calculations. Photochem. Photobiol. **81** (2005), 212–213. doi: 10.1111/j.1751-1097.2005.tb01544.x.

20. J. R. Reimers et al.: Assignment of the Q-bands of the chlorophylls: coherence loss via $Q_x$ - $Q_y$ mixing. Scientific reports **3** (2013), 2761. doi: 10.1038/srep02761.

21. V. Sundström: Femtobiology. Annual Review of Physical Chemistry **59**(1) (2008), 53–77. doi: 10.1146/annurev.physchem.59.032607.093615.

22. D. M. Jonas: Two-dimensional Femtosecond Spectroscopy. Annual Review of Physical Chemistry **54**(1) (2003), 425–463. doi: 10.1146/annurev.physchem.54.011002.103907.

23. K. L. M. Lewis and J. P. Ogilvie: Probing Photosynthetic Energy and Charge Transfer with Two-Dimensional Electronic Spectroscopy. J. Phys. Chem. Lett. **3**(4) (2012), 503–510. doi: 10.1021/jz201592v.

24. F. D. Fuller et al.: Pulse shaping based two-dimensional electronic spectroscopy in a background free geometry. Opt. Express **22**(1) (2014), 1018–1027. doi: 10.1364/OE.22.001018.

25. B. A. Diner and F. Rappaport: Structure, Dynamics, and Energetics of the Primary Photochemistry of Photosystem II of Oxygenic Photosynthesis. Annual Review of Plant Biology **53**(1) (June 2002), 551–580. doi: 10.1146/annurev.arplant.53.100301.135238.

26. E. Romero et al.: Quantum design of photosynthesis for bio-inspired solar-energy conversion. Nature **543**(7645) (2017), 355–365. doi: 10.1038/nature22012.

27. A. R. Holzwarth et al.: Kinetics and mechanism of electron transfer in intact photosystem II and in the isolated reaction center: Pheophytin is the primary electron acceptor. Proceedings of the National Academy of Sciences **103**(1) (2006), 6895–6900. doi: 10.1073/pnas.0505371103.

28. V. I. Novoderezhkin et al.: Mixing of exciton and charge-transfer states in Photosystem II reaction centers: modeling of Stark spectra with modified Redfield theory. Biophysical journal **93**(4) (2007), 1293–1311. doi: 10.1529/biophysj.106.096867.

29. V. I. Novoderezhkin et al.: Multiple charge-separation pathways in photosystem II: Modeling of transient absorption kinetics. ChemPhysChem **12**(3) (2011), 681–688. doi: 10.1002/cphc.201000830.

30. R. Jankowiak: Probing Electron-Transfer Times in Photosynthetic Reaction Centers by Hole-Burning Spectroscopy. The Journal of Physical Chemistry Letters **3**(12) (June 2012), 1684–1694. doi: 10.1021/jz300505r.

31. B. Donovan et al.: Transient Absorption Studies of the Primary Charge Separation in Photosystem II. The Journal of Physical Chemistry **100**(5) (1996), 1945–1949. doi: 10.1021/jp951984v.

32. S. R. Greenfield et al.: Time-resolved absorption changes of the pheophytin Q(X) band in isolated photosystem II reaction centers at 7 K: Energy transfer and charge separation. Journal of Physical Chemistry B **103** (1999), 8364–8374. doi: 10.1021/jp990962w.

33. S. R. Greenfield and M. R. Wasielewski: Excitation energy transfer and charge separation in the isolated Photosystem {II} reaction center. Photosynthesis Research **48**(1) (1996), 83–97. doi: 10.1007/BF00040999.

34. W. Liptay: Electrochromism and Solvatochromism. Angewandte Chemie - International Edition **8**(3) (1969), 177–188.

35. W. Liptay: Dipole Moments and Polarizabilities of Molecules in Excited Electronic States. Excited States. New York: Academic Press, 1974, 129–229.

36. L. Sebastian et al.: Charge transfer transitions in solid tetracene and pentacene studied by electroabsorption. Chemical Physics **61**(1-2) (Oct. 1981), 125–135. doi: 10.1016/0301-0104(81)85055-0.

37. J. Kalinowski et al.: Electroabsorption study of excited states in hydrogen-bonding solids: epindolidione and linear trans-quinacridone. Chemical Physics **182** (1994), 341–352. doi: 10.1016/0301-0104(94)00030-1.

38. W. Graupner et al.: Direct Observation of Ultrafast Field-Induced Charge Generation in Ladder-Type Poly(Para-Phenylene). Physical Review Letters **81** (1998), 3259–3262. doi: 10.1103/PhysRevLett.81.3259.

39. O. J. G. Somsen et al.: Excitonic Interactions and Stark Spectroscopy of Light Harvesting Systems. The Journal of Physical Chemistry B **102**(44) (1998), 8893–8908. doi: 10.1021/jp981114o.

40. L. J. Moore et al.: Excited-state electronic asymmetry of the special pair in photosynthetic reaction center mutants: Absorption and Stark spectroscopy. Biochemistry **38**(37) (1999), 11949–11960. doi: 10.1021/bi990892j.

41. R. N. Frese et al.: Electric field effects on the chlorophylls, pheophytins, and beta-carotenes in the reaction center of photosystem II.. Biochemistry **42**(30) (2003), 9205–9213. doi: 10.1021/bi0273516.

42. S. G. Boxer: Stark Realities. Journal of Physical Chemistry B **113** (2009), 2972–2983.

43. E. Romero et al.: Mixed exciton-charge-transfer states in photosystem II: Stark spectroscopy on site-directed mutants. Biophysical Journal **103**(2) (2012), 185–194. doi: 10.1016/j.bpj.2012.06.026.

44. A. Gelzinis et al.: Tight-binding model of the photosystem II reaction center: Application to two-dimensional electronic spectroscopy. New Journal of Physics **15** (2013). doi: 10.1088/1367-2630/15/7/075013.

45. N. Monahan and X.-Y. Zhu: Charge Transfer–Mediated Singlet Fission. Annual Review of Physical Chemistry **66**(1) (2015), 601–618. doi: 10.1146/annurev-physchem-040214-121235.

**CHAPTER 2**

**Theory of Nonlinear Optical Spectroscopic Methods**

## *2.1 Introduction*

Over the last two decades, two-dimensional electronic spectroscopy (2DES) has emerged as a powerful tool for studying complex, excitonically-coupled systems. In concept, the 2DES technique extends pump-probe spectroscopy by spectrally-resolving the excitation axis $\omega_\tau$ in addition to the detection axis $\omega_t$ by replacing the single pump pulse with two pulses with a variable time delay $\tau$ between them. Upon Fourier-transformation along $\tau$, a two-dimensional spectrum is obtained that is rich in chemical information of three types: the energies and degree of coupling between electronic excited states, the nature of dephasing in the system and the degree of inhomogeneous broadening, and finally the kinetics of energy transfer between these excited states. The primary advantage of 2DES over transient-absorption is that all of this information may be obtained without sacrificing frequency resolution nor time-resolution. The utility of 2DES has been demonstrated for the study of photosynthetic antenna complexes, photosynthetic enzymes, and artificial systems. In many of these systems, photo-catalyzed reactions proceed through a sequence of charge-separated states that are particularly challenging to study because they form rapidly and have weak spectral signatures. In particular, it was demonstrated that 2DES spectroscopy is not very sensitive to them.

In this chapter, I develop the theory of two-dimensional electronic Stark spectroscopy (2DESS), which enhances the sensitivity of 2DES to CT states by the perturbation of a large static (Stark)

field. I will discuss the semi-classical theory of optical spectroscopy required to describe the third-order signals obtained in 2DESS. In this paradigm, the process of optical signal generation can be broken into two conceptual steps. First, a classical field propagating in the sample generates an oscillating polarization $P(t)$ in the sample. If the field intensity is sufficiently high as when using short laser pulses, the response of the material becomes nonlinear in the field and this polarization gives rise to such interesting effects as second-harmonic generation, transient-absorption, and two-photon absorption. Assuming the magnetic properties can be neglected, this macroscopic polarization can be interpreted as the expectation value of the quantum polarization operator $\mathrm{Tr}\,P\hat{\rho}(t)$. The generated nonlinear polarization acts as a source term in Maxwell's wave equation and produces a signal field $E_s$ that is detected in the experiment. In this way, the task of the spectroscopist is to reconstruct the time-dependent density matrix $\hat{\rho}(t)$ given the measured signal field $E_s$.

In the following sections I describe the fundamentals of linear and third-order spectroscopies, starting with a description of the generation of the signal field $E_s$ as a function of the material response function $R$. I will briefly describe phase-reconstruction techniques, heterodyne detection and phase-cycling. In the following section I will discuss how the material response $R$ arises from the quantum dipole operator $\widehat{Q}$, and how dephasing and models of the bath couple to the material Hamiltonian to produce population relaxation and decoherence. In the final sections, I describe how the Stark field changes the molecular Hamiltonian to produce the 2DESS signal. This addition is one of the original contributions of this thesis and is used in the following chapters for the simulation and interpretation of experimental 2DESS spectra. The initial sections follow the approach of Butcher and Cotter to describe classical nonlinear optics from the quantum-mechanical prospective. A more complete description of theoretical methods used in third-order spectroscopies may be found in Mukamel[2] and Hamm and Zanni[3], as well as reviews cited in this chapter.

## 2.2   Theory of Signal Detection

*Electromagnetic Wave Equation*

The Maxwell equations describe the propagation of classical electric fields in matter. We are interested in deriving the nonlinear response of the material to an intense field. In the general case they take the form

$$\nabla \times \boldsymbol{E} - \frac{\partial \boldsymbol{B}}{\partial t} = 0 \tag{2.1a}$$

$$\nabla \times \boldsymbol{H} - \frac{\partial \boldsymbol{D}}{\partial t} = \boldsymbol{J} \tag{2.1b}$$

$$\nabla \cdot \boldsymbol{D} = \rho \tag{2.1c}$$

$$\nabla \cdot \boldsymbol{B} = 0 \tag{2.1d}$$

In these equations $\boldsymbol{E}$ and $\boldsymbol{H}$ are the electric field vector (in $\mathrm{V\,m^{-1}}$) and the magnetic field vector (in $\mathrm{A\,m^{-1}}$), respectively.

Solving this set of equations requires the form of coupling between the pairs $(\boldsymbol{E}, \boldsymbol{B})$ and $(\boldsymbol{B}, \boldsymbol{H})$ called the constitutive equations. In general they may have a complicated relationship[4], but in uniform isotropic linear media they take the form

$$\boldsymbol{D} = \epsilon \boldsymbol{E} = \epsilon_0 \boldsymbol{E} + \boldsymbol{P} \tag{2.2a}$$

$$\boldsymbol{B} = \mu \boldsymbol{H} = \mu_0 (\boldsymbol{H} + \boldsymbol{M}) \tag{2.2b}$$

It is typical in optics to deal with non-magnetic media so we can assume that the magnetisation $\boldsymbol{M}$ is zero. Further, as I will be dealing with solid, nonconducting samples that contain only bound charges, I can safely assume that the current $\boldsymbol{J}$ and charge $\hat{\rho}$ are also identically zero. With these simplifications and by substituting (2.2), it is possible to eliminate $\boldsymbol{H}$ from the Maxwell equations to obtain a wave equation in the time domain

$$\nabla \times \nabla \times \boldsymbol{E} = -\frac{1}{c^2} \frac{\partial^2 \boldsymbol{E}}{\partial t^2} - \mu_0 \frac{\partial^2 \boldsymbol{P}}{\partial t^2} \tag{2.3}$$

18

In the case of discrete monochromatic continuous beams, it is often more convenient to obtain (2.3) in the frequency domain by substituting the Fourier-relations for $\boldsymbol{E}(t)$

$$\nabla \times \nabla \times \boldsymbol{E}(f) = \frac{4\pi^2 f^2}{c^2} \boldsymbol{E}(f) + 4\pi^2 f^2 \mu_0 \boldsymbol{E}(f)$$

$$= \frac{\omega^2}{c^2} \boldsymbol{E}(\omega) + \omega^2 \mu_0 \boldsymbol{P}(\omega) \tag{2.4}$$

This is the wave-equation for monochromatic inputs. It is occasionally useful to use a quasi-monochromatic form, in which $\widehat{\boldsymbol{E}}(f)$ is an envelope function. This is particularly relevant for nonlinear interactions with femtosecond optical pulses. For now, we are assuming that there is only a single field-matter interaction, so there cannot be any cross-terms containing multiple input frequencies $\propto \omega_i \omega_j$.

In order to solve (2.3), we need a self-consistent field pair $(\boldsymbol{E}, \boldsymbol{P})$ that satisfies the boundary conditions of our experiment.

*Material Response Functions*

The simplest model of optical response due to H.A. Lorentz proposes that a propagating electric field induces a proportional polarization in the sample[5]. With the development of the laser, it became possible to observe optical nonlinearities which could be treated as anharmonicities within the simple model. To describe this behavior, it is convenient to expand the electric polarization $\boldsymbol{P}$ in powers of the incident electric field $\boldsymbol{E}$

$$\boldsymbol{P}(t) = \boldsymbol{P}^{(1)}(t) + \boldsymbol{P}^{(2)}(t) + \cdots + \boldsymbol{P}^{(n)}(t) + \cdots \tag{2.5}$$

where polarization of order $n$ is $\boldsymbol{P}^{(n)}$. The first order polarization $\boldsymbol{P}^{(1)}$ takes the form of a linear integral operator

$$\boldsymbol{P}^{(1)}(t) = \epsilon_0 \int_{-\infty}^{\infty} \mathrm{d}\tau \, \boldsymbol{T}^{(1)}(t;\tau) \cdot \boldsymbol{E}(\tau)$$

19

Further, we require that the system be time-invariant with respect to an arbitrary time shift $t_0$, such that there is no "absolute time" reference

$$\boldsymbol{T}^{(1)}(t; \tau - t_0) \equiv \boldsymbol{T}^{(1)}(t + t_0, \tau)$$

With this assumption, the first order polarization becomes a convolution of the electric field $\boldsymbol{E}(t)$ with an integral kernel called the *first-order material response function* $\boldsymbol{R}^{(1)}(\tau - t)$[1]

$$\boldsymbol{P}^{(1)}(t) = \epsilon_0 \int_{-\infty}^{\infty} d\tau\, \boldsymbol{R}^{(1)}(t - \tau) \cdot \boldsymbol{E}(\tau) = \epsilon_0 \int_{-\infty}^{\infty} d\tau\, \boldsymbol{R}^{(1)}(\tau) \cdot \boldsymbol{E}(t - \tau) \qquad (2.6)$$

To ensure that the material response yields a physically acceptable solution, we require two additional constraints. First, the material response must be real to ensure that the resulting polarization and thus the signal field $\boldsymbol{E}_s$ is real. Second, the material response must vanish for times before the field perturbs it $(\boldsymbol{R}^{(1)}(t < 0) \equiv 0)$ to satisfy causality.

By analogous arguments, each term of the polarization expansion $\boldsymbol{P}^{(n)}(t)$ can be shown to be related to a real response function tensor $\boldsymbol{R}^{(n)}(t_1, t_2, \cdots, t_n)$ of rank $n + 1$ that vanishes for any negative $t_n$. The polarization term is then multi-linear in the input fields. For third-order, the expansion is

$$\boldsymbol{P}^{(3)}(t) = \epsilon_0 \int_{-\infty}^{\infty} d\tau_1 \int_{-\infty}^{\infty} d\tau_2 \int_{-\infty}^{\infty} d\tau_3\, \boldsymbol{R}^{(3)}(\tau_1, \tau_2, \tau_3) \vdots \boldsymbol{E}(t - \tau_1)\boldsymbol{E}(t - \tau_2)\boldsymbol{E}(t - \tau_3) \quad (2.7)$$

These expressions are also commonly transformed to the frequency domain to obtain *susceptibilities* $\boldsymbol{\mathcal{X}}^{(n)}$

$$\boldsymbol{P}^{(1)}(t) = \epsilon_0 \int_{-\infty}^{\infty} d\omega\, \boldsymbol{\mathcal{X}}^{(1)}(-\omega_s; \omega) \cdot \boldsymbol{E}(\omega) \exp(-i\omega_s t) \qquad (2.8)$$

and

$$\boldsymbol{P}^{(3)}(t) = \epsilon_0 \int_{-\infty}^{\infty} d\omega_1 \int_{-\infty}^{\infty} d\omega_2 \int_{-\infty}^{\infty} d\omega_3\, \boldsymbol{\mathcal{X}}^{(3)}(-\omega_s; \omega_1, \omega_2, \omega_3) \vdots \boldsymbol{E}(\omega_1)\boldsymbol{E}(\omega_2)\boldsymbol{E}(\omega_3) \exp(-i\omega_s t)$$

$$(2.9)$$

where the susceptibility tensor $\chi^{(n)}$ is defined as the Fourier transform of the response function

$$\chi^{(n)}(-\omega_s; \omega_1, \cdots, \omega_n) = \int_{-\infty}^{\infty} d\tau_1 \cdots \int_{-\infty}^{\infty} d\tau_n \, \mathbf{R}^{(n)}(\tau_1, \cdots, \tau_n) \exp\left(-i \sum_j^n \omega_j \tau_j\right) \quad (2.10)$$

and $\omega_s$ is the "signal" frequency that represents the result of phase-matching that is discussed in the following section. For linear susceptibility, $\omega_s = \omega$.

This susceptibility approach is particularly useful for the case of monochromatic input fields because in that case the resulting signal field at a particular frequency depends only on the amplitude of a handful of frequency components. This approach is explored in detail in Boyd and Butcher&Cotter. In ultrafast spectroscopy, however, the broad bandwidth of the incident fields and our interest in time-dependant phenomena make the use of the time-domain or carrier-envelope form expressions (to be described later) much more convenient.

Let's turn now to how the material response function generates a signal field. In a later section, the material response will be tied to a microscopic quantum-mechanical description of the system.

## 2.3  Linear Response

To derive the expression for the signal field $\mathbf{E}_s$, it is convenient to first derive the result of a linear field-mater interaction. Higher-order interactions can then be treated as small perturbations to the linear response. To begin, we start with the wave equation in the frequency domain (2.4) and insert the expression for first-order polarization (2.8),

$$
\begin{aligned}
\nabla \times \nabla \times \mathbf{E}(\omega) &= \frac{\omega^2}{c^2} \mathbf{E}(\omega) + \omega^2 \mu_0 \mathbf{P}^{(1)}(\omega) \\
&= \frac{\omega^2}{c^2} (\mathbf{1} + \chi^{(1)}(-\omega; \omega)) \cdot \mathbf{E}(\omega) \\
&\equiv \frac{\omega^2}{c^2} \epsilon(\omega) \cdot \mathbf{E}(\omega) \quad (2.11)
\end{aligned}
$$

This equation describes the response of the material to an incident field, linking the field to the material *dielectric tensor* $\epsilon$. There is an implicit position dependence to this equation, which we

can make explicit by expanding the solution in a basis of plane waves propagating in the direction **s**,

$$E(\mathbf{r}, \omega) = \widehat{E}_{\omega_s} \exp(i\mathbf{k}_s \cdot \mathbf{r}) + \text{c.c.} \tag{2.12}$$

where it is conventional to expand the vector in terms of the real $(n)$ and imaginary $(\kappa)$ parts of the index of refraction, $\mathbf{k}_s = \omega_s[n(\omega_s) + i\kappa(\omega_s)]/c \, \mathbf{s}$. The magnitude of the vector $\mathbf{k}_s$ is not arbitrary because both the Helmholtz equation (2.11) and the Maxwell equations (2.1) must be satisfied simultaneously. This leads to the Fresnel equations which link the components of the index of refraction for a propagation direction **s** and the components of the dielectric tensor $\epsilon$,

$$[(\mathbf{s} \cdot \mathbf{e})\mathbf{s} - \mathbf{e}][n(\omega_s) + i\kappa(\omega_s)]^2 + [\text{Re}\,\epsilon + i\,\text{Im}\,\epsilon] \cdot \mathbf{e} = 0 \tag{2.13}$$

where $\mathbf{e}$ is the polarization vector of the electric field that satisfies $\mathbf{e}^\star \mathbf{e} = 1^*$. It is this set of equations that results in a birefringence in certain crystals and provides a way to obtain phase-matching in second harmonic generation. For our purposes, it is sufficient to deal with isotropic samples in which the index of refraction is independent of propagation direction. This simplification allows us to replace the dielectric tensor with a scalar $\epsilon$ and yields the familiar expression,

$$[n(\omega_s) + i\kappa(\omega_s)]^2 = \epsilon = 1 + \chi^{(1)} \tag{2.14}$$

This equation yields a particularly simple solution if we assume that the sample is "optically thin," that such that $n \gg \kappa$. In this case, we may replace the expression (2.14) by $n(n + i2\kappa)$, and notice that $\kappa = \text{Im}\,\chi^{(1)}/2n$. The measured signal field after propagation through the sample oriented perpendicular to $\hat{z}$ is

$$E_s(z, \omega_s) = \widehat{E}_{\omega_s} \exp(-\kappa\omega_s z/c) \exp(in\omega_s z/c) \tag{2.15}$$

---

*this topic is further discussed in a later section, in which it is demonstrated that polarization selection may be used for attenuating certain transitions

The absorption exponentially attenuates the signal as a function of propagation distance along $\hat{z}$. This is reflected in Beer's Law

$$\frac{\partial}{\partial z}I_s(\omega_s) = \frac{\partial}{\partial z}E_s^\star E_s = -\frac{2\kappa(\omega_s)\omega_s}{c}I_s = -\frac{\text{Im}\mathcal{X}^{(1)}(-\omega_s;\omega_s)\omega_s}{n(\omega_s)c}I_s \qquad (2.16)$$

where the absorption coefficient $\alpha \propto \text{Im}\,\mathcal{X}^{(1)}/\sqrt{1 + \text{Re}\mathcal{X}^{(1)}}$.

## 2.4   Nonlinear Interactions

Having obtained the expression for the first-order response, we now turn our attention to the higher-order terms in $(2.5)$. Collecting them into a single term $P^{(\text{NL})}$ yields

$$P(r,t) = \epsilon_0 \int_{-\infty}^{\infty} d\omega\, \mathcal{X}^{(1)}(-\omega,\omega) \cdot E(r,t)\exp(-i\omega t) + P^{(\text{NL})}(r,t) \qquad (2.17)$$

As we saw in the previous section, the first term on the right contributes to index of refraction and the absorption of the incident field. The nonlinear terms act as a perturbation to this behavior. Substituting this expression into the wave equation $(2.3)$, we obtain

$$\nabla\times\nabla\times E(r,t)+\frac{1}{c^2}\frac{\partial^2}{\partial t^2}\int_{-\infty}^{\infty} d\omega\,(1+\mathcal{X}^{(1)}(-\omega;\omega))\cdot E(r,\omega)\exp(-i\omega t) = -\mu_0\frac{\partial^2 P^{(\text{NL})}(r,t)}{\partial t^2}$$
$$(2.18)$$

Whereas in the linear absorption case we expanded in a basis of infinite plane waves with a sinusoidal phase dependence, this time we will use the quasimonochromatic (carrier-amplitude) form for the fields

$$E(r,t) = \sum_{\omega_s\geq 0} \widehat{E}_{\omega_s}(r,t)\exp(-i\omega_s t) + \text{c.c.} \qquad (2.19)$$

$$P(r,t) = \sum_{\omega_s\geq 0} \widehat{P}_{\omega_s}(r,t)\exp(-i\omega_s t) + \text{c.c.} \qquad (2.20)$$

where $\widehat{E}_{\omega_s}(t)$ and $\widehat{P}_{\omega_s}(t)$ are the bandwidth-limited slowly-varying envelopes centered near $\omega_s$. The spatial phase in this form is hidden in the envelopes. In the frequency domain $(2.19)$ becomes

$$E(r,\omega) = \frac{1}{2}\sum_{\omega_s\geq 0} \widehat{E}_{\omega_s}(r,\omega - \omega_s) + \text{c.c.} \qquad (2.21)$$

23

Now we can substitute (2.21) and (2.20) into (2.18) to obtain an expression involving the field envelopes. We will focus on the term involving $\chi^{(1)}$ in (2.18) first and rederive an expression analogous to (2.15). Using (2.14) for an isotropic sample, this term becomes

$$
\begin{aligned}
I &= \frac{1}{c^2}\frac{\partial^2}{\partial t^2}\int_{-\infty}^{\infty} d\omega\,(1 + \chi^{(1)}(-\omega;\omega))E(\boldsymbol{r},\omega)\exp(-i\omega t)\\
&= -\int_{-\infty}^{\infty} d\omega\,\frac{[n(\omega) + i\kappa(\omega)]^2\omega^2}{c^2}\frac{1}{2}\sum_{\omega_s\geq 0}[\widehat{\boldsymbol{E}}_{\omega_s}(\boldsymbol{r},\omega - \omega_s) + \widehat{\boldsymbol{E}}^{\star}_{\omega_s}(\boldsymbol{r},-\omega - \omega_s)]\exp(-i\omega t)\\
&= -\frac{1}{2}\sum_{\omega_s\geq 0}\int_{-\infty}^{\infty} d\omega\,k^2(\omega)\widehat{\boldsymbol{E}}_{\omega_s}(\boldsymbol{r},\omega - \omega_s)\exp(-i\omega t) + \text{c.c.}
\end{aligned}
$$

To simplify the expression further, we expand $k^2(\omega)$ in a Taylor series around $\omega_s$, which leads to the expression

$$
I \approx -\frac{1}{2}\sum_{\omega_s\geq 0}\exp(-i\omega_s t)\left(k_s^2 + i2k_s\left.\frac{dk}{d\omega}\right|_{\omega_s}\frac{\partial}{\partial t} - k_s\left.\frac{d^2k}{d\omega^2}\right|_{\omega_s}\frac{\partial^2}{\partial t^2}\right)\widehat{\boldsymbol{E}}_{\omega_s}(\boldsymbol{r},t) + \text{c.c.}
$$

Substituting this result into (2.18), expanding both $\boldsymbol{E}$ and $\boldsymbol{P}^{(\mathrm{NL})}$ in the carrier-envelope form and collecting terms centered near $\omega_s$, we can obtain an equation for the time-domain envelope components of the electric field

$$
\nabla\times\nabla\times\widehat{\boldsymbol{E}}_{\omega_s}(\boldsymbol{r},t) - \left(k_s^2 + i2k_s\frac{1}{v_g}\frac{\partial}{\partial t} - k_s\left.\frac{d^2k}{d\omega^2}\right|_{\omega_s}\frac{\partial^2}{\partial t^2}\right)\widehat{\boldsymbol{E}}_{\omega_s}(\boldsymbol{r},t) = \mu_0\omega_s^2\widehat{\boldsymbol{P}}^{(\mathrm{NL})}_{\omega_s}(\boldsymbol{r},t) \quad (2.22)
$$

where $v_g \equiv \left(\left.\dfrac{dk}{d\omega}\right|_{\omega_s}\right)^{-1}$ is the group velocity. This equation describes the propagation of bandwidth-limited signals of arbitrary spatial frequency distribution, encoded in the $\boldsymbol{r}$-dependence of the envelopes.

For simplicity, we make a number of approximations analogous to those used in the linear case. First, we orient the coordinate system such that the generated signal lies along the $\hat{z}$ direction and look for an infinte plane-wave solution. This reduces the form of the field envelope to $\widehat{\boldsymbol{E}}_{\omega_s}(z,t)$ and the first term in (2.22) to $-\dfrac{\partial^2}{\partial z^2}$. Next, we assume that the signal field is propagating in the

$+\hat{z}$ direction, such that $\widehat{\boldsymbol{E}}_{\omega_s}(z,t) = \boldsymbol{A}_{\omega_s}(z,t)\exp(+ik_s z)$. Finally, we make the spatial slowly-varying approximation, $\left|\frac{\partial^2 A_{\omega_s}}{\partial z^2}\right| \ll \left|k_s \frac{\partial A_{\omega_s}}{\partial z}\right|$. With these approximations, we obtain

$$\left(i\frac{\partial}{\partial z} + i\frac{1}{v_g}\frac{\partial}{\partial t} - \frac{1}{2}\left.\frac{\partial^2 k}{\partial \omega^2}\right|_{\omega_s}\frac{\partial^2}{\partial t^2}\right)\boldsymbol{A}_{\omega_s}(z,t) = -\frac{\mu_0\omega_s^2}{2k_s}\boldsymbol{P}^{(\mathrm{NL})}{}_{\omega_s}(\boldsymbol{r},t)\exp(-ik_s z) \quad (2.23)$$

In the limit of monochromatic fields (no time-dependence of envelopes) and no nonlinear polarization, this expression reduces to the linear field propagation expression (2.15).

*Optical Phase Matching*

The expression (2.23) obtained in the previous section demonstrates an important spatial selectivity property called "phase-matching." We can demonstrate this property by taking the limit of monochromatic fields, such that the time derivatives become negligible. In this case, (2.23) reduces to

$$\frac{\partial}{\partial z}\boldsymbol{A}_{\omega_s}(z) = i\frac{\mu_0\omega_s^2}{2k_s}\boldsymbol{P}^{(\mathrm{NL})}{}_{\omega_s}(\boldsymbol{r},t)\exp(-ik_s z) \quad (2.24)$$

From the discussion on response functions above, we saw that the polarization is multi-linear in the input fields, and we assumed that the nonlinear polarization cannot couple to the generated signal. If we posit a plane-wave solution for $\boldsymbol{P}_{\omega_s}^{(n>1)}$ as we did for $\widehat{\boldsymbol{E}}_{\omega_s}$, we observe that each non-linear polarization term at a signal frequency $\omega_s = \pm\omega_1 \pm \omega_2 \pm \cdots \pm \omega_n$ would propagate with a spatial frequency $\boldsymbol{k}_s = \pm\boldsymbol{k}_1 \pm \boldsymbol{k}_2 \pm \cdots \pm \boldsymbol{k}_n$. Labeling the generated signal polarization vector along $\hat{z}$ as $k_s$ and the projection of the polarization spatial frequency on $\hat{z}$ as $k_s' = \boldsymbol{k}_s' \cdot \hat{z}$, the equation becomes

$$\frac{\partial}{\partial z}\boldsymbol{A}_{\omega_s}(z) = i\frac{\mu_0\omega_s^2}{2k_s}\widehat{\boldsymbol{P}}_{\omega_s}(z)\exp(i(k_s' - k_s)z) \quad (2.25)$$

By integrating this over the sample of length $z$ we can obtain an expression for the field envelope after propagation through the sample, in the limit of no signal absorption,

$$\boldsymbol{A}_{\omega_s}(z) = \frac{i\mu_0\omega_s^2 z}{2k_s}\widehat{\boldsymbol{P}}_{\omega_s}\mathrm{sinc}\left(\frac{\Delta k_s z}{2}\right)\exp\left(\frac{i\Delta k_s z}{2}\right) \quad (2.26)$$

25

where the wavevector mismatch is $\Delta k_s \equiv k_s' - k_s$ and we have assumed that the polarization is uniform along $\hat{z}$.

For large sample thicknes $(z \gg 1/\omega)$, the $\mathrm{sinc}(x) = \sin x/x$ function can be approximated as a delta function. In this limit it acts as a sharply selective spatial filter that strongly attenuates the generation of polarization components away from $\hat{z}$. In the opposite limit, it reduces to unity, performing no filtering. In this case, signals are generated in all directions. In practice, the terms that we have neglected by ignoring time-dependence and spatial dispersion serve to relax the phase-matching condition even for macroscopic samples.

This spatial filtering behavior has important experimental consequences, because it allows the selection of a particular order of nonlinearity and field interaction order simply by placing the detector at a particular spatial position.

*Homodyne and Heterodyne Detection*

A fundamental challenge in coherent optical spectroscopy lies in the fact that at this time it is impossible to measure the amplitude of an optical wave directly. Instead, optical detectors are "square-law" in the sense that it is the incident optical power that is measured. An ideal optical detector measures a current $i_s$* that is linear with the incident power

$$i_s = kAI_s \tag{2.27}$$

where $k$ is a proportionality constant, and $A$ is the portion of the detector area illuminated by the beam. For a typical experiment, we are interested in the time-domain or frequency response of this signal. For example, in a linear absorption experiment

$$\frac{\Delta i_s(\omega)}{i_0} = \frac{I_s(\omega) - I_0}{I_0} \approx \alpha(\omega) \propto \left| \chi^{(1)} \right|^2 \tag{2.28}$$

---

*or charge, as in CCD detectors

where $\alpha$ is the unnormalized absorption coefficient we obtained earlier. As can be seen from (2.26), this proportionality to the square of the absolute value of susceptibility is true for any order nonlinearity[6]. It is called *homodyne detection* because the signal field is optically mixed with itself, $E_s{}^\star E_s$, and is detected as a differential change in the intensity $\Delta I_s$.

In contrast, the phase-matching criterion suggests that instead of detecting the signal field directly, we can instead add it coherently to an auxiliary field propagating in the same direction called the *local oscillator* and detect the interference that results. This approach is called *heterodyne detection*. In this case,

$$
\begin{aligned}
i_{\text{detected}}(t) &\propto |\boldsymbol{E}_{\text{LO}}(t) + \boldsymbol{E}_s(t)|^2 \\
&= I_{\text{LO}} + I_s(t) + \text{Re}[\boldsymbol{E}_{\text{LO}}^\star(t) \cdot \boldsymbol{E}_s(t)] \\
&\approx I_{\text{LO}} + \text{Re}[\boldsymbol{E}_{\text{LO}}^\star(t) \cdot \boldsymbol{E}_s(t)]
\end{aligned}
\tag{2.29}
$$

The local oscillator acts to amplify the much-weaker signal $\boldsymbol{E}_s$ and, provided that the local oscillator has a well characterized spectrum and phase, allows us to reconstruct the full field amplitude of the signal rather than just its absolute value. This technique is particularly useful in noncollinear geometries because this increase in signal strength allows detection of very weak optical signals above the detector noise-floor.

*Field Polarization*

In the dipole approximation for isotropic media, the propagation of the incident field does not depend on polarization. In the case of higher-order interactions such as pump-probe, or in experiments beyond the dipole approximation such as circular dichroism, the polarization vector becomes important to properly describe the interaction. In this case, it is common to express the polarization of an electric field as

$$
\boldsymbol{E}_s = \boldsymbol{e}E_s = e_\mu E_{s\mu}
\tag{2.30}
$$

where $\boldsymbol{e}$ is a (complex) unit vector representing the polarization state of the field $\boldsymbol{E}_s$ which satisfies $\boldsymbol{e}^\star \cdot \boldsymbol{e}$. The generated electric polarization $\boldsymbol{P}^{(\mathrm{NL})}$ is sensitive to the polarization of the incident fields $\boldsymbol{E} = \boldsymbol{e}_j E_j$. By judiciously choosing the polarization vectors of the input fields, particular combinations of tensor elements of $\boldsymbol{P}^{(\mathrm{NL})}$ can be probed.

## 2.5 *Density Matrix Perturbation Theory*

As discussed in the previous sections, the superposition of fields in media can lead to a macroscopic polarization that we treated as a perturbation to the linear response. This polarization was characterized in a field-independent manner through a response function $\boldsymbol{R}$, or equivalently, a susceptibility $\mathcal{X}$. In the semi-classical approach, we can tie this response function to the microscopic behavior by obtaining expectation values of quantum operators corresponding to electric and magnetic dipoles, and higher order terms in a multipole expansion. In typical optical applications, the higher order contributions are negligible, so we will stop at the electric dipole term. This is called the *electric dipole approximation*. A classical approach to this problem is described in[4], sec 6.6.

In analogy to the classical definition, we define the macroscopic electric polarization $\boldsymbol{P}$ as the dipole moment density defined in a volume $V$. This volume must be small enough that the variations in external properties like the incident field intensity are small, and yet large enough that this volume contains a representative ensemble of quantum systems. By the correspondence principle, we define the polarization as

$$\boldsymbol{P}(\boldsymbol{r}, t) = \left\langle \widehat{\boldsymbol{Q}}_{\mathrm{total}} \right\rangle / V \tag{2.31}$$

where $\widehat{\boldsymbol{Q}}_{\mathrm{total}}$ is the electric dipole operator that includes a sum over all charges in the volume, of the form

$$\widehat{\boldsymbol{Q}}_{\mathrm{total}} = -e \sum_j \hat{\boldsymbol{r}}_j + e \sum_k Z_k \hat{\boldsymbol{r}}_k \tag{2.32}$$

where $e$ is the electric charge and $Z_k$ is the charge of the nucleus. In the density matrix formalism, this expectation value can be calculated by evaluating the trace so that the polarization we seek is given by,

$$P(\boldsymbol{r}, t) = \frac{1}{V} \operatorname{Tr}\left[\widehat{\boldsymbol{Q}}(\boldsymbol{r})\hat{\rho}(t)\right] \tag{2.33}$$

where the time evolution of the density matrix is governed by the Liouville equation

$$i\hbar \frac{\mathrm{d}\hat{\rho}}{\mathrm{d}t} = [\widehat{H}, \hat{\rho}] \tag{2.34}$$

These last two equations provide the link between the macroscopic generated signal field $\boldsymbol{E}_\mathrm{s}$ and the microscopic time-evolution of the quantum system in the dipole limit. It is accurate provided the generated signal is not strong enough to couple back to the system. To make the problem more tractable, we make a further simplification and assume that the volume $V$ contains subensembles of identical quantum systems that do not interact with each other and that are identically oriented*. This is equivalent to saying that the Hamiltonian $\widehat{H}_j$ describing the system $j$ is identical and spatially independent, and therefore commutes with every other Hamiltonian describing systems in any subensemble. In this case, instead of working with the total dipole operator $\widehat{\boldsymbol{Q}}_\mathrm{total}$ we can instead track the statistical average behavior of each subensemble. The total polarization is then scaled by the number density $N_j \equiv M_j/V$ of each subensemble $j$ consisting of $M_j$ systems

$$P(\boldsymbol{r}, t) = \sum_j N_j \operatorname{Tr}\left[\widehat{\boldsymbol{Q}}\hat{\rho}_j(t)\right] \tag{2.35}$$

where the density matrix $\hat{\rho}$ depends on the externally-applied electric fields. Calculation of the macroscopic polarization then reduces to obtaining the average density operator evolution for a subensemble.

---

*the spatial orientation of each subensemble can be different, which is important because it allows treating arbitrarily-oriented ensembles in the same framework

## 2.6  Superoperator Description of System Evolution

The time evolution of each quantum system is described by Liouville equation (2.34) in which the system Hamiltonian $\widehat{H}$ can be split into time-dependent and independent parts

$$\widehat{H}(t) = \widehat{H}_0 + \widehat{H}_{\mathrm{I}}(t) \tag{2.36}$$

where $\widehat{H}_0$ is called the *material Hamiltonian* that models the system evolution as well as any microscopic relaxation behavior, and $\widehat{H}_{\mathrm{I}}$ is called the *interaction Hamiltonian*. It represents the perturbation of the system by a time-dependent external force. In the dipole approximation, it is simply

$$\widehat{H}_{\mathrm{I}}(t) = -\widehat{\boldsymbol{Q}} \cdot \boldsymbol{E}(t) \tag{2.37}$$

where $\boldsymbol{E}$ is an external electric field.

The material Hamiltonian can be further subdivided into several parts

$$\widehat{H}_0 = \widehat{H}_{\mathrm{system}} + \widehat{H}_{\mathrm{bath}} + \widehat{H}_{\mathrm{SB}} + \widehat{H}_{\mathrm{DC}}(\boldsymbol{E}_{\mathrm{DC}}) \tag{2.38}$$

In this equation the first term is the system Hamiltonian which includes all the degrees of freedom that must be modelled exactly. $\widehat{H}_{\mathrm{bath}}$ represents the model for relaxation processes responsible for decoherence and population relaxation that couple to the system through the system-bath coupling term $\widehat{H}_{\mathrm{SB}}$. The bath has to be treated approximately, because it has far too many degrees of freedom to include explicitly. The final term $\widehat{H}_{\mathrm{DC}}$ is a Stark effect perturbation term that parametrically dependent on an external static electric field. This term will be discussed later, in connection with the 2DESS experiment.

Instead of using the conventional density matrix formalism directly, it will be convenient to describe the time evolution of the system using superoperators. This is analogous to the transition from the wavefunction formalism to the density matrix formalism, and involves an increase of dimensionality of the description space from $N \times N$ space of the density matrices to the $N^2 \times N^2$

space of linear functionals of operators, called "superoperators." In this space, quantum operators like the density operator $\hat{\rho}$ become vectors. This increase in complexity is rewarded by a more compact and intuitive description of relaxation processes. For instance, the commutation with the Hamiltonian in equation (2.34) can be defined as a superoperator

$$\mathscr{L}\odot \Leftrightarrow [\hat{H}, \odot] = \hat{H}\odot - \odot\hat{H} \tag{2.39}$$

where $\odot$ is a placeholder for an operator[*]. We can split this total *Liouvillian superoperator* into parts using the distributivity property of commutators, and define two more superoperators called the material and interaction Liouvillians

$$\mathscr{L}_{\mathrm{mat}}\odot \Leftrightarrow [\hat{H}_0, \odot] \tag{2.40}$$

$$\mathscr{L}_{\mathrm{int}}\odot \Leftrightarrow [-\hat{Q}\cdot E(t), \odot] \tag{2.41}$$

The equation of motion for the density operator in the superoperator formalism is described by the *Liouville-von Neumann* equation which takes a form analogous to the Schrödinger equation,

$$i\hbar\frac{\partial}{\partial t}\hat{\rho}(t) = \mathscr{L}_{\mathrm{mat}}\hat{\rho}(t) + \mathscr{L}_{\mathrm{int}}(t)\hat{\rho}(t) \tag{2.42}$$

In the absence of any external perturbation ($\mathscr{L}_{\mathrm{int}} = 0$), the density operator $\hat{\rho}$ is in thermal-equilibrium. This means that it is time-independent, with population occupancy satisfying the Boltzmann distribution and having no coherence. That is[†]

$$\hat{\rho}(t) = \hat{\rho}_0 = \eta\exp\left(-\hat{H}_0/k_B T\right) \tag{2.43}$$

where $\eta$ is a normalization constant to ensure that $\mathrm{Tr}[\hat{\rho}] = 1$,

$$\eta = 1/\mathrm{Tr}\left[\exp\left(-\hat{H}_0/k_B T\right)\right] \tag{2.44}$$

---

[*]Note that on the right, we are in operator space, while on the left the operator $\odot$ is actually a vector. Thus this equation suggests an equivalence rather than an equality.

[†]this expression is in the density matrix formalism because it is easier to express this way

In this case, $(2.42)$ can be directly integrated to obtain the field-independent propagator in the Liouville representation

$$\mathcal{U}_{\text{mat}}(t) = \exp\left(-\frac{i}{\hbar}\mathcal{L}_{\text{mat}}t\right) \tag{2.45}$$

and we notice that the equilibrium density operator $\hat{\rho}_0$ commutes with this propagator $\mathcal{U}_{\text{mat}}(t)\hat{\rho}_0 = \hat{\rho}_0$.

## 2.7    *Perturbative Expansion of $\hat{\rho}$ in Liouville Space*

Having obtained the field-independent part of the propagation, we are now in a position to treat the interaction Hamiltonian as a small perturbation to the equilibrium Hamiltonian. We can expand the density operator $\hat{\rho}(t)$ in a series in powers of the interaction Hamiltonian, much the same way we expanded the polarization previously in equation $(2.5)$

$$\hat{\rho}(t) = \hat{\rho}_0 + \hat{\rho}_1(t) + \cdots + \hat{\rho}_n(t) + \cdots \tag{2.46}$$

Additionally, we take assume that at the infinitely-distant past, the bath was in thermal equilibrium, and thus $\hat{\rho}(-\infty) = \hat{\rho}_0$. This implies that all other orders $\hat{\rho}_{n\neq0}(-\infty) = 0$ and establishes a boundary condition for our expansion. By inserting $(2.46)$ into $(2.42)$ and equating orders of the field-matter interaction, we obtain a set of differential equations that approximate the evolution of the density operator

$$
\begin{aligned}
i\hbar\frac{\partial\hat{\rho}_0}{\partial t} &= \mathcal{L}_{\text{mat}}\hat{\rho}_0 \\
i\hbar\frac{\partial\hat{\rho}_1(t)}{\partial t} &= \mathcal{L}_{\text{mat}}\hat{\rho}_1(t) + \mathcal{L}_{\text{int}}\hat{\rho}_0 \\
i\hbar\frac{\partial\hat{\rho}_2(t)}{\partial t} &= \mathcal{L}_{\text{mat}}\hat{\rho}_2(t) + \mathcal{L}_{\text{int}}\hat{\rho}_1(t) \\
&\vdots \\
i\hbar\frac{\partial\hat{\rho}_n(t)}{\partial t} &= \mathcal{L}_{\text{mat}}\hat{\rho}_n(t) + \mathcal{L}_{\text{int}}\hat{\rho}_{n-1}(t)
\end{aligned}
\tag{2.47}
$$

In principle, this completes the discussion of the problem. Having obtained an approximate solution to this set of equations to a given order, $\hat{\rho}_{\sum_{j \leq n}}(t) = \hat{\rho}_0 + \hat{\rho}_1(t) + \cdots + \hat{\rho}_n(t)$, we evaluate the expectation value (2.31) and obtain an expression for the signal field via (2.23). However, it will be more convenient to solve this set of equations by transforming to a rotating coordinate frame first, called the *interaction picture*, in which these equations take a particularly compact and intuitive form.

*Interaction Picture*

To obtain a solution to the set of equations (2.47), we note that every equation has the form

$$i\hbar \frac{\mathrm{d}\hat{\rho}_n(t)}{\mathrm{d}t} = \mathcal{A}(t)\hat{\rho}_n(t) + \mathcal{B}(t)$$

where $\mathcal{A}$ and $\mathcal{B}$ are superoperators and $\hat{\rho}_n(t)$ is the $n$-th term of the expansion. This suggests that we try a solution using an integrating factor applied on the left, being careful to maintain the ordering of the operators. Calling the integrating factor $\mathcal{V}_0$, we search for a solution of the equation

$$i\hbar \frac{\mathrm{d}}{\mathrm{d}t}[\mathcal{V}_0(t)\hat{\rho}_n(t)] = i\hbar \mathcal{V}_0(t)\frac{\mathrm{d}\hat{\rho}_n(t)}{\mathrm{d}t} - \mathcal{V}_0 \mathcal{L}_{\mathrm{mat}}\hat{\rho}_n(t)$$

By expanding the differential on the right and equating terms, we obtain an equation for the integrating factor and, by direct integration, the solution

$$\frac{\mathrm{d}\mathcal{V}_0}{\mathrm{d}t} = +\frac{i}{\hbar}\mathcal{V}_0 \mathcal{L}_{\mathrm{mat}}$$

$$\mathcal{V}_0(t) = \exp[+i\mathcal{L}_{\mathrm{mat}}t/\hbar] \equiv \mathcal{U}_{\mathrm{mat}}^\dagger(t) \tag{2.48}$$

Solving the adjoint differential equation by applying a different integrating factor $\mathcal{U}_0$ on the right, we can obtain the adjoint solution

$$\mathcal{U}_0(t) = \exp[-i\mathcal{L}_{\mathrm{mat}}t/\hbar] \equiv \mathcal{U}_{\mathrm{mat}}(t) \tag{2.49}$$

These integrating factors $\mathcal{U}_{\text{mat}}$ and $\mathcal{U}_{\text{mat}}^{\dagger}$ are the forward and backward propagators in Liouville space, which represent the field-free evolution dynamics of the density operator. We can see that in a strict operator sense they satisfy the following properties,

$$\mathcal{U}_{\text{mat}}^{\dagger}(t) = (\mathcal{U}_{\text{mat}}(t))^{\dagger} = \mathcal{U}_{\text{mat}}(-t) \tag{2.50a}$$

$$\mathcal{U}_{\text{mat}}(t)\mathcal{U}_{\text{mat}}(t') = \mathcal{U}_{\text{mat}}(t + t') \tag{2.50b}$$

$$\mathcal{U}_{\text{mat}}(t)\mathcal{U}_{\text{mat}}^{\dagger}(t) = 1 \tag{2.50c}$$

We may now proceed with obtaining the solution of the perturbation expansion of $\hat{\rho}$ in terms of the factor $\mathcal{U}_{\text{mat}}^{\dagger}\hat{\rho}$,

$$i\hbar \frac{\mathrm{d}}{\mathrm{d}t}[\mathcal{U}_{\text{mat}}^{\dagger}(t)\hat{\rho}_n(t)] = \mathcal{U}_{\text{mat}}^{\dagger}(t)\mathcal{L}_{\text{int}}(t)\hat{\rho}_{n-1}(t)$$

By inserting the property (2.50c) in the expression above, we obtain an expression for a general term of the series of $\hat{\rho}_n(t)$ in the *interaction picture*,

$$i\hbar \frac{\mathrm{d}\hat{\rho}^{\mathrm{I}}_n(t)}{\mathrm{d}t} = \mathcal{L}^{\mathrm{I}}_{\text{int}}(t)\hat{\rho}^{\mathrm{I}}_{n-1}(t) \tag{2.51}$$

where I introduced the notation in the interaction picture $\hat{\rho}^{\mathrm{I}}(t) \equiv \mathcal{U}_{\text{mat}}^{\dagger}(t)\hat{\rho}(t)$ for the density operator and $\mathcal{L}^{\mathrm{I}}_{\text{int}}(t) \equiv \mathcal{U}_{\text{mat}}^{\dagger}(t)\mathcal{L}_{\text{int}}(t)\mathcal{U}_{\text{mat}}$ for the interaction Liouvillian. These definitions provide examples of transforming vectors and superoperators to the interaction picture, with the reverse transformation given by replacing $\mathcal{U}_{\text{mat}}^{\dagger} \Leftrightarrow \mathcal{U}_{\text{mat}}$. In this form we obtain the solution by direct integration,

$$\hat{\rho}^{\mathrm{I}}_n(t) = -\frac{i}{\hbar} \int_{-\infty}^{t} \mathrm{d}\tau \, \mathcal{L}^{\mathrm{I}}_{\text{int}}(\tau)\hat{\rho}^{\mathrm{I}}_{n-1}(\tau) \tag{2.52}$$

and we may transform to the density matrix space using the equivalence relation

$$\mathcal{U}_{\text{mat}}^{\dagger}(t)\hat{\rho}(t) \Leftrightarrow U_{\text{mat}}^{\dagger}(t)\hat{\rho}(t)U_{\text{mat}}(t) \tag{2.53}$$

with the definition $U_{\text{mat}}(t) \equiv \exp\left(-i\hat{H}_0 t/\hbar\right)$.
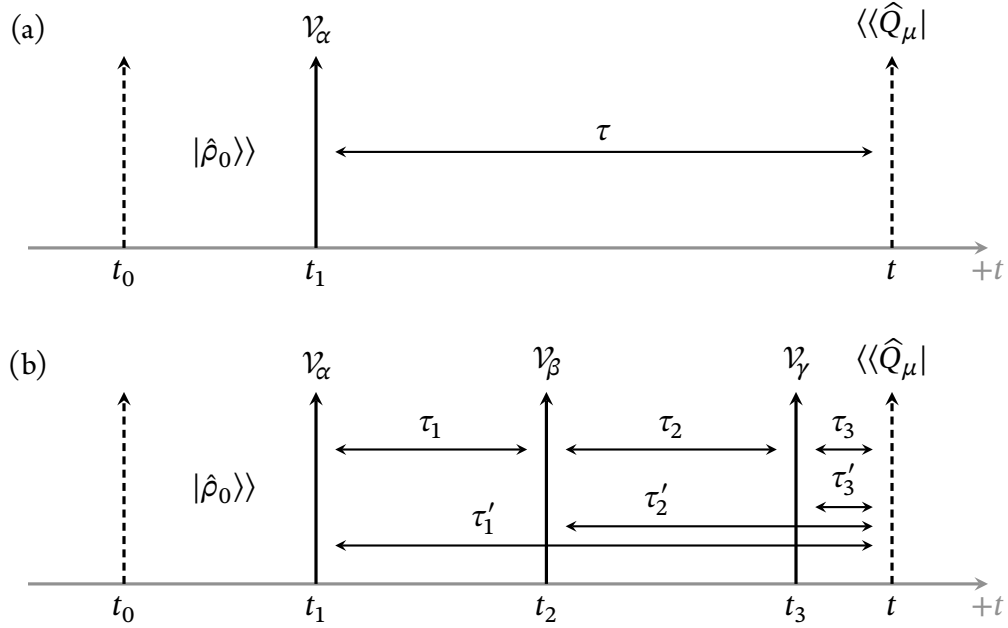
**Figure 2.1** The time-ordering of field-matter interactions for (a) the first-order response and (b) the third-order response. In the notation of the text, the time delays $\tau_n$ are the integration variables, not the location of the pulses in the field envelopes $E_\alpha$.

## 2.8 Linear and Third-order Response Functions

Having obtained a perturbative solution of the density operator $\hat\rho$ in Liouville space, we can now evaluate the terms of the polarization expansion $(2.5)$ by evaluating the expectation value in $(2.31)$ and associating each polarization term $\boldsymbol{P}_n(t)$ with the density operator expansion term $\hat\rho_n(t)^*$.

The first-order reponse is given by

$$\boldsymbol{P}^{(1)}(t) = N\left\langle\widehat{\boldsymbol{Q}}(t)\right\rangle \equiv N\langle\langle\widehat{\boldsymbol{Q}}|\hat\rho_1(t)\rangle\rangle$$

where $N$ is the number density of quantum systems in the microscopic volume, and I have introduced the double-angle notation for expressing operators as vectors in Liouville space. In order to evaluate this expectation value, we first obtain the first-order density operator $\hat\rho_1(t)$ in the

---

*for simplicity, we assume that the system consists of one subensemble, and drop the sum notation introduced in equation $(2.35)$

Schrödinger picture using (2.52),

$$|\hat{\rho}_1(t)\rangle\rangle = \mathcal{U}_{\text{mat}}(t)|\hat{\rho}^{\text{I}}_1(t)\rangle\rangle = \frac{1}{i\hbar}\int_{t_0}^{t} dt_1\, \mathcal{U}_{\text{mat}}(t)\mathcal{L}^{\text{I}}_{\text{int}}(t_1)|\hat{\rho}^{\text{I}}_0(t_1)\rangle\rangle \tag{2.54}$$

Note that in this expression, $\hat{\boldsymbol{Q}}$ is a vector quantity and that the interaction Liouvillian $\mathcal{L}^{\text{I}}_{\text{int}}$ also contains terms that are dependent on the direction and polarization of the incident field. To keep track of this, I will denote the index of the polarization vector of the polarization $\boldsymbol{P}$ as $e_\mu$ and the polarization vector of $\boldsymbol{E}$ (in the sense of (2.30)) as $e_\alpha$. Keeping this in mind, we can obtain $\boldsymbol{P}^{(1)}(t)$ as

$$P^{(1)}_\mu(t) = N\,\text{Re}\left[e^\star_\mu \frac{1}{i\hbar}\int_{t_0}^{t} dt_1\, \langle\langle \hat{Q}_\mu | \mathcal{U}_{\text{mat}}(t - t_1)\mathcal{V}_\alpha E_\alpha(t_1)|\hat{\rho}_0\rangle\rangle\right] \tag{2.55}$$

where the expression is now in the Schrödinger picture instead of the interaction picture and the notation $\mathcal{V}_\alpha \odot \Leftrightarrow [\hat{Q}_\alpha, \odot]$ was introduced to factor out the electric field dependence, and we take the real part to select the polarization $e_\mu$. By making the variable substitution $t_1 \leftrightarrow \tau$ and extending the limit $t_0 \rightarrow -\infty$, we can cast this equation to the response function form,

$$P^{(1)}_\mu(t) = N\,\text{Re}\left[e^\star_\mu \int_0^{t-t_0} d\tau\, \frac{i}{\hbar}\langle\langle \hat{Q}_\mu | \mathcal{U}_{\text{mat}}(\tau)\mathcal{V}_\alpha|\hat{\rho}_0\rangle\rangle E_\alpha(t - \tau)\right]$$

$$= \text{Re}\left[\epsilon_0 \int_{-\infty}^{\infty} d\tau\, R^{(1)}_{\mu\alpha}(\tau)e^\star_\mu(e_\alpha E(t - \tau) + \quad\text{c.c.}\quad)\right] \tag{2.56}$$

$$\text{with}\quad R^{(1)}_{\mu\alpha}(\tau) \equiv \frac{N}{\epsilon_0}\frac{i}{\hbar}\Theta(\tau)\langle\langle \hat{Q}_\mu(\tau)|\mathcal{V}_\alpha(0)\hat{\rho}_0\rangle\rangle \tag{2.57}$$

where the limits have been extended to $\pm\infty$ to match the form of (2.6) and the incident field complex polarization vector has been factored out of $E_\alpha$. Here, $\Theta$ is the Heaviside theta function, representing the causality requirement of the response function. The response function (2.57) can be put into a more familiar form in the density matrix formalism by noting that the inner product

36

in Liouville space corresponds to the trace

$$\langle\langle \widehat{Q}_\mu(\tau)|\mathcal{V}_\alpha(0)\hat{\rho}_0\rangle\rangle \Leftrightarrow \mathrm{Tr}\Big[\mathrm{U}^\dagger_{\mathrm{mat}}(\tau)\widehat{Q}_\mu \mathrm{U}_{\mathrm{mat}}(\tau)[\widehat{Q}_\alpha,\hat{\rho}_0]\Big]$$

$$= \mathrm{Tr}\Big[\widehat{Q}_\mu(\tau)\widehat{Q}_\alpha\hat{\rho}_0 - \widehat{Q}_\mu(\tau)\hat{\rho}_0\widehat{Q}_\alpha\Big]$$

$$= J(\tau) - J^\star(\tau)$$

$$\text{with} \quad J(\tau) \equiv \mathrm{Tr}\Big[\widehat{Q}_\mu(\tau)\widehat{Q}_\alpha\hat{\rho}_0\Big]$$

This demonstrates the general requirement that the response function is real reflecting the measurable nature of the polarization $\boldsymbol{P}$. The real part of the expression $(2.56)$ is taken as a mathematical convenience to project onto a Jones vector represented by $\mathrm{e}_\mu$, not because either the field nor the response is complex.

For third-order polarization, an analogous procedure leads to a response function

$$R^{(3)}_{\mu\alpha\beta\gamma}(\tau_1,\tau_2,\tau_3) \equiv \frac{N}{\epsilon_0}\left(\frac{i}{\hbar}\right)^3 \Theta(\tau_1)\Theta(\tau_2)\Theta(\tau_3) \tag{2.58}$$

$$\langle\langle\widehat{Q}_\mu|\mathcal{U}_{\mathrm{mat}}(\tau_3)\mathcal{V}_\gamma\mathcal{U}_{\mathrm{mat}}(\tau_2)\mathcal{V}_\beta\mathcal{U}_{\mathrm{mat}}(\tau_1)\mathcal{V}_\alpha|\hat{\rho}_0\rangle\rangle$$

which generates a polarization given by

$$P^{(3)}_\mu(t) = \mathrm{Re}\,\epsilon_0 \int_{-\infty}^\infty \mathrm{d}\tau_3 \int_{-\infty}^\infty \mathrm{d}\tau_2 \int_{-\infty}^\infty \mathrm{d}\tau_1\, R^{(3)}_{\mu\alpha\beta\gamma}(\tau_1,\tau_2,\tau_3)\mathrm{e}^\star_\mu \mathrm{e}_\alpha \mathrm{e}_\beta \mathrm{e}_\gamma \times$$

$$E_\alpha(t-\tau_3-\tau_2-\tau_1)E_\beta(t-\tau_3-\tau_2)E_\gamma(t-\tau_3) \tag{2.59}$$

$$+ \quad \text{c.c.}$$

These equations represent the link between the microscopic description of matter using the density operator and the macroscopic measured field, obtained through the polarization component $P^{(3)}_\mu$. The response is causal as required by the form of $(2.7)$, but is not in the independent convolutional form. This defect is superficial, as can be seen by making the substitutions $\tau'_2 \leftrightarrow \tau_3 + \tau_2$ and $\tau'_1 \leftrightarrow \tau_1 + \tau_2 + \tau_3$. By the definitions of the intervals, the response function will still vanish for any $\tau'_n \leq 0$.

As before, we may demonstrate that the third-order response is causal by splitting it into several response functions $\boldsymbol{R}_k^{(3)}$ and their complex conjugates. To do this, we repeatedly substitute the propagator identity (2.50c) into (2.58) and transform the dipole operators to the interaction picture, indicated by the time-dependence of $\hat{Q}$ and $\mathcal{V}$. This readily yields the definitions of $\boldsymbol{R}_k^{(3)}$

$$R_{\mu\alpha\beta\gamma}^{(3)}(\tau_1', \tau_2', \tau_3') = \frac{N}{\epsilon_0}\left(\frac{i}{\hbar}\right)^3 \Theta(\tau_1' - \tau_2')\Theta(\tau_2' - \tau_3')\Theta(\tau_3') \sum_{k=1}^{4} \left[R_{k,\mu\alpha\beta\gamma} - R_{k,\mu\alpha\beta\gamma}^{\star}\right] \quad \text{(2.60a)}$$

$$\text{with} \quad R_{1,\mu\alpha\beta\gamma} = \text{Tr}\left[\hat{Q}_\beta(\tau_1' - \tau_2')\hat{Q}_\gamma(\tau_1' - \tau_3')\hat{Q}_\mu(\tau_1')\hat{Q}_\alpha(0)\hat{\rho}_0\right] \quad \text{(2.60b)}$$

$$R_{2,\mu\alpha\beta\gamma} = \text{Tr}\left[\hat{Q}_\alpha(0)\hat{Q}_\gamma(\tau_1' - \tau_2')\hat{Q}_\mu(\tau_1')\hat{Q}_\beta(\tau_1' - \tau_3')\hat{\rho}_0\right] \quad \text{(2.60c)}$$

$$R_{3,\mu\alpha\beta\gamma} = \text{Tr}\left[\hat{Q}_\alpha(0)\hat{Q}_\beta(\tau_1' - \tau_2')\hat{Q}_\mu(\tau_1')\hat{Q}_\gamma(\tau_1' - \tau_3')\hat{\rho}_0\right] \quad \text{(2.60d)}$$

$$R_{4,\mu\alpha\beta\gamma} = \text{Tr}\left[\hat{Q}_\mu(\tau_1')\hat{Q}_\gamma(\tau_1' - \tau_3')\hat{Q}_\beta(\tau_1' - \tau_2')\hat{Q}_\alpha(0)\hat{\rho}_0\right] \quad \text{(2.60e)}$$

In the 2DES literature these pathways are commonly represented in graphical form using the double-sided Feynman diagram formalism[2], depicted in Figure 2.2. They portray the interaction of the field with density matrix elements at sequential time intervals. Here, the initial state is represented as a density matrix element $|a\rangle\langle a|$ at the bottom of the diagram, an element of the thermally equilibrated density matrix $\hat{\rho}_0$. Each field-matter interaction represented as a line on the left (ket) or right (bra) side causes the density matrix element to evolve for the time interval until the next interaction. Because the field-matter interaction Hamiltonian depends on the electric field, each wiggly line is linked to an electric polarization vector $\boldsymbol{e}$ and wavevector $\boldsymbol{k}$. The resulting total wavevector $\boldsymbol{k}$ must satisfy the phase-matching conditions for bulk samples. In this way, each diagram allows one to track the resulting polarization component and the effect of the propagator $U_{\text{mat}}$, making it a useful graphical tool for interpreting 2D electronic spectra.

## 2.9  Modeling of a Realistic System

In the previous sections, we developed a theory that links the microscopic behavior of an ensemble of quantum systems in a small volume $V$ to the macroscopic polarization that leads to nonlinear
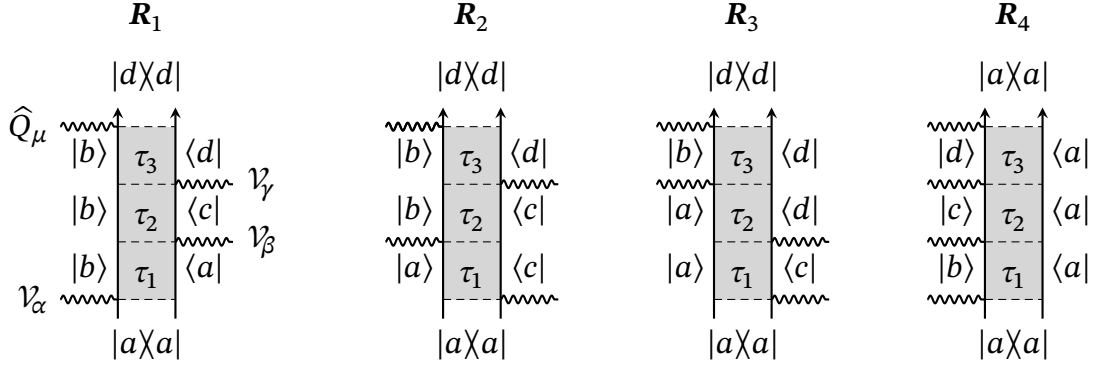
**Figure 2.2** Feynman diagrams for general third-order signal in a multi-level system. Each field-matter interaction represented as ⌇ acts on the left or right of the density matrix to cause a transition to a population $|a\rangle\langle a|$ or a coherence $|a\rangle\langle b|$. Because each action on the right corresponds to choosing the negative part of the commutator, there is an overall $(-1)^n$ factor for each diagram, where $n$ is the number of interactions from the right. The time intervals between interactions are represented as $\tau_n$.

optical effects. We were able to reach this point without specifying much detail about the system itself, other than to split the total Hamiltonian $\widehat{H}$ based on time-dependence.

In reality, condensed-phase systems are far too complex to treat fully quantum-mechanically due to the near-infinite number of degrees of freedom that would be required. Instead, the system is partitioned into a set of discrete quantum-mechanical states that are treated exactly and a continuum of states that are modeled by statistical mechanics methods using projection operator techniques. This approach allows an immense simplification of the modelling, because only the aggregate behavior of the continuum states must be traced, which take the form of $n$-time correlation functions. The disadvantage is that this is inherently an approximation process, analogous to replacing an unknown distribution function by a finite number of moments. Even with this simplification, only a few analytically-tractable solutions exist. This thesis will deal with only one, called the Brownian Oscillator model, for which the bath is modelled as an infinite number of harmonic oscillators. There is excellent literature which deals with these topics in detail[2,7]. Here I sketch the outline of the procedure.

*Material Hamiltonian Revisited*

Let us take a model of the total Hamiltonian in the Brownian oscillator form[2,8],

$$\widehat{H}_S = \frac{\hat{p}}{2m} + V(\hat{x}) \tag{2.61}$$

$$\widehat{H}_I = W(\hat{x}, t) \tag{2.62}$$

$$\widehat{H}_B = \sum_\alpha \frac{\hat{p}_\alpha}{2m_\alpha} + \frac{1}{2}m_\alpha \omega_\alpha \hat{x}_\alpha^2 \tag{2.63}$$

$$\widehat{H}_{SB} = -\hat{x} \sum_\alpha c_\alpha \hat{x}_\alpha \tag{2.64}$$

$$\widehat{H}_{ren} = \frac{1}{2}\hat{x}^2 \sum_\alpha \frac{c_\alpha^2}{m_\alpha \omega_\alpha^2} \tag{2.65}$$

Here, our system of interest is represented by $\widehat{H}_S$, while the bath is a large number of harmonic oscillators $\widehat{H}_B$, represented with operators with the $\alpha$ subscripts. We assume that the coupling is linear between the system and the bath with the coupling strength $c_\alpha$. In comparison to (2.38), we have added an extra term called the renormalization Hamiltonian that represents the energy shift that the system experiences when put in contact with the bath. It is required so that the system satisfies the Quantum Langevin equation[8]. As usual, $\widehat{H}_I$ represents the field-matter interaction and is left in a general form.

The popularity of this model rests on the fact that for an arbitrary potential, the evolution of this system is exactly solvable. In fact, the bath behavior is completely characterized by a function called the *bath spectral density*, defined as

$$J(\omega) = \pi \sum_\alpha \frac{c_\alpha^2}{2m_\alpha \omega_\alpha}(\delta(\omega - \omega_\alpha) - \delta(\omega + \omega_\alpha)) \tag{2.66}$$

while the renormalization Hamiltonian is simply

$$\widehat{H}_{ren} = \frac{1}{2}\lambda \hat{x}^2 \tag{2.67}$$

$$\text{with} \quad \lambda \equiv \int_{-\infty}^{\infty} \frac{d\omega}{2\pi} \frac{J(\omega)}{\omega} \tag{2.68}$$

In the spectroscopy literature, $\lambda$ is often referred to as the reorganization energy.

If we assume that the system is initially in the ground state which includes the reorganization energy and the bath is in thermal equilibrium (see (2.43)), we may trace out the bath degrees of freedom and, in the limit of weak system-bath coupling, obtain a complex correlation function

$$C(t) = \int_{-\infty}^{\infty} \frac{d\omega}{2\pi} J(\omega) \cos(\omega t) \coth\left(\frac{\beta\hbar\omega}{2}\right) - i \int_{-\infty}^{\infty} \frac{d\omega}{2\pi} J(\omega) \sin(\omega t) \tag{2.69}$$

This correlation function represents the modulation of the energy gap between the ground state and the excited states by the bath. Looking at only the ground and first excited state that we now label as $g$ and $e$ respectively, it can be shown that the auxiliary response functions take the form[2]

$$R_{1,\mu\alpha\beta\gamma} = \hat{Q}_\alpha \hat{Q}_\beta \hat{Q}_\gamma \hat{Q}_\mu \exp(-i\omega_{eg}\tau_1 - i\omega_{eg}\tau_3)$$
$$\times \exp\left(-g^\star(\tau_3) - g(\tau_1) - f_+(\tau_3, \tau_2, \tau_1)\right) \tag{2.70}$$

$$R_{2,\mu\alpha\beta\gamma} = \hat{Q}_\alpha \hat{Q}_\beta \hat{Q}_\gamma \hat{Q}_\mu \exp(i\omega_{eg}\tau_1 - i\omega_{eg}\tau_3)$$
$$\times \exp\left(-g^\star(\tau_3) - g(\tau_1) + f_+^\star(\tau_3, \tau_2, \tau_1)\right) \tag{2.71}$$

$$R_{3,\mu\alpha\beta\gamma} = \hat{Q}_\alpha \hat{Q}_\beta \hat{Q}_\gamma \hat{Q}_\mu \exp(i\omega_{eg}\tau_1 - i\omega_{eg}\tau_3)$$
$$\times \exp\left(-g(\tau_3) - g^\star(\tau_1) + f_-^\star(\tau_3, \tau_2, \tau_1)\right) \tag{2.72}$$

$$R_{4,\mu\alpha\beta\gamma} = \hat{Q}_\alpha \hat{Q}_\beta \hat{Q}_\gamma \hat{Q}_\mu \exp(-i\omega_{eg}\tau_1 - i\omega_{eg}\tau_3)$$
$$\times \exp\left(-g(\tau_3) - g^\star(\tau_1) - f_-(\tau_3, \tau_2, \tau_1)\right) \tag{2.73}$$

$$\text{with} \quad f_\pm(\tau_3, \tau_2, \tau_1) \equiv g^{(\star,)}(\tau_2) - g^{(\star,)}(\tau_2 + \tau_3) - g(\tau_1 + \tau_2) + g(\tau_1 + \tau_2 + \tau_3) \tag{2.74}$$

$$g(t) \equiv \int_0^t dt' \int_0^{t'} dt'' \frac{C(t'')}{\hbar^2} \tag{2.75}$$

In particular, all of the time-dependence is encoded in an exponential pre-factor dependent on the coherence times $\tau_1$ and $\tau_3$, which gets modulated by a factor dependent on the bath correlation function through the lineshape function $g(t)$. In the case that the system-bath coupling is $J(\omega) = 0$, this modulating factor reduces to unity and the response functions simply oscillate at the electronic gap frequency. Conversely, a sharp feature in the spectral density will show up

41

as an additional resonance in this pre-factor*. This property is useful for including vibrational modes into the 2D spectrum at a small computational cost. The disadvantage of this approach is that because the bath modes are independent in the linear-coupling limit, coherences between vibrational modes cannot be modeled in this way.

In this section I have described a simple model for relaxation of a particle coupled to a harmonic bath at thermal equilibrium. This model illustrates the advantages of using a harmonic bath representation, but is too simple to describe the dynamics of realistic quantum systems. Instead, a multimode Brownian oscillator model is typically used[2]. In this model, each quantum system is represented as a two-level system representing the electronic ground and excited state. By invoking the *Born-Oppenheimer* (adiabatic) approximation, the vibrational levels are factored out of the electronic wavefunctions and are modeled as sets of harmonic oscillators. These sets are sometimes referred to as *primary oscillators*. The bath is of the same harmonic oscillator form as described above, but it now couples to the vibrational levels in both the ground and excited state. The *Franck-Condon* approximation is also used to assume that the dipole operator by which the optical field couples to the system is independent of vibrational degrees of freedom. This model has a convenient generalized form for multiple sites with independent bath-coupling that is used to perform the simulations in the following chapter of this thesis.

Some comments about this model are in order. This model relies on the termination of the cumulant expansion which restricts the use of this model to linear coupling in the bath degrees of freedom. As pointed out in[8], this does not necessarily imply that the bath of harmonic oscillators represent any specific harmonic degrees of freedom, but rather that to first order in coupling one cannot tell the difference. Several workers have pointed out that this approximation may not be valid for many experimentally interesting systems. It is an exciting field of research to obtain an accurate and computationally efficient method for modeling realistic systems that is not limited

---

*This can be seen by substituting the definition of $J(\omega)$ into the correlation function and looking at the imaginary part. A delta function at frequency $\omega_r$ will produce a resonance in the lineshape.

in this way.

*Phase-matched Signals and the Rotating Wave Approximation*

Having obtained a reasonable model for the quantum system, we are now in a position to determine the form of the third-order polarization $P^{(3)}$. To do this, let us assume that the electric field that induces this nonlinear polarization is the sum of three driving fields of the quasi-monochromatic plane-wave form which are all approximately resonant with the electronic transition frequency $\omega_0 \approx \omega_{eg}$ and are differentiated by their polarization and wavevector.

Each field can be represented in the form

$$E_n(r, t) = e_n A_n(t - k_n \cdot r/\omega_0 - i\phi_n) \exp(ik_n \cdot r_n - i\omega_0 t) + \text{c.c.}$$

$$= e_n \tilde{A}_n(t, r) \exp(-i\omega_0 t) \exp(-i\phi_n) + \text{c.c.} \tag{2.76}$$

where for the $n$-th pulse, $A$ is a real pulse envelope centered at $t = 0$ and $e$ is the polarization vector of the field. We also allow the field to have an arbitrary phase-shift $\phi$. Experimentally, it is convenient to define all pulse envelopes with respect to a common time-origin, such that each pulse has a fixed time-delay $t'$, being careful to track the additional carrier phase-shift of $\exp(i\omega_0 t')$ caused by the translation of the envelope when we do this[9]. For a third-order experiment, we have three unique time-delays $(\tau_a = \tau + T + t', \tau_b = T + t', \tau_c = t')$ expressed in terms of the delay between the centers of each pair of envelopes ($\tau$, $T$, and $t'$). Because each pulse has a finite bandwidth, the convolution of (2.9) will result in signals that come from regions of pulse overlap for which the order of interaction is not the same as that given by the delays. This phenomenon is referred to as *pulse-overlap effects*.

Upon substitution of the total field $E(t) = \sum_n E_n(t)$ into (2.59)[10], we find that the resulting polarization integral contains terms with phase-factors oscillating at $\omega_s = \pm\omega_0 \pm \omega_0 \pm \omega_0$ that come from the interference of the three driving fields multiplied by the propagation factors

$\exp(-i\omega_{eg}(\tau_1 \pm \tau_3))$. Many terms will interfere constructively to generate highly-oscillating integrands that have a much smaller contribution to the integral than slowly-varying terms and can be neglected. Using this fact we can drop all terms with phase-factors different from $\exp(\pm i\omega_0 t)$. This is called the rotating-wave approximation (RWA) and it considerably reduces the number of signals that we must consider. Also note that the final time-delay $t'$ is a free parameter, and we can set it to zero.

The third-order polarization can then be written in the form[11]

$$\boldsymbol{P}^{(3)}(\tau, T, t) = \exp(-i\omega_0(t - \tau)) \int_{-\infty}^{\infty} d\tau_3 \int_{-\infty}^{\infty} d\tau_2 \int_{-\infty}^{\infty} d\tau_1$$

$$S_{\boldsymbol{k}_I}(\tau_1, \tau_2, \tau_3) \times \left[ E_1^{\star(\tau_a)} E_2^{(\tau_b)} E_3^{(\tau_c)} + E_1^{\star(\tau_a)} E_3^{(\tau_b)} E_2^{(\tau_c)} \right] \exp(i\omega_0(\tau_3 - \tau_1))$$

$$+ S_{\boldsymbol{k}_{II}}(\tau_1, \tau_2, \tau_3) \times \left[ E_2^{(\tau_a)} E_1^{\star(\tau_b)} E_3^{(\tau_c)} + E_3^{(\tau_a)} E_1^{\star(\tau_b)} E_2^{(\tau_c)} \right] \exp(i\omega_0(\tau_3 + \tau_1))$$

$$+ S_{\boldsymbol{k}_{III}}(\tau_1, \tau_2, \tau_3) \times \left[ E_2^{(\tau_a)} E_3^{(\tau_b)} E_1^{\star(\tau_c)} + E_3^{(\tau_a)} E_2^{(\tau_b)} E_1^{\star(\tau_c)} \right] \exp(i\omega_0(\tau_3 + 2\tau_2 + \tau_1)) \quad (2.77)$$

where $S_{\boldsymbol{k}_I}^{(3)} \equiv -R_1^{\star} + R_2 + R_3$, $S_{\boldsymbol{k}_{II}}^{(3)} \equiv -R_2^{\star} + R_1 + R_4$, $S_{\boldsymbol{k}_{III}}^{(3)} \equiv -R_3^{\star} + R_4$ are the called the system response functions for the rephasing ($\boldsymbol{k}_I$), non-rephasing ($\boldsymbol{k}_{II}$), and double-quantum ($\boldsymbol{k}_{III}$) pathways, and the superscript with a time-delay represents the time-ordering of each pulse interaction*. The full expressions for these response functions can be found elsewhere[11].

As before we can express the interaction sequences graphically using double-sided Feynman diagrams (see Figure 2.3). However, now each group of response function takes on a specific physical meaning: excited state absorption (ESA, diagrams corresponding to $-R_1^{\star}$ and $-R_2^{\star}$), stimulated emission (SE, diagrams $R_1$ and $R_2$), ground state bleach (GB, diagrams $R_3$ and $R_4$), and double-quantum coherence (DQC, diagrams $R_3^{\star}$ and $R_4$). Though not discussed in this thesis, we may also represent incoherent population transfer between excited states during the population time $T$ as Feynman diagrams[12]. The double-quantum pathways are not probed in this work, and we will ignore them for the rest of the thesis.

---

*To simplify the expression we have dropped the tensorial nature of these interactions, but it can easily be reconstructed by selecting the appropriate tensor elements of each $S^{(3)}$ and inserting $e$ for each field.

**(a)** $\mathbf{k}_I = -\mathbf{k}_\alpha + \mathbf{k}_\beta + \mathbf{k}_\gamma$

ESA $|e_i\rangle\langle e_i|$  SE $|g\rangle\langle g|$  GSB $|g\rangle\langle g|$  ESA' $|e_j\rangle\langle e_j|$  SE' $|g\rangle\langle g|$

$\mathbf{k}_s$, $\mathbf{k}_\gamma$, $\mathbf{k}_\beta$, $\mathbf{k}_\alpha$

ESA: $|f_k\rangle$ $\tau_3$ $\langle e_i|$ ; $|e_j\rangle$ $\tau_2$ $\langle e_i|$ ; $|g\rangle$ $\tau_1$ $\langle e_i|$ — $|g\rangle\langle g|$

SE: $|e_j\rangle$ $\tau_3$ $\langle g|$ ; $|e_j\rangle$ $\tau_2$ $\langle e_i|$ ; $|g\rangle$ $\tau_1$ $\langle e_i|$ — $|g\rangle\langle g|$

GSB: $|e_j\rangle$ $\tau_3$ $\langle g|$ ; $|g\rangle$ $\tau_2$ $\langle g|$ ; $|g\rangle$ $\tau_1$ $\langle e_i|$ — $|g\rangle\langle g|$

ESA': $|f_k\rangle$ $\tau_3$ $\langle e_j|$ ; $|e_j\rangle$ $|e_i\rangle$ $\tau_2$ $|e_j\rangle$ $|e_i\rangle$ ; $|g\rangle$ $\tau_1$ $\langle e_i|$ — $|g\rangle\langle g|$

SE': $|e_j\rangle$ $\tau_3$ $\langle g|$ ; $|e_j\rangle$ $|e_i\rangle$ $\tau_2$ $|e_j\rangle$ $|e_i\rangle$ ; $|g\rangle$ $\tau_1$ $\langle e_i|$ — $|g\rangle\langle g|$

**(b)** $\mathbf{k}_{II} = \mathbf{k}_\alpha - \mathbf{k}_\beta + \mathbf{k}_\gamma$

ESA $|e_j\rangle\langle e_j|$  SE $|g\rangle\langle g|$  GSB $|g\rangle\langle g|$  ESA' $|e_j\rangle\langle e_j|$  SE' $|g\rangle\langle g|$

$\mathbf{k}_s$, $\mathbf{k}_\gamma$, $\mathbf{k}_\beta$, $\mathbf{k}_\alpha$

ESA: $|f_k\rangle$ $\tau_3$ $\langle e_j|$ ; $|e_j\rangle$ $\tau_2$ $\langle e_j|$ ; $|e_i\rangle$ $\tau_1$ $\langle g|$ — $|g\rangle\langle g|$

SE: $|e_i\rangle$ $\tau_3$ $\langle g|$ ; $|e_i\rangle$ $\tau_2$ $\langle e_j|$ ; $|e_i\rangle$ $\tau_1$ $\langle g|$ — $|g\rangle\langle g|$

GSB: $|e_j\rangle$ $\tau_3$ $\langle g|$ ; $|g\rangle$ $\tau_2$ $\langle g|$ ; $|e_i\rangle$ $\tau_1$ $\langle g|$ — $|g\rangle\langle g|$

ESA': $|f_k\rangle$ $\tau_3$ $\langle e_j|$ ; $|e_j\rangle$ $|e_i\rangle$ $\tau_2$ $|e_j\rangle$ $|e_i\rangle$ ; $|g\rangle$ $\tau_1$ $\langle e_i|$ — $|g\rangle\langle g|$

SE': $|e_j\rangle$ $\tau_3$ $\langle g|$ ; $|e_j\rangle$ $|e_i\rangle$ $\tau_2$ $|e_j\rangle$ $|e_i\rangle$ ; $|e_i\rangle$ $\tau_1$ $\langle e_i|$ — $|g\rangle\langle g|$

**(b)** $\mathbf{k}_{III} = \mathbf{k}_\alpha + \mathbf{k}_\beta - \mathbf{k}_\gamma$

DQC1 $|e_j\rangle\langle e_j|$  DQC2 $|g\rangle\langle g|$

$\mathbf{k}_s$, $\mathbf{k}_\gamma$, $\mathbf{k}_\beta$, $\mathbf{k}_\alpha$

DQC1: $|f_k\rangle$ $\tau_3$ $\langle e_j|$ ; $|f_k\rangle$ $\tau_2$ $\langle g|$ ; $|e_i\rangle$ $\tau_1$ $\langle g|$ — $|g\rangle\langle g|$

DQC2: $|e_j\rangle$ $\tau_3$ $\langle g|$ ; $|f_k\rangle$ $\tau_2$ $\langle g|$ ; $|e_i\rangle$ $\tau_1$ $\langle g|$ — $|g\rangle\langle g|$
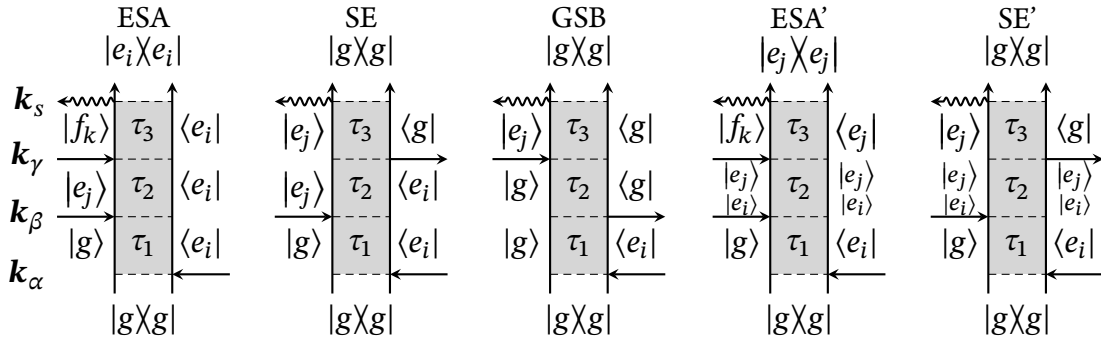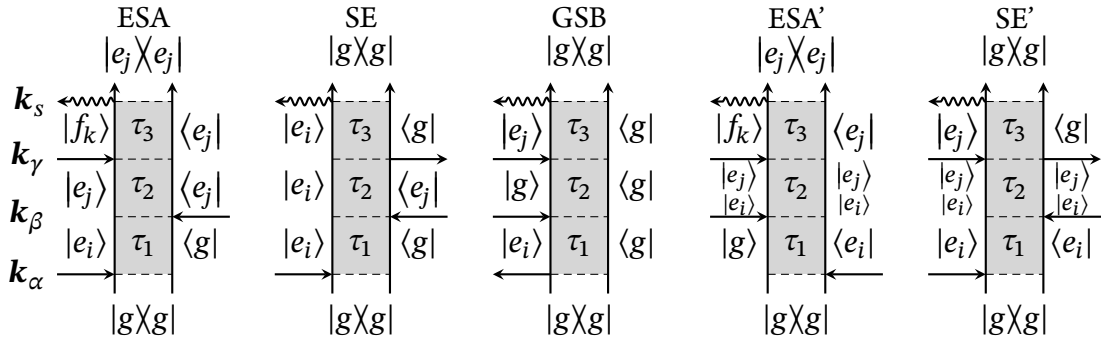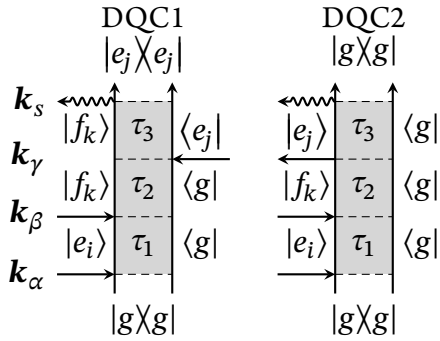
**Figure 2.3** Double-sided Feynman diagrams after the rotating wave approximation. Contributions to the (a) rephasing $\mathbf{k}_I$, (b) nonrephasing $\mathbf{k}_{II}$, and (c) double-quantum $\mathbf{k}_{III}$ phase-matched direction is shown. Population transfer diagrams are indicated with a quote. The Greek indices are used to label the field polarizations.

*Rotational Averaging*

In this chapter we have emphasized the vectorial nature of the response function by including the Greek indexes representing the components of the dipole operator in the molecular frame. Unless the sample is macroscopically oriented such as in a crystal, each subpopulation of molecules can be arbitrarily oriented with respect to the laboratory frame. On the other hand, it is far more convenient to define the optical field properties (the propagation vector $k_s$ and the polarization vector $e$) in the laboratory frame. Therefore, in order to properly calculate the generated polarization, we must rotate each subpopulation to the laboratory frame and then calculate the interaction Hamiltonian term. The macroscopic polarization is then the orientational average given by (2.35). For an arbitrary distribution of orientations, this average must be performed numerically and is computationally expensive. However, in the isotropically oriented case that we have been considering, the use of the Brownian oscillator model and the resulting correlation functions allow for a convenient simplification.

As can be seen from the form of the response function above, using the lineshape functions allowed us to pull the dependence on the dipole operator out of the trace expressions in (2.60). Each response function has a factor of the form

$$\hat{Q}_\mu \hat{Q}_\alpha \hat{Q}_\beta \hat{Q}_\gamma \equiv \langle (\hat{Q}_4 \cdot e_4^\star)(\hat{Q}_1 \cdot e_1)(\hat{Q}_2 \cdot e_2)(\hat{Q}_3 \cdot e_3) \rangle$$

where the angular brackets represent an average over the distribution of molecular orientations. To perform the rotational average we must apply a matrix transformation to align the each molecular coordinate frame to the lab frame, and integrate over 3 Euler angles. The resulting value acts as a scaling factor for each set of dipole operators, which are then summed to obtain the total response function. These integrals turn out to possess a fair bit of symmetry, so that for a given set of polarization vectors the high-order integration reduces to a few dot-products[13]. For example, for the common case that all of the polarization vectors are linearly polarized and equal

$(e_1 = e_2 = e_3 = e_4)$, the rotationally averaged factor reduces to

$$\langle(\hat{Q}_4 \cdot e_4^\star)(\hat{Q}_1 \cdot e_1)(\hat{Q}_2 \cdot e_2)(\hat{Q}_3 \cdot e_3)\rangle =$$
$$\frac{1}{15}\big[(\hat{Q}_1 \cdot \hat{Q}_2)(\hat{Q}_3 \cdot \hat{Q}_4) + (\hat{Q}_1 \cdot \hat{Q}_3)(\hat{Q}_2 \cdot \hat{Q}_4) + (\hat{Q}_1 \cdot \hat{Q}_4)(\hat{Q}_2 \cdot \hat{Q}_3)\big]$$

while for the other common case where the pump pulses and probe pulses are perpendicular the scaling factor is instead

$$(\hat{Q}_4 \cdot e_4^\star)(\hat{Q}_1 \cdot e_1)(\hat{Q}_2 \cdot e_2)(\hat{Q}_3 \cdot e_3)\rangle =$$
$$\frac{1}{30}\big[4(\hat{Q}_1 \cdot \hat{Q}_2)(\hat{Q}_3 \cdot \hat{Q}_4) - (\hat{Q}_1 \cdot \hat{Q}_3)(\hat{Q}_2 \cdot \hat{Q}_4) - (\hat{Q}_1 \cdot \hat{Q}_4)(\hat{Q}_2 \cdot \hat{Q}_3)\big]$$

Note that the first term in both expressions appears with a positive sign, while the remaining terms have opposite signs. By performing both measurements and combining the results one can select the term in which the first two and last two interactions occur with pairwise aligned dipoles[14]. This is the basis of polarization selection for 2DES spectroscopy, which has been used to enhance weak features in 2D spectra[3,15].

One caveat to this approach is that this analytic rotational averaging approach requires that all of the orientation-dependence can be lumped into a limited number of dipole-dipole terms in the interaction Hamiltonian. This is not an issue for typical 2D experiments, however this assumption breaks down for cases in which the field-matter interaction cannot be treated perturbatively. As will be described in the following section on 2D electronic Stark spectroscopy, the system eigenstates are shifted by a large static electric field called the Stark field. The magnitude of this shift is dependent on the molecular orientation which causes different dephasing and relaxation rates in subpopulations. Therefore a more complicated orientational average integral must be calculated and must be calculated numerically in general.

## 2.10 2DES and Associated Spectroscopies

As discussed in the introduction, 2D electronic spectroscopy is an effective technique for reconstructing the molecular environment and correlations within a sample. In this third-order experiment, a three pulses of fixed time delays interact sequentially with the sample, moving it first through a coherence (during interval $\tau$), then a population ($T$), and finally another coherence ($t$), generating a time-dependent third-order polarization. For this reason, the time-delays are conventionally referred to as the coherence time $\tau$, the population time $T$, and the detection time $t$. This process generates the rephasing, non-rephasing, and double-quantum signals in unique directions given by phase-matching. The resulting signal is Fourier-transformed along $\tau \mapsto \omega_\tau$ and $t \mapsto \omega_t$ and is presented as a two-dimensional correlation map as a function of population time $T$. The details of the experimental aspects of this procedure is discussed in Chapter 4. Here I will discuss the graphical interpretation of the generated rephasing and non-rephasing signals denoted $S_{\mathrm{RE}}^{(3)}(-\omega_\tau, T, \omega_t)$ and $S_{\mathrm{NR}}^{(3)}(\omega_\tau, T, \omega_t)$ for the case of a few simple systems and probed with delta-function pulses.

As can be seen from the Feynman diagrams in Figure 2.3, the rephasing and non-rephasing signals differ in the order of the first two interactions. In the impulsive limit, the rephasing signal is proportional to ($\tau > 0$)

$$S_{\mathrm{RE}}^{(3)}(\omega_\tau, T, \omega_t) \propto \int_0^\infty \mathrm{d}\tau \exp(i\omega_\tau \tau) \int_{-\infty}^\infty \mathrm{d}t \exp(i\omega_t t) S_{\boldsymbol{k}_I}(\tau, T, t) \qquad (2.78)$$

while the nonrephasing signal is given by ($\tau < 0$)

$$S_{\mathrm{NR}}^{(3)}(\omega_\tau, T, \omega_t) \propto \int_0^\infty \mathrm{d}\tau \exp(i\omega_\tau \tau) \int_{-\infty}^\infty \mathrm{d}t \exp(i\omega_t t) S_{\boldsymbol{k}_{II}}(\tau, T, t) \qquad (2.79)$$

Note that in both cases, the detected signal is phase-matched in the rephasing direction $\boldsymbol{k}_I$. This is used in experiment to spatially select the rephasing signal. Simply scanning over negative $\tau$ yields the non-rephasing signal as well. Using this information and the Feynmann diagrams we

can predict the location of peaks in the rephasing and non-rephasing spectra by simply looking at the first and last coherences in a diagram. This technique is called *diagramatic perturbation theory*.

For a two-level system, the only terms that survive in both the rephasing and nonrephasing spectra are the SE and GSB terms, reflecting the dynamics on the excited state and the ground-state, respectively. For the rephasing signals with no population relaxation, the ground-state and excited state signals are identical and show up at $-\omega_\tau = \omega_t$. The nonrephasing signals will be identical, but mirrored over the $\omega_t$ axis.

In addition to identifying the location of a peak, two-dimensional spectra contain rich information about the local environment. At short population times, the diagonal width corresponds to inhomogeneous broadening, reflecting the distribution of local environments causing shifts in the energy gap. The anti-diagonal width at early times contains information about the homogeneous linewidth, the dephasing rate of the excited state[2,3]. At long waiting times, the peaks broaden and become symmetrical, indicating a loss of correlation.

## 2.11   2DESS Theory

We have described the origin of first- and third-order signals observed in optical spectroscopy, as well as sketched out an approach typically used to model these signals theoretically. To describe 2DESS it is necessary for us to understand the effect of a large static DC field on these signals encoded as the $\widehat{H}_{\mathrm{DC}}$ term in the material Hamiltonian. For this work, we assume that the sample is a set of neutral, polarizable molecules that are fixed in a passive matrix. This is a good assumption for the experiments of the following chapters in which neutral systems of interest are immobilized in a glassy matrix in liquid nitrogen. The effect of the Stark perturbation term on a single molecule can be modeled to second-order in the field as

$$\widehat{H}_{\mathrm{DC}}(\boldsymbol{E}_{\mathrm{DC}}) = -\widehat{\boldsymbol{\mu}} \cdot \boldsymbol{E}_{\mathrm{DC}} - \frac{1}{2}\boldsymbol{E}_{\mathrm{DC}} \cdot \widehat{\boldsymbol{\alpha}} \cdot \boldsymbol{E}_{\mathrm{DC}} \tag{2.80}$$

where $\hat{\boldsymbol{\mu}}$ is the static dipole operator and $\hat{\boldsymbol{\alpha}}$ is the second-rank tensor polarizability operator. For convenience, we assume that in the energy basis the operators are diagonal and simply result in an orientation-dependent energy shift of the field-free eigenstates. The spectroscopically relevant quantity is the difference in permanent dipole moment and polarizability between the excited state and the ground state, which results in an orientation-dependent shift of the absorption peak of the form

$$\langle \Delta \hbar \omega_{eg} \rangle = \langle -(\hat{\boldsymbol{\mu}}_{ee} - \hat{\boldsymbol{\mu}}_{gg}) \cdot \boldsymbol{E}_{\mathrm{DC}} - \frac{1}{2}(\hat{\boldsymbol{\alpha}}_{ee} - \hat{\boldsymbol{\alpha}}_{gg}) : \boldsymbol{E}_{\mathrm{DC}} \boldsymbol{E}_{\mathrm{DC}} \rangle \qquad (2.81)$$

where the $\langle \rangle$ brackets indicate that a rotational average must be performed. In an isotropic immobilized sample this rotational average causes a mixing of the $\hat{\boldsymbol{\mu}}$ and $\hat{\boldsymbol{\alpha}}$ terms such that the total field dependence is quadratic[16].

In the case of linear absorption, it was first shown by Liptay[17] that the resulting differential field-on/field-off (Stark) absorption spectrum can be expressed in terms of derivatives of the field-off absorption spectrum scaled by factors of $\hat{\boldsymbol{\mu}}$ and $\hat{\boldsymbol{\alpha}}$ (see[16] for explicit expressions for the lineshapes). In particular, first-derivative lineshapes are associated with changes in polarizability $\Delta \hat{\boldsymbol{\alpha}}$, while second-derivatives correspond to differences in the dipole moment $\Delta \hat{\boldsymbol{\mu}}$. Further, the signal amplitude depends on the dot-product of the polarization of the optical field and the Stark field. This allows one to determine the relative orientation between transition and dipole moments.

Liptay used this approach to investigate the effects of solvation on absorption spectra in small molecules. Since then, this approach has been successfully applied to study charge-transfer processes in organic and photovoltaic systems. Much of the recent work in this area has been carried out by Boxer and coworkers[18].

The success of the lineshape approach relies on the clean separation of absorption bands, which facilitates fitting the Stark spectrum to derivatives of those bands. In the case of closely-spaced levels such as in photosynthetic antennae complexes[19] or reaction centers[20], it is no

longer possible to unambiguously separate the contributions from $\Delta\hat{\boldsymbol{\mu}}$ and $\Delta\hat{\boldsymbol{\alpha}}$ terms because cross-terms show up that continuously interpolate between these two regimes. This was demonstrated by Somsen and coworkers[19], who treated the Stark perturbation in the same way as an optical field interaction in a third-order process with two DC field-matter interactions, $\chi^{(3)}(-\omega_s; \omega, 0, 0)$. Later, Novoderezhkin et al used the same general framework with an explicit treatment of the charge-transfer states[20] to model the Stark spectrum of photosystem II reaction center.

One major limitation of the approaches discussed so far is that none scale to time-resolved third-order spectroscopies. The perturbed eigenstate approach of Liptay cannot properly account for coupling between states that changes strength as a function of orientation, while the perturbative expansions treating the field in the interaction term would require an equivalent of a $\chi^{(5)}$ simulation that would yield very complicated analytic expressions and would be expensive to compute, especially in the case of multiple chromophores. It is also not obvious that truncating the static field perturbation is appropriate at second order when the effective field amplitude that is experimentally achievable is the same order of magnitude as the optical fields, but applied throughout the experiment as opposed to a short impulse.

For the 2DESS simulations performed in this thesis, a more direct approach in the spirit of Liptay is taken. The simulations performed on the basis of this approach constitutes the major contribution of this thesis. We assume that the DC field interaction acts to shift the eigenstates of the system, leading to the response functions having the form

$$R = \hat{Q}_\alpha \hat{Q}_\beta \hat{Q}_\gamma \hat{Q}_\mu \exp(-i\omega'_{eg}\tau_1 - i\omega'_{eg}\tau_3) \exp(\cdots) \tag{2.82}$$

where $\omega'_{eg} = \omega_{eg} - \Delta\omega_{eg}$ is the orientation-dependent shifted eigenstate frequency given by 2.81. The orientational average is then evaluated explicitly using a spherical mesh of appropriate order[*][21]. and the resulting third-order signals are interpreted as difference spectra

$$S^{(3)}(\omega_1, T, \omega_3)_{2\text{DESS}} = S^{(3)}(\omega_1, T, \omega_3, \boldsymbol{E}_{\text{DC}}) - S^{(3)}(\omega_1, T, \omega_3) \tag{2.83}$$

[*]The details of the computational method are discussed in the following chapter

This approach has the benefit of being conceptually identical to the way experimental signals are obtained and allows us to observe the effects of a large static field interacting with the difference permanent dipole and polarizability without treating it perturbatively. Effectively, the site energies of field-dependent terms are shifted as a function of orientation. In the case of independent chromophores, the approach reduces to the full Liptay theory to produce first- and second-derivative lineshapes. For strongly-coupled excitonic systems, the field instead acts to change the composition of the excitons, yielding more complicated spectra that cannot be simply interpreted. These effects are discussed in the following chapter, in which this novel approach is used to simulate 2D electronic Stark spectra of excitonically-coupled dimer system relevant for the study of charge-separation in photosynthetic systems.

*References*

1. P. N. Butcher and D. Cotter: The elements of nonlinear optics. Ed. by P. L. Knight and W. J. Firth. Cambridge, UK: Cambridge University Press, 1991.

2. S. Mukamel: Principles of Nonlinear Optical Spectroscopy. New York: Oxford University Press, 1995.

3. P. Hamm and M. Zanni: Concepts and Methods of 2D Infrared Spectroscopy. Cambridge, UK: Cambridge University Press, 2011.

4. D. J. Jackson: Classical Electrodynamics. 3rd. Hoboken, NJ: John Wiley & Sons, 1999.

5. M. Born and E. Wolf: Principles of Optics. Ed. by M. Farley-Born and E. Wolf. 7th (expan. Cambridge, UK: Cambridge University Press, 1999, pp. 1–936.

6. M. D. Levenson and S. S. Kano: Introduction to Nonlinear Laser Spectroscopy. San Diego, USA: Academic Press, 1988.

7. J. Sung and R. J. Silbey: Four wave mixing spectroscopy for a multilevel system. Journal of Chemical Physics **115**(20) (2001), 9266–9287. doi: 10.1063/1.1413979.

8. G. W. Ford et al.: Quantum Langevin equation. **37** (1988), 4419–4428.

9.  A. W. Albrecht et al.: Experimental distinction between phase shifts and time delays: Implications for femtosecond spectroscopy and coherent control of chemical reactions. Journal of Chemical Physics **111**(24) (1999), 5691. doi: 10.1063/1.480457.

10. S. M. G. Faeder and D. M. Jonas: Phase-resolved time-domain nonlinear optical signals. Phys. rev. A **62**(January) (2000), 33820. doi: 10.1103/PhysRevA.62.033820.

11. D. Abramavicius et al.: Manipulation of two-dimensional spectra of excitonically coupled molecules by narrow-bandwidth laser pulses. Chemical Physics **372**(1-3) (2010), 22–32. doi: 10.1016/j.chemphys.2010.04.015.

12. D. Abramavicius et al.: Coherent Multidimensional Optical Spectroscopy of Excitons in Molecular Aggregates; Quasiparticle Versus Supermolecule Perspectives. Chemical Reviews **109** (2009), 2350–2358.

13. D. L. Andrews and T. Thirunamachandran: On three-dimensional rotational averages. The Journal of Chemical Physics **67**(11) (1977), 5026. doi: 10.1063/1.434725.

14. A. Albrecht: Polarizations and assignments of transitions: The method of photoselection. Journal of Molecular Spectroscopy **6** (1961), 84–108. doi: 10.1016/0022-2852(61)90234-X.

15. J. Dostál et al.: Mapping the energy flow through the entire photosynthetic apparatus in situ. Submitted **8**(May) (2015), 1–6. doi: 10.1038/nchem.2525.

16. W. Liptay: Dipole Moments and Polarizabilities of Molecules in Excited Electronic States. Excited States. New York: Academic Press, 1974, 129–229.

17. W. Liptay: Electrochromism and Solvatochromism. Angewandte Chemie - International Edition **8**(3) (1969), 177–188.

18. S. G. Boxer: Stark Realities. Journal of Physical Chemistry B **113** (2009), 2972–2983.

19. O. J. G. Somsen et al.: Excitonic Interactions and Stark Spectroscopy of Light Harvesting Systems. The Journal of Physical Chemistry B **102**(44) (1998), 8893–8908. doi: 10.1021/jp981114o.

20. V. I. Novoderezhkin et al.: Mixing of exciton and charge-transfer states in Photosystem II reaction centers: modeling of Stark spectra with modified Redfield theory. Biophysical journal **93**(4) (2007), 1293–1311. doi: 10.1529/biophysj.106.096867.

21. I. H. Sloan and R. S. Womersley: Extremal Systems of Points and Numerical Integration on the Sphere. Advances in Computational Mathematics **21**(1/2) (2004), 107–125. doi:

10.1023/B:ACOM.0000016428.25905.da.

## Modeling of 2DESS Spectra

In this chapter, I calculate the spectral signatures of energy and charge-transfer in several model systems as they would show up in a 2DESS experiment using realistic parameters. By contrasting the calculated signatures, I discuss strategies for differentiating energy transfer from charge-transfer and compare the utility of the 2DESS experiment to the 2DES and Stark spectroscopy experiment. The chapter culminates in a discussion of a charge-transfer-active dimer system modeled after the "special-pair" of photosystem II rection center.

### 3.1   Theory

*System Hamiltonian*

As the model system we take a set of $N$ excitonically-coupled two-level systems of the Frenkel exciton form[1,2]

$$\hat{H}_0 = \sum_i \mathcal{E}_i \hat{B}_i^\dagger \hat{B}_i + \sum_{i \neq j} \mathbb{J}_{ij} \hat{B}_i^\dagger \hat{B}_j + \sum_{i \neq j} \frac{\mathbb{K}_{ij}}{2} \hat{B}_i^\dagger \hat{B}_j^\dagger \hat{B}_i \hat{B}_j + \hat{H}_{\text{bath}} + \hat{H}_{\text{SB}} + \hat{H}_{\text{DC}} \qquad (3.1)$$

where $\hat{B}_i$ ($\hat{B}_i^\dagger$) destroy (create) an excitation on the $i$-th molecule*. Here, the first term represents the site energy and $\mathbb{J}_{ij}$ is the coupling between excitations on the $i$-th and $j$-th site. The matrix $\mathbb{K}_{ij}$ represents the anharmonicity of the doubly-excited state consisting of an excitation residing

---

*This notation is called second-quantization form and is discussed in detail in literature on molecular crystals[3,4]. More information in the context of 2D spectroscopy may be found in Mukamel[2]

on $i$ and $j$. The bath terms $\widehat{H}_{\text{bath}}$ and $\widehat{H}_{\text{SB}}$ represent the harmonic oscillator bath discussed in Chapter 2[1,2].

The Stark Hamiltonian in this notation induces a shift in the site energy $\mathcal{E}$ parameterized by the orientation of the two-level system and the magnitude of the DC field $\boldsymbol{E}_{\text{DC}}$,

$$\widehat{H}_{\text{DC}} = \sum_i \left[ -\Delta\widehat{\boldsymbol{\mu}} \cdot \boldsymbol{E}_{\text{DC}} - \frac{1}{2}\boldsymbol{E}_{\text{DC}} \cdot \Delta\widehat{\boldsymbol{\alpha}} \cdot \boldsymbol{E}_{\text{DC}} \right] \widehat{B}_i^\dagger \widehat{B}_i \tag{3.2}$$

The distinction between the local field and the externally-applied field has been dropped for the purposes of this modeling.

In the interaction Hamiltonian, the contribution of the nuclear charge was ignored and the dipole approximation was used. Then the field-matter coupling takes the form

$$\widehat{H}_{\text{I}}(t) = \sum_i \left[ \widehat{\boldsymbol{\mu}}_i \widehat{B}_i^\dagger + \widehat{\boldsymbol{\mu}}_i^\dagger \widehat{B}_i \right] \cdot \boldsymbol{E}(t) \tag{3.3}$$

where $\widehat{\boldsymbol{\mu}}_i$ is the transition moment dipole for the $i$-th excitation.

*Rotational and Disorder Averaging*

To obtain linear and 2D spectra for an isotropically oriented sample, a rotational average was performed over the orientation of the lab as observed by the molecule. To generate a set of rotation matrices uniformly-distributed over the three-dimensional surface $S^3$, the following strategy was taken. First, a set of uniformly-distrbuted points on the surface of a sphere was obtained from a spherical-design mesh[5] of order $m$. The rotation of the laboratory frame $\hat{z} \mapsto \hat{z}'$ axis to each point on the mesh was encoded as a quaternion[6]. A set of $n$ rotations about $\hat{z}'$ was then generated over the range $[0, 2\pi)$ to rotationally average over the orientation of the $\hat{x}'$ and $\hat{y}'$ axes. This parameterization is particularly easy in the quaternion formalism[6]. The resulting quaternion encoding the coordinate transformation was then converted to a rotation matrix that was applied to the polarization vector of the optical fields $\boldsymbol{e}$ and the orientation of the Stark field $\boldsymbol{E}_{\text{DC}}$. Ap-

proaches for generating a random uniform rotation matrix were also tried[7], but it was found that the convergence of the two-dimensional spectra in this case was extremely slow.

Optionally, static disorder was added to the simulation by sampling the set of site energies $\mathcal{E}_i$ from a joint-Gaussian distribution parameterized by mean transition energies $\mathcal{E}_{0,i}$ and FWHM variances $\sigma_i$. The covariance was set to zero. For each sample of energies, a rotational average was performed as above. The resulting spectra were averaged together to obtain the final spectrum.

The Stark and 2DESS spectra were generated by repeating the procedure with the static field perturbation on and off and taking the difference.

*Model Parameters*

The parameters for the modeling were chosen to approximate the $Q_y$ bands of the $P_{D1}$ and $P_{D2}$ chlorophylls (Chls) of the photosystem II reaction center and a charge-transfer (CT) state between them. The relative orientations of the transition dipole moments of the two Chls were extracted from a recent high-resolution crystal structure of PSII ([8], PDB: 3WU2) by calculating the normalized vector connecting the $N_B$ and $N_D$ nitrogens in the Chl porphyrin ring[9] (see Figure 3.1). The magnitude of the transition moments $\|\hat{\boldsymbol{\mu}}_i\|$ was assumed to be 4.0 Debye[10]*. It was further assumed that the permanent dipole moment difference vector $\Delta\hat{\boldsymbol{\mu}}$ of Chl lies in the same direction as the transition moment[11] and has magnitude 1.41 D[12]. The CT state was modeled as a two-level system with no transition dipole moment and a large $\|\Delta\hat{\boldsymbol{\mu}}\| = 38$ D. The relative orientation was chosen as the vector connecting the Mg atoms of the Chls, with the magnitude estimated by Coulombic interaction[12]. This was done to model the $P_{D1}^- O_{D2}^+$ CT state that is proposed to lie there. When included, the change in polarizability $\Delta\hat{\boldsymbol{\alpha}}$ was fixed at a large value such that the Stark shift is the same order of magnitude as the permanent dipole moment contribution and to be isotropic, $\mathrm{Tr}[\Delta\hat{\boldsymbol{\alpha}}]/3 = 100\,\text{Å}^3$. This was done to more easily compare the effects of $\Delta\hat{\boldsymbol{\alpha}}$

---

*1 Debye $\approx 3.34 \times 10^{-30}$ C m; 1 Å$^3 \approx 1.113 \times 10^{-40}$ C m$^2$ V$^{-1}$
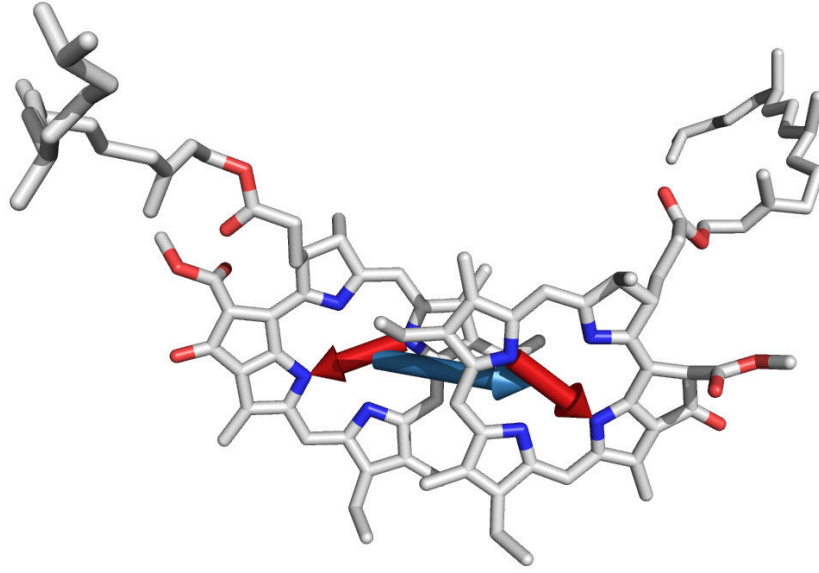
**Figure 3.1** Relative orientation of transition and permanent dipole moments. $P_{D1}$ and $P_{D2}$ were extracted from crystal structure (PDB: 3WU2), with difference transition and permanent dipole moments of the $Q_y$ transition represented as arrows. The Chl transition dipole moments are shown in red, the CT state permanent dipole moment is shown in blue.

and $\Delta\hat{\mu}$.

Coupling between the Chls and CT state and the site-energies were obtained from previously published models[10–12]. In particular, the Chl-Chl coupling was assumed to be 150 cm$^{-1}$, and the Chl-CT coupling was 45 cm$^{-1}$. The site energies were 15,260 cm$^{-1}$, 15,190 cm$^{-1}$ and 15,180 cm$^{-1}$ for $P_{D1}$, $P_{D2}$, and the CT state, respectively.

The system bath spectral density was simulated in two ways. The first model $J_I(\omega)$ included an overdamped Brownian oscillator of the form

$$J_I(\omega) = 2\lambda_0 \frac{\omega\gamma_0}{\omega^2 + \gamma_0^2} \tag{3.4}$$

with the parameters $\lambda_0 = 35$ cm$^{-1}$ and $\gamma_0 = 40$ cm$^{-1}$[12]. The second model additionally included high-frequency underdamped modes representing vibrational structure of the excited state

58

extracted from fluorescence-line-narrowing experiments[13]

$$J_{II}(\omega) = J_I(\omega) + \sum_j 2\lambda_j \omega_j^2 \frac{\omega \gamma_j}{\left(\omega_j^2 - \omega^2\right)^2 + \omega^2 \gamma_j^2} \tag{3.5}$$

For each mode $\gamma_j = 3\,\mathrm{cm^{-1}}$. The modes with frequency above $1{,}000\,\mathrm{cm^{-1}}$ were not included to prevent aliasing effects upon 2DESS calculation. In both cases, the bath temperature was set to 77 K, corresponding to an inverse temperature of $\approx 53.5\,\mathrm{cm^{-1}}$. The coupling to the spectral density for each Chl was set to 1.0, while the CT state coupling was 1.5[13]. This represents the larger relaxation rate of the CT state as compared to the sites. When using the simplified spectral density $J_I$ and $J_{II}$, the site-energies were shifted by $-\lambda_0 = 505.3\,\mathrm{cm^{-1}}$ and $278.2\,\mathrm{cm^{-1}}$ to keep the simulation window similar to that in simulations of Novoderezhkin et al. The spectral densities $J_I$, $J_{II}$, and the original spectral density of[12] (labeled $J_{III}$) are shown in Figure 3.2.

The optical electric fields were assumed to be identically polarized along $\hat{x}$ and to have a field strength of $\left\|\boldsymbol{E}_{\text{optical}}\right\| = 1.1\,\mathrm{MV/cm}$. The Stark field was oriented along $\hat{y}$ with magnitude $\left\|\boldsymbol{E}_{\text{DC}}\right\| = 1\,\mathrm{MV/cm}$, corresponding to a shift of $16.8\,\mathrm{cm^{-1}/D}$ and $0.056\,\mathrm{cm^{-1}/\mathring{A}^3}$. These values were chosen based on typical experimental values used in our experiments described in Chapter 6.

## 3.2    Results

The effect of the Stark field on two-dimensional electronic spectra was simulated by modeling progressively larger systems with the site parameters as described in the previous section.

For convenience, the plot format is the same for all cases. The left side consists of the calculated 2D spectrum at population time $T = 0$ on the lower left and the calculated linear absorption spectrum on the upper left. A projection of the 2D onto the $\omega_\tau$ axis is also plotted in the upper left, showing a very close match to the linear absorption spectrum. The 2D spectrum amplitude is normalized to $\pm 1$ and plotted with line contours increasing exponentially by a factor of 2. The right side is the calculated 2DESS and Stark spectra plotted in the same format, with the projec-
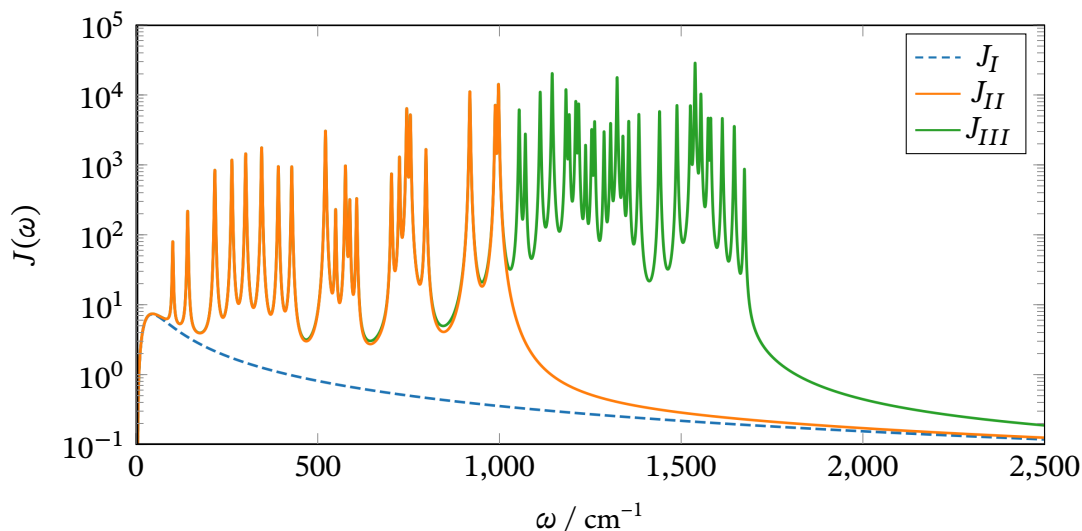
**Figure 3.2** Spectral densities used for 2DESS modeling. The low-frequency modes are represented by an overdamped Brownian oscillator $J_I$. High-frequency modes were modeled as underdamped modes with $\gamma = 3\,\text{cm}^{-1}$ and other parameters obtained from[12] ($J_{III}$). For numerical convenience, the modes with central frequency above $1{,}000\,\text{cm}^{-1}$ were removed ($J_{II}$).

tion on $\omega_\tau$ plotted over the Stark spectrum. The number in the upper-right of the 2DESS is the relative scaling factor between 2D and 2DESS spectra. Bars are included in the linear absorption and Stark spectra to indicate the positions of electronic eigenstates, color-coded by their eigenvalues from lowest to highest as blue, red, and green. The dashed bars represent initial positions before bath reorganization and imaginary dephasing is applied.

*Projection of 2D onto the Excitation Axis*

In the simulations of this model system, it was found that the normalized projection of the 2D spectrum at $T = 0$ onto the excitation axis accurately tracks the linear absorption spectrum (see Figure 3.3). This approach reproduces the correct linewidth much better than the commonly used approach of taking the square-root of the diagonal slice and is useful even in the 2DESS and Stark spectra comparison. Although 2D and linear absorption are intrinsically different experiments, the projection is a useful way to understand the additional information that the 2DESS experiment

is able to resolve as compared to the Stark experiment. In particular, it suggests the reasons that the Liptay formalism breaks down in the case of strong couplings and the presence of CT states.

The justification for the 2D absorptive spectrum projection onto $\omega_\tau$ resulting in a scaled version of the linear absorption spectrum can be explained pictorially via Figure 3.4. In the coupled-dimer model, the dipole moments for the ground-state to excited-state transitions and the excited-state to doubly-excited state transitions are identical. Upon integration along the detection axis, the ESA and GSB signals cancel such that the signal that remains is the SE signal. For the special case of all-parallel 2D and identical dipoles, this can be written as the linear absorption multiplied by a prefactor that is canceled upon normalization of both the projected 2D and the linear absorption. This is equivalent to stating that all information about the dynamics is "traced out" by the summation along $\omega_t$ and we retain only the initial absorption of the pump along $\omega_\tau$. This approach generalizes to non-parallel orientations as well, provided the experiment is performed with optical polarizations at a generalized "magic-angle," such that the anisotropy of the 2D spectrum is removed and the cancellation between ESA and GSB is maintained[14]. More mathematical details on this procedure for the purpose of fitting the kinetics of 2D spectra is discussed by Dostál et al.[14].

### $J_I$ Spectral Density

The simplest case investigated was the effect of the static field on the spectrum of the $P_{D1}$ monomer. As can be seen from Figure 3.5 and Figure 3.6, the lineshapes of the Stark and 2DESS spectra follow the Liptay model[15]. The Stark and 2DESS spectrum appears with a first-derivative lineshape when only the $\Delta\widehat{\alpha}$ contribution* is modeled (Figure 3.5), and a second-derivative shape when only the $\Delta\widehat{\mu}$ is taken into account (Figure 3.6). Note that because of peak asymmetry in the absorption and 2D spectrum, the second derivative shape exhibits a similar peak asymmetry. In practice, fit-

---

*this contribution is second-order in the applied field $E_{DC}$
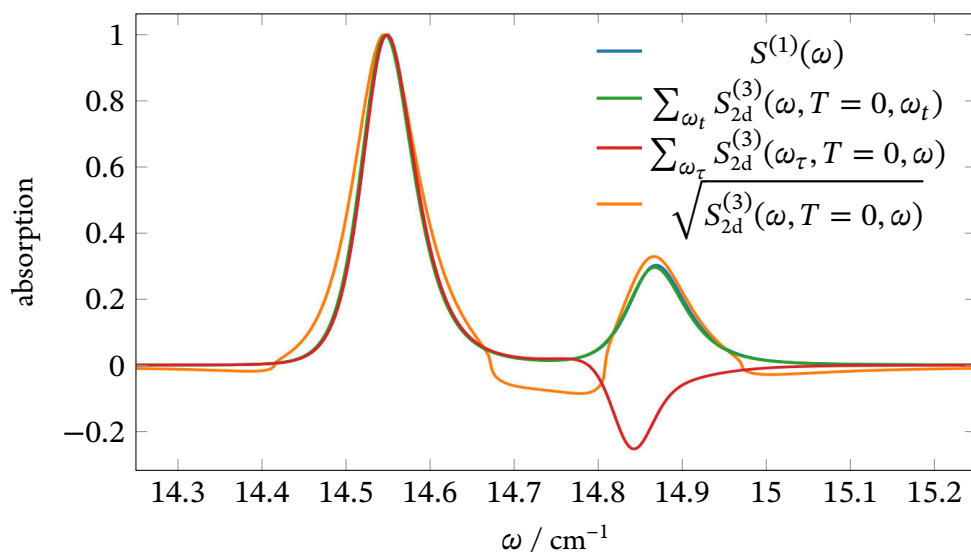
**Figure 3.3** Comparison of different projections of the 2D real-absorptive spectrum of the $P_{D1}P_{D2}$ dimer and the calculated linear absorption. The projection onto the excitation axis $\omega_\tau$ matches the linear absorption spectrum $S^{(1)}$ nearly perfectly. The diagonal slice shown in orange tends to broaden the linewidth and has discontinuities due to negative ESA features that appear on the diagonal.
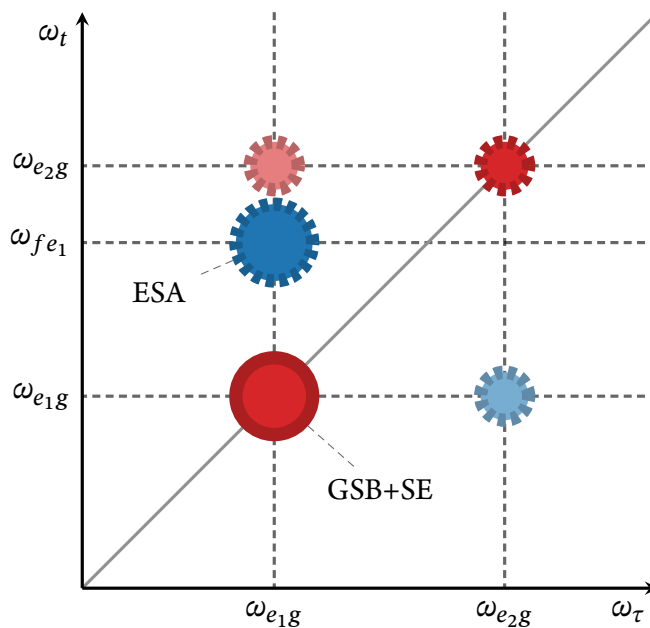


**Figure 3.4** Illustration of the 2D real-absorptive spectrum of a J-type dimer, showing the positions of ESA, SE, and GSB signals.

ting of linear absorption spectra and Stark spectra is performed with a sum-of-Gaussians model for which this peak asymmetry may lead to an incorrect conclusion that a significant polarizability difference $\Delta\widehat{\alpha}$ is present. Fitting the measured absorption spectrum is "safer" in this regard, though it forces the parameters of the fitting to be identical over the measured absorption bandwidth. A partial solution is to fit the absorption spectrum to a small number of asymmetric lineshapes, for example as discussed in[16].

In the simulations, a very large value of difference polarizability $\Delta\widehat{\alpha} = 100\,\text{Å}^3$ was used to make the effect of this term in the spectrum approximately the same amplitude as that from the permanent dipole moment change $\Delta\widehat{\mu}$. It is important to point out that the estimated $\Delta\widehat{\alpha}$ values for Chl in ethanol are estimated to be smaller by over an order of magnitude[17]. This value was chosen to demonstrate that the value of the polarizability would need to be unphysically large to get a similar magnitude of Stark signal.

In simulations of the dimer $P_{D1}P_{D2}$, the spectra of the $\Delta\widehat{\mu}$ case follow a similar behavior as the monomer with regards to the lineshape (see Figure 3.7). However, now we observe that the amplitude of the second-derivative contribution of the upper exciton at 14,800 cm$^{-1}$ is enhanced as compared to the monomer case in the 2DESS spectrum. This is a consequence of two facts. First, the cross-peaks in 2D spectra are proportional to $\mu_1^2\mu_2^2$ while diagonal peaks have the same dipole moment $\mu_2^2\mu_2^2$. When the dipole magnitude of the lower exciton is much larger than that of the upper exciton, the cross-peak amplitude is larger than the diagonal peak. Second, the Stark spectrum is a projection of the $T = 0$ signal of 2DESS projected onto the $\omega_\tau$ axis. This enhancement is canceled somewhat, due to the opposite sign of ESA at 14,800 cm$^{-1}$ and SE+GSB at 14,550 cm$^{-1}$, resulting in some cancellation of the Stark signal there. The 2DESS signal is about twice as large relative to the 2D signal as for the monomer case.

Upon addition of a CT state (Figure 3.8), the lineshape of the Stark spectrum changes significantly. In the $\Delta\widehat{\mu}$ case, the upper- and lower-excitons take first-derivative lineshapes, and a large
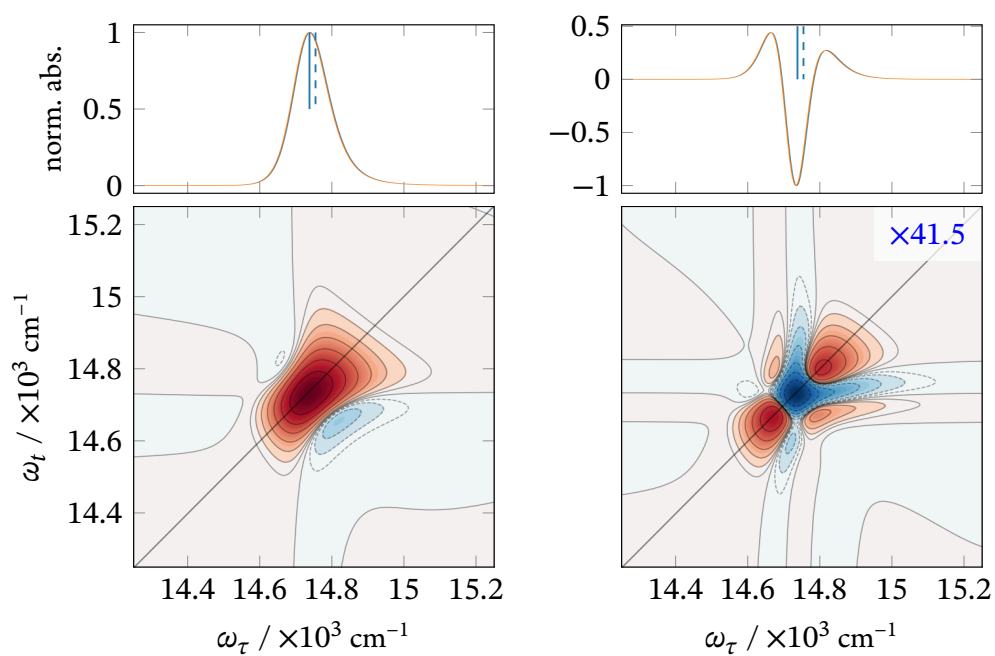
**Figure 3.5** 2D and 2DESS spectra of $P_{D1}$ calculated with $J_I$ spectral density and $\Delta\hat{\mu}$ contribution only. The dashed blue bars show the initial position of $P_{D1}$ before bath reorganization is applied $(14{,}755\ \mathrm{cm}^{-1})$. The final position is shown as a solid line $(14{,}738\ \mathrm{cm}^{-1})$.
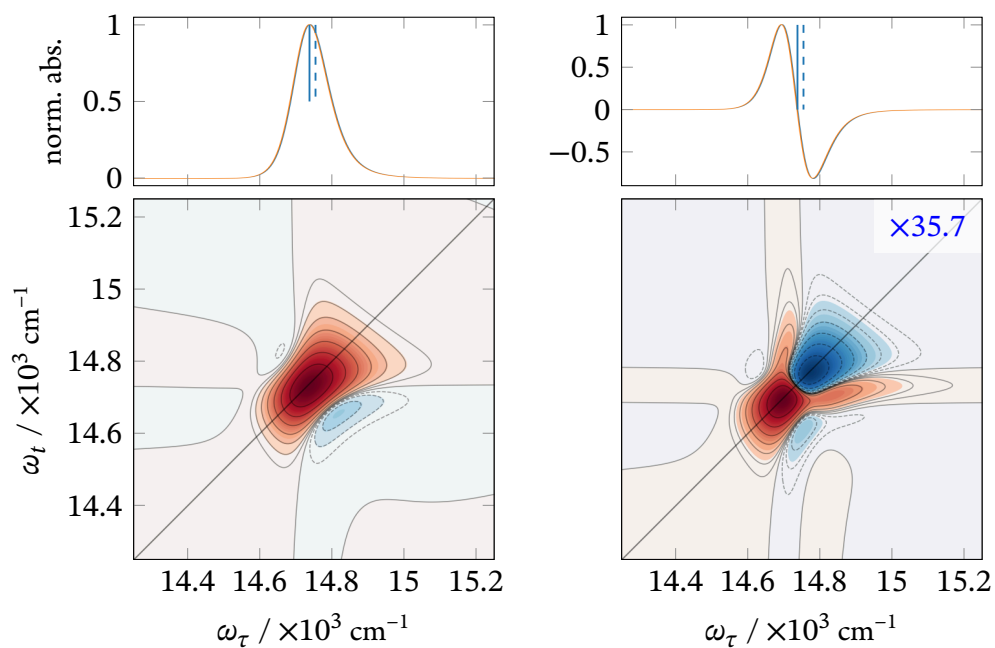


**Figure 3.6** 2D and 2DESS spectra of $P_{D1}$ calculated with $J_I$ spectral density and $\Delta\hat{\alpha}$ contribution only. Prior to bath reorganization, $P_{D1}$ is located at $14{,}755\ \mathrm{cm}^{-1}$ (dashed blue), finally shifting to $14{,}738\ \mathrm{cm}^{-1}$ (solid blue).
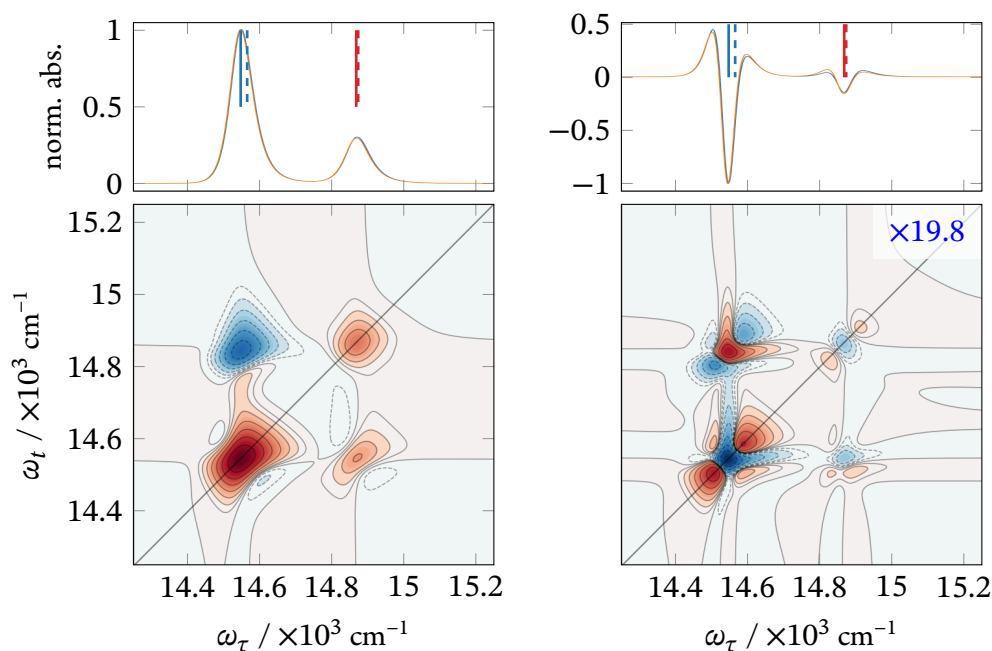
**Figure 3.7** 2D and 2DESS spectra of $P_{D1}$ $P_{D2}$ dimer calculated with $J_I$ spectral density and $\Delta\hat{\mu}$ contribution only. Initial positions of eigenstates are shown in dashed lines. The lower exciton corresponds to 61:39% $P_{D2}$:$P_{D1}$, shifting from 14,566 cm$^{-1}$(dashed) to 14,548 cm$^{-1}$. The upper exciton (red) shows the opposite ratio and shifts from 14,874 cm$^{-1}$ to 14,868 cm$^{-1}$.

amplitude cross-peak appears between them. This cross-peak is responsible for the majority of the 2DESS signal amplitude. Interestingly, the Stark spectrum has the largest amplitude at the position near the upper-exciton. It is apparent from the 2DESS spectrum that the CT state is localized near the lower-exciton. Upon projection onto the excitation axis, most of the signal is canceled out, which leads to a misleading Stark spectrum. The 2DESS spectrum does not have this defect. Note also that that the signal amplitude is increased by a factor of four from the dimer case and the first-derivative shapes along the diagonal are mirrored in opposite directions.

To explain the difference between the Stark and 2DESS signal amplitude, it is convenient to look at the delocalization of the CT state as a function of orientation. By squaring the unitary transformation matrix from the site-basis to the eigen-energy basis, one can obtain the fractional delocalization of the CT basis onto the eigenstates. This can be represented as a polar plot show-
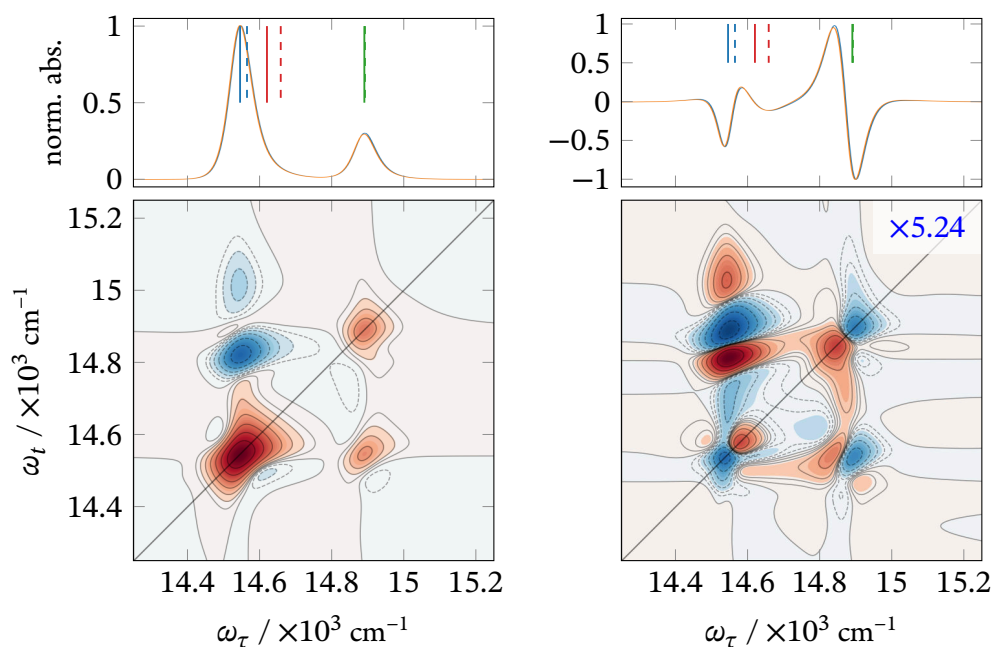
**Figure 3.8** 2D and 2DESS spectra of $P_{D1}$ $P_{D2}$ dimer and CT state calculated with $J_I$ spectral density and $\Delta\widehat{\mu}$ contribution only. The lower exciton (blue) consists of primarily $P_{D2}$ and $P_{D1}$ in the proportion 62:37:0.5% of $P_{D2}$:$P_{D1}$:CT, shifting from 14,565 cm$^{-1}$ to 14,546 cm$^{-1}$. The upper exciton (green) consists of 36:56:8% $P_{D2}$:$P_{D1}$:CT. The imaginary dephasing and bath reorganization nearly cancel, barely shifting the state from 14,892 cm$^{-1}$ to 14,891 cm$^{-1}$. The CT state is primarily localized on the second eigenstate (red), 7:1.3:91% in the same order. This is reflected in the comparably large shift of this eigenstate from 14,659 cm$^{-1}$ to 14,620 cm$^{-1}$.

ing percentage of CT character in each eigenstate, with the energy of the eigenstate in cm$^{-1}$ along the radius. The plot for the dimer+CT $\Delta\widehat{\mu}$ case is shown in Figure 3.9. The first, second, and third eigenstates are represented as blue, orange and green circles, respectively. The CT state has no transition dipole moment and thus does not contribute significantly to the Stark spectrum when it is localized. Therefore, there should not be a significant Stark signal in the regions near 14,500 cm$^{-1}$, 14,700 cm$^{-1}$ and 15,000 cm$^{-1}$. The largest signal is obtained when the CT state is close to 50% delocalized which occurs at 14,550 cm$^{-1}$, 14,850 cm$^{-1}$ and 14,900 cm$^{-1}$. This is reflected in the Stark spectrum, which shows large amplitude at those positions. Because of the cancellation of the cross-peak at 14,550 cm$^{-1}$, the Stark signal amplitude does not reflect the large
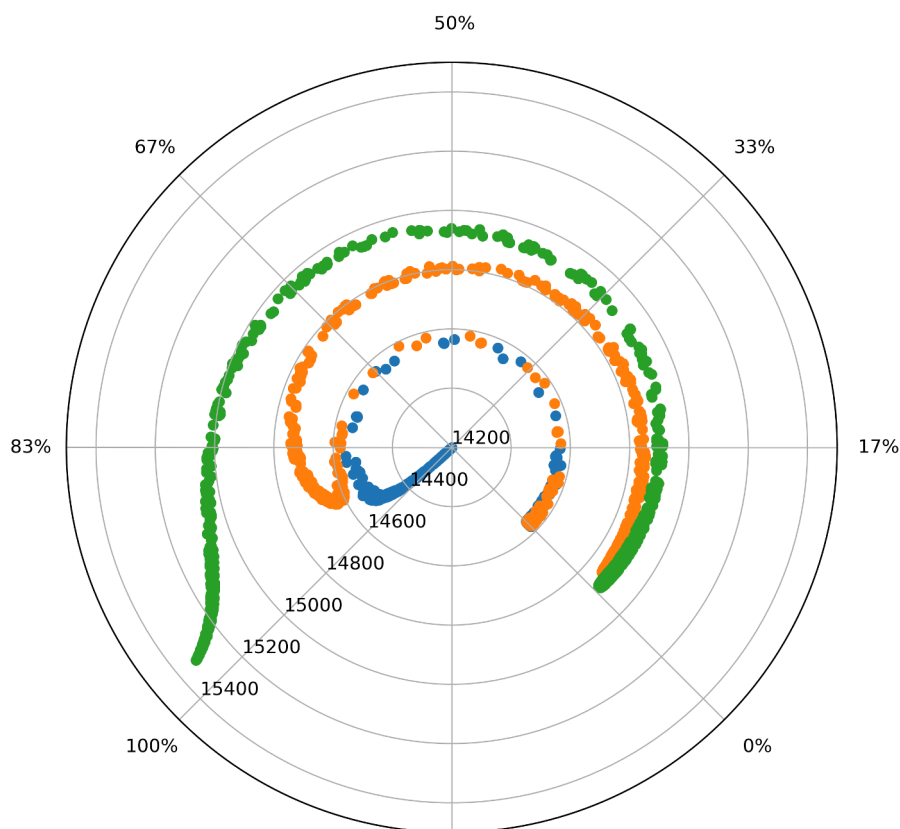
**Figure 3.9** Localization of the CT state on three eigenstates for the $P_{D1}P_{D2}$+CT system using the $J_I$ spectral density. Three eigenstates are shown in shown in blue, orange, and green, as a function of orientation. The energy of the eigenstates is shown on the radial axis in cm$^{-1}$. The percentage of CT state character is on the perimeter.

changes in cross-peak amplitude observed in the 2DESS spectrum, reflecting a change in the coupling between the lower- and upper-excitons as a function of orientation. This interpretation suggests that the Stark spectrum does not contain enough information to localize the position of CT states in strongly-coupled systems, but that the cross-peaks in the 2DESS spectrum may show a clearer picture.

The figures for the $\Delta\hat{\alpha}$ case for all subsequent simulations may be found in Appendix D. The difference polarizability contribution in the isotropic limit simply results in a shift of the energy of the eigenstates, resulting in a first-derivative lineshape in Stark spectra. For the case that $\Delta\hat{\alpha}$ has

the same sign for all states, the peak asymmetry will be oriented in the same way, generally with the positive feature on the low-energy side reflecting that upon applied DC field, the molecule is more readily polarized in the same direction. The polarizability is expected to be quite smaller for realistic systems, on the order of $10\,\text{Å}^3$[18].

*$J_{II}$ Spectral Density*

To obtain a more realistic simulation of the $P_{D1}P_{D2}$ dimer, the $J_{II}$ spectral density was used for Stark simulation. In addition to providing a model for the vibrational structure of the pigments in the reaction center, this spectral density causes a significant broadening of the lineshapes corresponding to stronger system-bath coupling. This is reflected in the modeling, in which the lineshapes are significantly broader than for the $J_I$ spectral density. For this density, the reorganization energy shift is $261.8\,\text{cm}^{-1}$. All site energies were shifted by $278.2\,\text{cm}^{-1}$ to match the modeling of Novoderezhkin et al.

The monomer $P_{D1}$ spectra (Figure 3.10, Figure D.2) have the same behavior as observed in the previous section. As before, the $\Delta\widehat{\boldsymbol{\mu}}$ 2DESS spectrum exhibits a second-derivative lineshape that is asymmetric and larger on the red side. Because of the Born-Oppenheimer approximation, the vibrational structure is simply overlaid on top of the electronic structure, shifting in the same way as the electronic transition. This is reflected in the positions of the most-negative features in the vibronic progression of Figure 3.10. Compared to the $J_I$ calculations, ESA features appear on the diagonal, reflecting transitions from the $i \rightarrow j$ vibrational transitions where $i \neq j$. These features do not agree with monomer 2DES data obtained in $\text{Chl}-\text{a}$[19,20], calling into question the appropriateness of using the $J_{II}$ and $J_{III}$ spectral densities in simulations[21]. The relative amplitude of the 2DESS signal is slightly larger than before.

The dimer $P_{D1}P_{D2}$ spectra exhibit a more complicated structure due to the spectral density. Because of larger system-bath coupling, the ESA feature is shifted by an additional $261.8\,\text{cm}^{-1}$ cor-
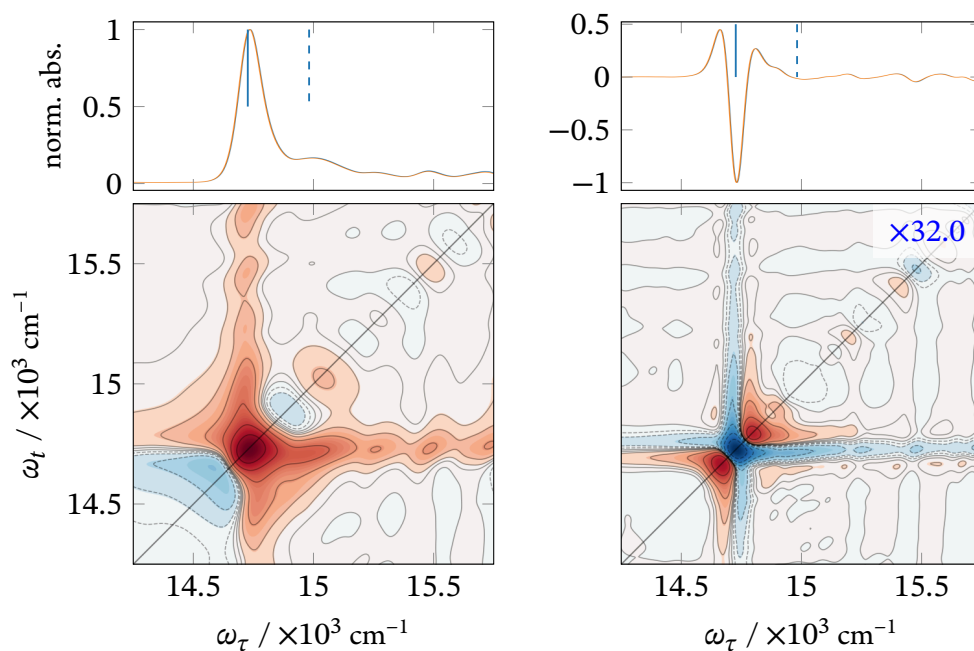
**Figure 3.10** 2D and 2DESS spectra of $P_{D1}$ calculated with $J_{II}$ spectral density and $\Delta\widehat{\mu}$ contribution only. The $P_{D1}$ (blue) shifts from 14,982 cm$^{-1}$ to 14,727 cm$^{-1}$, reflecting the much larger bath-reorganization energy. The spectral density generates ESA signatures near the diagonal that are not observed in experiment.

responding to the interaction of the bath with the doubly-excited states. The features from each exciton shift diagonally in the 2DESS spectrum, while the cross-coupling features (off-diagonal ESA and GSB+SE) shift vertically. The strongest features of the 2D spectrum correspond to opposite-signed features on the 2DESS spectrum, allowing one to differentiate electronic cross-peaks from vibrational overtones of diagonal peaks. Because of larger dephasing of the upper-exciton and the lack of an ESA feature, it dominates the Stark spectrum. Notably, the lineshapes of the Stark spectrum resemble those of the first-derivative of the 2D spectrum.

With the addition of a CT state, the 2DESS spectrum changes significantly. In the reference 2D, the CT state is located on the red side of the lower-exciton, near 14,555 cm$^{-1}$ and is strongly localized. Because of this, there is no significant feature in the spectrum that can be associated with the CT state. The other major features are the lower and upper excitons, consisting of roughly 55%
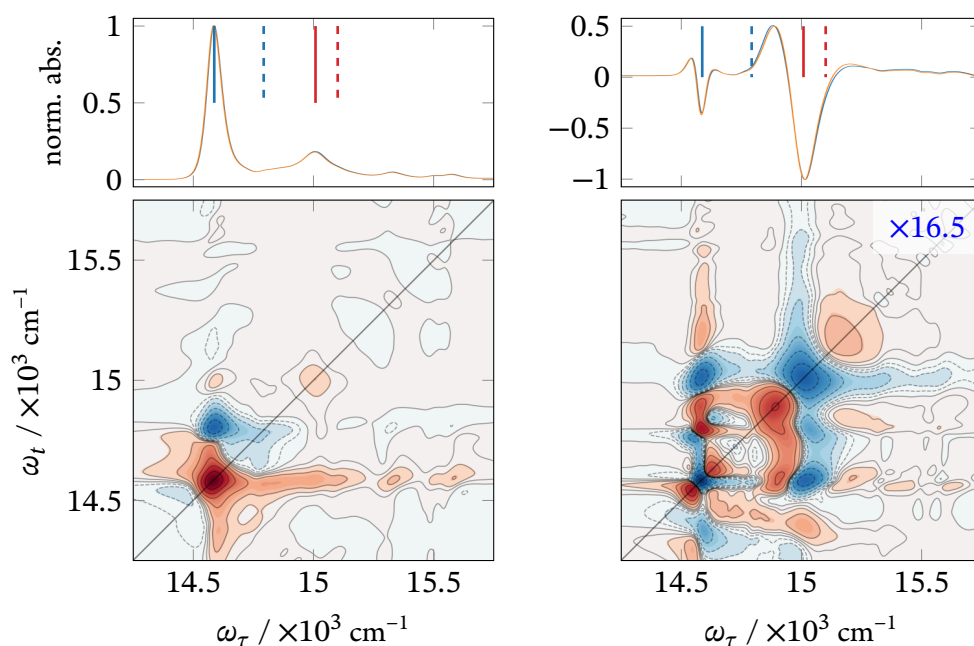
**Figure 3.11** 2D and 2DESS spectra of $P_{D1}P_{D2}$ calculated with $J_{II}$ spectral density and $\Delta\hat{\mu}$ contribution only. As in the $J_I$ simulation, $P_{D1}$ and $P_{D2}$ are delocalized on the upper (red) and lower (blue) excitons in the ratio of 39:61, with the upper exciton consisting mostly of $P_{D1}$. Notably, the lower exciton is shifted more (from 14,793 cm$^{-1}$ to 14,587 cm$^{-1}$) than the upper exciton due to imaginary dephasing terms. The upper exciton shifts from 15,101 cm$^{-1}$ to 15,008 cm$^{-1}$.

$P_{D1}$, 36% $P_{D2}$ for the upper excition, and 63% $P_{D1}$, 37% $P_{D2}$ for the lower exciton. Upon applying the static field, the CT state becomes delocalized on the upper exciton, shifting the position of the upper peak in the 2DESS spectrum to lower energy because of the stronger system-bath coupling. The low-energy features in Figure 3.12 can be explained as a simple shift down in energy, analogous to the monomer-$\Delta\hat{\mu}$ case. The negative diagonal feature at 15,450 cm$^{-1}$ and the corresponding negative cross-peaks in the 2DESS spectrum reflect the shift of the upper-exciton. The vibrational structure of the shifted lower-exciton is canceled by the negative cross-peak at (15,450 cm$^{-1}$, 14,550 cm$^{-1}$) and the upper-exciton is shifted to a lower energy at 14,800 cm$^{-1}$. Interestingly, the pattern of the low energy peak in the 2DESS is inverted from that of Figure 3.8. This may be due to an interference effect of the CT state and the lower-exciton, which shifts the
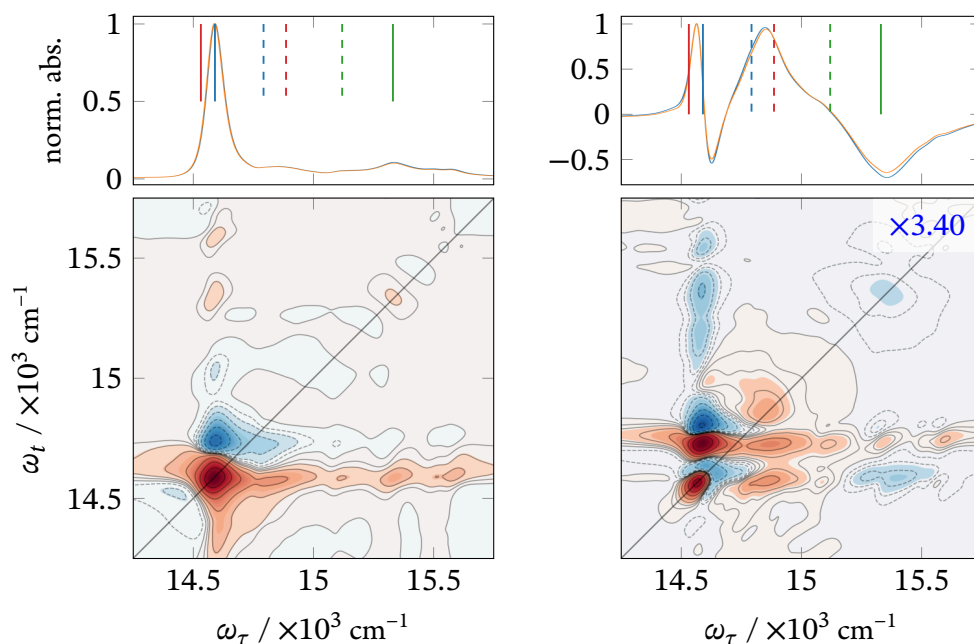
**Figure 3.12** 2D and 2DESS spectra of $P_{D1}P_{D2}$+CT calculated with $J_{II}$ spectral density and $\Delta\hat{\mu}$ contribution only. The initial configuration of the excitons is identical to the $J_I$ case discussed above. A significant departure from the previous case is due to magnitude of the reorganization shift of the localized CT state (red). It migrates from 14,885 cm$^{-1}$ to 14,531 cm$^{-1}$. The lower and upper excitons are located at 14,590 cm$^{-1}$ and 15,331 cm$^{-1}$. The upper exciton is shifted primarily due to imaginary dephasing terms.

characteristic second-derivative shape seen in Figure 3.10 to slightly lower energy as the lower-exciton takes on more CT character and therefore has larger system-bath coupling.

### 3.3 Discussion and Outlook

Stark spectroscopy has previously proven useful for the study of charge-separation reactions in photosynthetic reaction centers[22], as well as for the measurement of the direction and magnitude of local electric fields[23,24]. Here we have seen that it works quite well for the case of weakly-coupled excitonic systems, especially if the intrinsic peak asymmetry is taken into account. In this case, the Liptay formalism is applicable, and has formed the basis of analysis for these systems.

In the strongly-coupled dimer system considered here, however, it is evident that the simple interpretation of peaks as first- and second-derivative lineshapes is insufficient to localize the states of interest. Further, it appears that the asymmetry of the lineshape is strongly dependent on the strength of the system-bath coupling, allowing the lineshape to interpolate between the second- and first-derivative shape. This is particularly evident in the dimer with CT state case, for which the CT state migrates far away from its initial location upon application of the field and dominates the Stark signal contribution.

Based on a comparison of the results of preliminary 2DESS experiments on photosystem II reaction center (see Chapter 6) to this model, it appears that the modeled permanent dipole moment difference $\Delta\widehat{\mu}$ of the charge-transfer state is overestimated. There the applied field is nearly twice as large, yet such significantly shifted peaks have not been observed. This is not surprising, because this magnitude was assigned based on a Coulombic coupling model that was then fit to Stark and 2D spectra. Including the model discussed in this chapter in the form of the Stark calculation into the fitting procedure can narrow the parameter space of the fitting procedure and allow a quantitative comparison of the 2DESS spectrum with experiment. Because of the numerical averaging step involved in the 2DESS computation, at this time the full 2DESS simulation is too expensive to include in the fitting procedure directly. Future work includes performing the rotational averaging of the 2DESS model analytically using the phased-rotational averaging formalism of Andrews and Harlow[25].

For simple systems, the 2DESS experiment allows one to differentiate the $\Delta\widehat{\alpha}$ case from the $\Delta\widehat{\mu}$ case without resorting to fitting lineshapes. Because there is no projection onto the excitation axis $\omega_\tau$, the largest signals are not canceled even in the strongly-coupled dimer system. The location of the negative features on the diagonal and their corresponding cross-peaks allows one to localize the original position of the excitons. We expect this technique will be very useful for the study of organic photovoltaics, for which the coupling is not as strong as that in photosynthetic

reaction centers. Some experiments in this direction have already been performed on an organic polymer in solution, and are discussed in Chapter 5.

While the 2DESS signal for strongly-coupled systems with CT character is complicated, the experiment provides insight into the interference effects that dominate the Stark spectrum of these systems. The modeling suggests that the 2DESS experiment is particularly sensitive to the CT state, and may provide quantitative measurements of magnitude and position of this state. Though only the all-parallel optical polarization experiment was modeled here, performing this experiment with different optical polarization schemes and relative angle between the optical propagation vector and the Stark field may allow one to extract the relative orientation of the CT state dipole compared to the transitions of the excitons.

In addition to providing information about the position of the CT state at a fixed time, a two-dimensional electronic Stark experiment can be performed at different population times $T$, probing the formation and coupling of CT states to excitonic states during the course of a charge-transfer reaction. As demonstrated by the experiments of Chapter 6, the 2DESS spectra encodes information on the kinetics of charge-separation, allowing the study of charge-transfer reactions in complicated, spectrally-congested systems. Extracting quantitative information from these spectra remains a challenge, and further modeling is required to assign meaning to the relative magnitude of the features observed.

*References*

1. D. Abramavicius et al.: Coherent Multidimensional Optical Spectroscopy of Excitons in Molecular Aggregates; Quasiparticle Versus Supermolecule Perspectives. Chemical Reviews **109** (2009), 2350–2358.

2. S. Mukamel: Principles of Nonlinear Optical Spectroscopy. New York: Oxford University Press, 1995.

3. A. S. Davydov: Theory of Molecular Excitons. New York: Plenum Press, 1971.

4.  V. M. Agranovich and M. D. Galanin: Electronic Excitation Energy Transfer in Condensed Matter. Ed. by V. M. Agranovich and A. A. Maradunin. New York: Elsevier Science Publishing Company, 1982.

5.  I. H. Sloan and R. S. Womersley: Extremal Systems of Points and Numerical Integration on the Sphere. Advances in Computational Mathematics **21**(1/2) (2004), 107–125. doi: 10.1023/B:ACOM.0000016428.25905.da.

6.  K. Shoemake: Animating rotation with quaternion curves. ACM SIGGRAPH Computer Graphics **19**(3) (1985), 245–254. doi: 10.1145/325165.325242.

7.  F. Mezzadri: How to generate random matrices from the classical compact groups. Notices Am. Math. Soc. **54**(5) (2006), 592–604. arXiv: 0609050 [math-ph].

8.  Y. Umena et al.: Crystal structure of oxygen-evolving photosystem II at a resolution of 1.9 Å.. Nature **473**(7345) (2011), 55–60. doi: 10.1038/nature09913.

9.  M. E. Madjet et al.: Intermolecular coulomb couplings from ab initio electrostatic potentials: Application to optical transitions of strongly coupled pigments in photosynthetic antennae and reaction centers. Journal of Physical Chemistry B **110**(34) (2006), 17268–17281. doi: 10.1021/jp0615398. arXiv: arXiv:1401.4290v2.

10. G. Raszewski et al.: Theory of Optical Spectra of Photosystem II Reaction Centers: Location of the Triplet State and the Identity of the Primary Electron Donor. Biophysical Journal **88**(2) (2005), 986–998. doi: 10.1529/biophysj.104.050294.

11. V. I. Novoderezhkin et al.: Mixing of exciton and charge-transfer states in Photosystem II reaction centers: modeling of Stark spectra with modified Redfield theory. Biophysical journal **93**(4) (2007), 1293–1311. doi: 10.1529/biophysj.106.096867.

12. V. I. Novoderezhkin et al.: Multiple charge-separation pathways in photosystem II: Modeling of transient absorption kinetics. ChemPhysChem **12**(3) (2011), 681–688. doi: 10.1002/cphc.201000830.

13. V. I. Novoderezhkin et al.: Pathways and timescales of primary charge separation in the photosystem II reaction center as revealed by a simultaneous fit of time-resolved fluorescence and transient absorption. Biophysical journal **89**(3) (2005), 1464–1481. doi: 10.1529/biophysj.105.060020.

14. J. Dostál et al.: Two-dimensional electronic spectroscopy can fully characterize the population transfer in molecular systems. The Journal of Chemical Physics **145**(12) (2016), 124312. doi: 10.1063/1.4962577.

15. W. Liptay: Dipole Moments and Polarizabilities of Molecules in Excited Electronic States. Excited States. New York: Academic Press, 1974, 129–229.

16. A. L. Stancik and E. B. Brauns: A simple asymmetric lineshape for fitting infrared absorption spectra. Vibrational Spectroscopy **47**(1) (2008), 66–69. doi: 10.1016/j.vibspec.2008.02.009.

17. S. Krawczyk: Electrochromism of chlorophyll a monomer and special pair dimer. BBA - Bioenergetics **1056**(1) (1991), 64–70. doi: 10.1016/S0005-2728(05)80073-8.

18. I. Renge and K. Mauring: Spectral shift mechanisms of chlorophylls in liquids and proteins. Spectrochimica Acta - Part A: Molecular and Biomolecular Spectroscopy **102** (2013), 301–313. doi: 10.1016/j.saa.2012.10.034.

19. S. S. Senlik et al.: Two-Color Nonlinear Spectroscopy for the Rapid Acquisition of Coherent Dynamics. Journal of Physical Chemistry Letters **6**(13) (2015), 2413–2420. doi: 10.1021/acs.jpclett.5b00861.

20. R. Moca et al.: Two-Dimensional Electronic Spectroscopy of Chlorophyll a: Solvent Dependent Spectral Evolution. The Journal of Physical Chemistry B **119**(27) (July 2015), 8623–8630. doi: 10.1021/acs.jpcb.5b04339. arXiv: arXiv:1408.1149.

21. A. Gelzinis et al.: Tight-binding model of the photosystem II reaction center: Application to two-dimensional electronic spectroscopy. New Journal of Physics **15** (2013). doi: 10.1088/1367-2630/15/7/075013.

22. L. J. Moore et al.: Excited-state electronic asymmetry of the special pair in photosynthetic reaction center mutants: Absorption and Stark spectroscopy. Biochemistry **38**(37) (1999), 11949–11960. doi: 10.1021/bi990892j.

23. S. G. Boxer: Stark Realities. Journal of Physical Chemistry B **113** (2009), 2972–2983.

24. G. U. Bublitz and S. G. Boxer: Stark spectroscopy: applications in chemistry, biology, and materials science. Annual review of physical chemistry **48** (1997), 213–242. doi: 10.1146/annurev.physchem.48.1.213.

25. D. L. Andrews and M. J. Harlow: Phased and Boltzmann-weighted rotational averages. Physical Review A **29**(5) (1984), 2796–2806. doi: 10.1103/PhysRevA.29.2796.

# CHAPTER 4

## Experimental Setup for 2DESS Experiments

In this chapter I describe the optical setup[1] that has been developed in our group that solves many of the challenges associated with making high-sensitivity 2DES measurements and discuss the analysis that must be done to reconstruct the complex third-order response. Then I show how the setup may be extended to conveniently measure both the Stark and 2DESS signals at cryogenic temperatures[2]. High signal-to-noise measurements of Stark signals require the sample to withstand a very high applied voltage near the dielectric strength limit of most materials. In the final section of this chapter I discuss the sample cell design and requirements on the samples that allow this high voltage to be reached consistently. The experimental results using this setup can be found in the following chapters.

## 4.1  *Experimental Implementation of 2DES*

Conceptually, our two-dimensional spectroscopy experiment can be broken up into three parts: the generation and compression of light sources to act as the driving fields $E_n$, the manipulation of the fields to produce a background-free geometry, and finally the heterodyne detection of the signal.
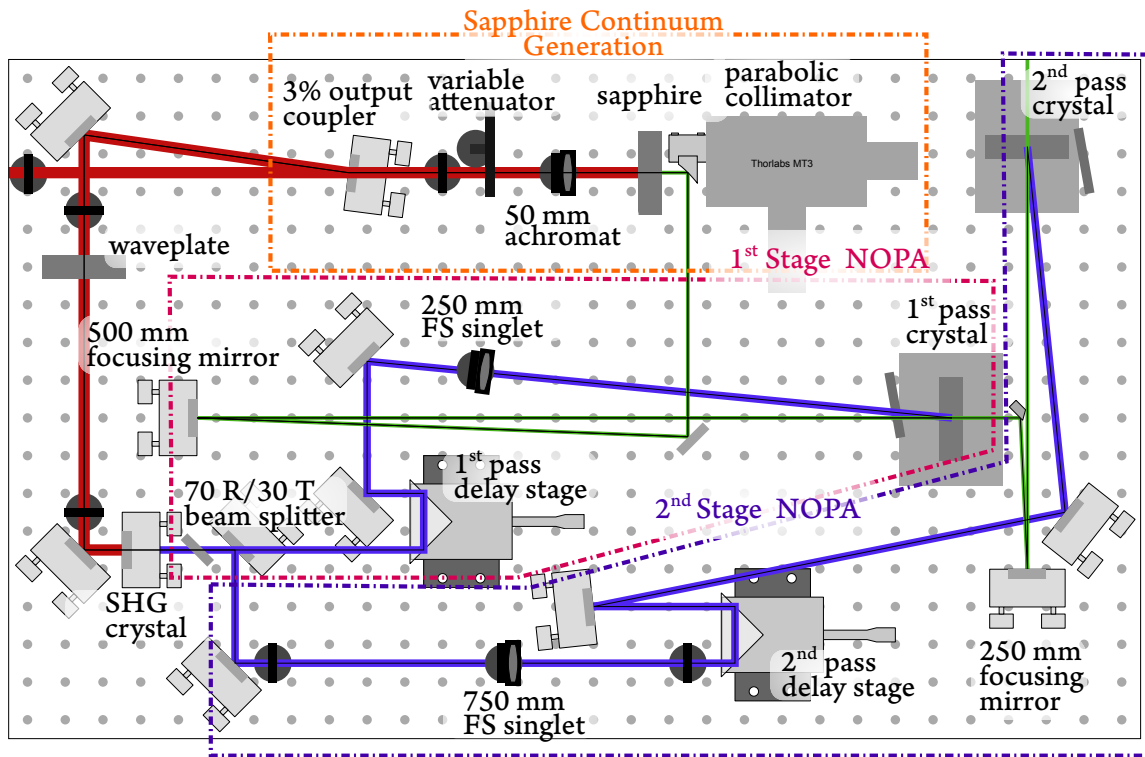
**Figure 4.1** Optical layout of NOPA. The Ti:Sapph regen beam (800 nm) enters on the left (red) and is split between the continuum generation and pump sections. The generated second harmonic is shown in blue. The continuum and generated signal is shown in green. See the text for details on components.

*Light Sources*

In our setup, a commerical pumped titanium-saphhire oscillator (SpectraPhysics MaiTai) generates 50 fs pulses centered near 800 nm at a 84 MHz repetition rate. The oscillator seeds a Ti:Sapph regenerative amplifier (SpectraPhysics Spitfire Pro) running at 500 Hz and outputting 2 mJ of energy per pulse at 800 nm. The majority of this energy is split into two home-built non-collinear optical parametric amplifiers (NOPAs) which provide stable light sources tunable from 480 nm to 720 nm.

The NOPA[3,4] utilizes two $\chi^{(2)}$ processes for operation: difference-frequency generation (DFG) and second-harmonic generation (SHG). In DFG, electric fields at two frequencies $\omega_1$

and $\omega_2$ interact in a nonlinear crystal material to produce a field at the difference frequency $\omega_s = \omega_1 - \omega_2$. Second-harmonic generation is essentially this process in reverse, yielding a field with twice the frequency of the input $\omega_s = \omega_1 + \omega_1$. In crystals without an inversion symmetry, these processes are efficient when the frequencies satisfy energy conservation and are phase-matched[5]. In most NOPA designs, β-barium borate (BBO) is the nonlinear medium of choice because of high damage threshold, low group-velocity dispersion, and low absorption over most of the visible and NIR[6].

Our NOPA design shown in Figure 4.1 is duplicated twice to provide the pump and probe beams for the 2DES experiment. About 95% of the input from the regen is used to generate second-harmonic at 400 nm in a 0.5 mm BBO crystal to provide the pump for the DFG process. The pump is split into two paths in a 30/70 ratio and sent to the the first- and second-pass mixing crystals. For both paths, fused silica retroreflectors provide chirp for the pumps and allow adjusting the temporal overlap with the seed at the crystals. The remaining 5% provides the power for continuum generation in 3 mm C-cut sapphire window that acts as a broadband seed[7]. The seed is collimated using a $f = 25$ mm off-axis parabolic mounted on a 5-axis kinematic mount and focused onto the first mixing crystal using a 500 mm spherical mirror. The first-pass pump is focused by a 25 mm fused-silica lens and spatially overlapped with the seed to produce DFG. The resulting signal is focused onto the second mixing crystal and is amplified further by the second-pass pump ($f = 75$ mm).

The bandwidth and mode of the resulting signal can be optimized by adjusting the relative angle between the seed and the pump, and their spatial and temporal overlap. To provide stable and efficient operation, it is key that the pump intensity at each mixing power is approximately $100\,\mathrm{GW/cm^2}$ and that the spot sizes of the pump and seed are well matched. Using this design, we are routinely able to generate pulses of 120 nm bandwidth with a central wavelength tunable from 530 nm to 670 nm, with a short-term stability below 1% over that bandwidth.

After generating the pump and probe pulses, each is compressed using a home-built grism compressor[8], which allows to compensate both second- and third-order dispersion. The compression of the pump and probe is performed using compressor-based MIIPS[9] to observe the effect of tuning the insertion and separation between the grisms on the second-harmonic generated in a 10 μm BBO. The pump undergoes additional compressed by an acousto-optic pulse-shaper (Fastlite Dazzler) using the SPEAR algorithm[10]. After compression, the effective time-resolution is verified by performing a TG-FROG measurement in a thin piece of fused-silica, typically yielding sub-15 fs FWHM durations.

*2D Spectrometer*

As discussed in Chapter 2, the two-dimensional electronic spectrum is generated when three broadband optical pulses interact with the sample to generate a third-order polarization. Due to the phase-matching condition, it is possible to set the wave-vectors of the fields $\boldsymbol{k}$ such that the signal is generated in a direction distinct from all of the driving fields. In our setup[1], this is achieved using a diffractive optic (DO) to produce a box-CARS-like geometry. The setup is shown in Figure 4.2. Briefly, the pump and probe paths following parallel paths are focused by a $f = 500\,\mathrm{mm}$ spherical mirror onto a custom diffraction grating (DO, 21 lines/mm) designed to produce odd orders. Using a mask, we select the $\pm 1$ orders of the pump path and denote them as $\boldsymbol{k}_{1,2}$. Along the probe path, the +1 order is selected for the probe beam $\boldsymbol{k}_3$ and the +3 order is used for the local oscillator $\boldsymbol{E}_{\mathrm{LO}}$. The diffracted beams are imaged to the sample position using a $f = 200\,\mathrm{mm}$ spherical mirror, and then the heterodyned signal generated in the rephasing $\boldsymbol{k}_I$ direction is collimated and detected with a spectrometer (Horiba Jobin-Yvon iHR320 with PIXIS 1340X100B CCD) to be read out with every laser shot $(500\,\mathrm{Hz})$.

The three time-delays for the experiment are generated as follows. The coherence time-delay $\tau$ between pump pulses is obtained with sub-fs precision using the pulse shaper (Dazzler), which
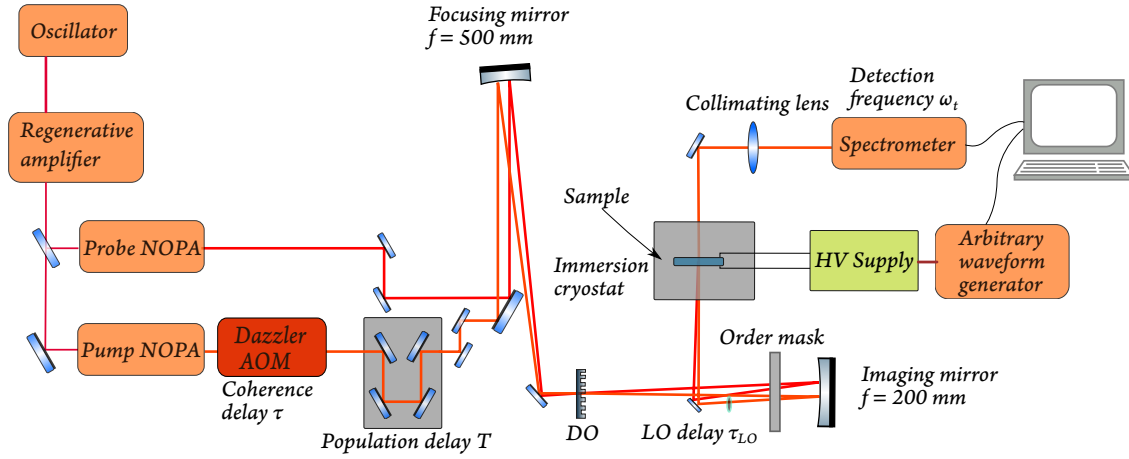
**Figure 4.2** A schematic representation of a diffractive-optic-based two-dimensional electronic Stark spectroscopy setup.

also provides compression and phase-cycling capabilities. The relative time delay between the last pump pulse and the probe $T$ is controlled by a conventional retroreflector-based delay. The heterodyned signal is detected with a spectrometer, so no scanning of the detection time $t$ is required. The heterodyne delay between the local oscillator and the probe is controlled by a thin piece of fused silica, to produce a time delay of $\tau_{\text{LO}} = 850$ fs at 650 nm.

Unlike a conventional box-CARS setup, our setup contains two pulses propagating collinearly along the pump path, resulting in six total pulses after the DO (see Figure 4.3). The signal can be generated from four combinations of the pump pulses interacting the probe; the detected signal in the $\boldsymbol{k}_I$ direction is a superposition of the rephasing signal obtained from scanning $\tau > 0$, two transient-grating signals ($\tau = 0$), and the nonrephasing signal $\tau < 0$. The three types of signals can be separated based on their phase-dependence by a technique called phase-cycling[11,12].

As essentially a broadband nested interferometer, the 2D spectroscopy experiment is particularly sensitive to phase jitter between the driving fields. By using common optics for all parts of the interferometer and generating the two pump pulses collinearly in the pulse-shaper, our setup is passively phase-stable to $\lambda/200$[1]. Further, the setup is easily configured to perform
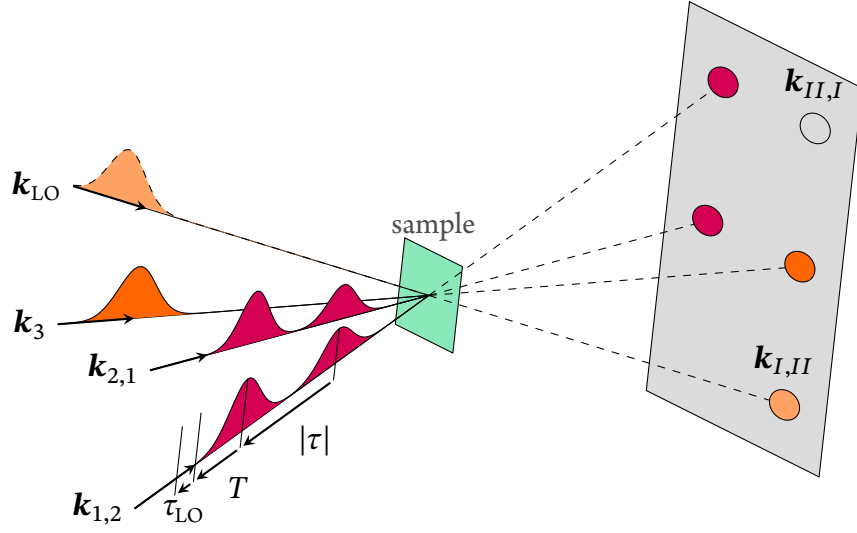
**Figure 4.3** Phase-matching diagram in the diffractive-optic pulse-shaping setup. The coherence delay $\tau$ between pumps (shown in red) is controlled with the pulse-shaper, which also applies a phase shift $(\phi_1, \phi_2)$ to each pump. The heterodyne-detected signal in the $\boldsymbol{k}_{\text{LO}}$ is recollimated and collected with a spectrometer.

transient-absorption/pump-probe measurements and linear absorption measurements by changing the mask after the DO, during the same experiment. This capability is utilized for phase-reconstruction of the complex measured signal, called "phasing."

*Signal Reconstruction*

The measured signal at the spectrometer consists of several contributions. In addition to the heterodyned signal encoding the third-order response (see §2.4), there are also several non-phase-matched contributions collectively referred to as *scatter*. The detected intensity for each pixel takes the form

$$I_{\text{measured}}(\tau, T) = \text{Re}\, E_{\text{LO}}^{\star} E_{s}(\tau, T) + I_{s}(\tau, T) + I_{\text{LO}} \tag{4.1}$$

$$+ I_{\text{pump}} + I_{\text{probe}} + \text{Re}\, E_{\text{LO}}^{\star} E_{\text{pump}} + \text{Re}\, E_{\text{LO}}^{\star} E_{\text{probe}} \tag{4.2}$$

In this expression, the first term on the right contains the rephasing, non-rephasing, and transient-grating signals. The remaining terms are unwanted signals that must be removed. Particularly bothersome are the heterodyned scatter terms, $E_{\text{LO}}^{\star}$, because they represent dynamic scatter that is amplified by the local oscillator and cannot be removed by averaging.

To extract the heterodyned signal, we use a technique borrowed from NMR called *phase-cycling*. The pulse-shaper gives a precise control over the relative phase of the pump pulses which gets imprinted on both the third-order signals and the $E_{\text{LO}}^{\star}E_{\text{pump}}$ term. Consider that we apply a phase $\phi_1$ to the first pump and $\phi_2$ to the second*. From (2.77) we can see that away from pulse-overlap, the rephasing signal will have the same phase-dependence as the $\boldsymbol{k}_I$ vector, $-\phi_1 + \phi_2$. Similarly, the non-rephasing has the opposite phase, $\phi_1 - \phi_2$, and we obtain two transient-grating signals with phases $\phi_1 - \phi_1 = \phi_2 - \phi_2 = 0$. Unlike the third-order signals, the dynamic scatter terms depend only on a single phase. Writing this expression in matrix notation we obtain

$$I_{\text{measured}}(\tau, T) = \text{Re}\left[e^{i(-\phi_1+\phi_2)} \quad e^{i(\phi_1-\phi_2)} \quad 1 \quad \frac{e^{i\phi_1}}{2} + \frac{e^{i\phi_2}}{2} \quad 1 \quad 1\right]\begin{bmatrix} E_{\text{re}}E_{\text{LO}}^{\star} \\ E_{\text{nr}}E_{\text{LO}}^{\star} \\ E_{\text{tg}}E_{\text{LO}}^{\star} \\ E_{\text{pump}}E_{\text{LO}}^{\star} \\ E_{\text{probe}}E_{\text{LO}}^{\star} \\ I_{\text{DC}} \end{bmatrix} \quad (4.3)$$

Here, I have grouped all of the intensities in the $I_{\text{DC}}$ term and split the $E_{\text{s}}$ term based on the phase-dependence of each signal. One approach to separating the signals of interest is to perform two measurements with a pair of phases shifted by $\pi$, such as $(0, \pi/2)$ and $(\pi, 3\pi/2)$, and averaging the resulting signals and canceling the pump scatter terms. In the case that it is possible to independently scan the coherence time $\tau$ independently, the rephasing and nonrephasing signals can

---

*of course due to the geometry, we will see both time-orderings of the pulse, even away from pulse-overlap

be separated as well[11]. In this setup, both positive and negative $\tau$ are scanned simultaneously, precluding the use of this technique.

Instead, we combine this $\pi$-flipping technique with a three-phase-cycle approach proposed by Zhang et al.[12] and perform 2x3 style of phase-cycling, using the phases

$$(\phi_1, \phi_2) \in \{(0,0),(\pi,\pi),(0,2\pi/3),(\pi,5\pi/3),(0,4\pi/3),(\pi,7\pi/3)\} \qquad (4.4)$$

This corresponds to adding rows to the matrix in $(4.3)$. After removing the pump scatter terms as before, the final separation is performed by inverting the matrix

$$\begin{bmatrix} E_{\mathrm{re}}E_{\mathrm{LO}}^{\star} \\ E_{\mathrm{nr}}E_{\mathrm{LO}}^{\star} \\ E_{\mathrm{tg}}E_{\mathrm{LO}}^{\star} + E_{\mathrm{probe}}E_{\mathrm{LO}}^{\star} + I_{\mathrm{DC}} \end{bmatrix} = \begin{bmatrix} 1 & 1 & 1 \\ e^{i\frac{2\pi}{3}} & e^{-i\frac{2\pi}{3}} & 1 \\ e^{i\frac{4\pi}{3}} & e^{-i\frac{4\pi}{3}} & 1 \end{bmatrix}^{-1} \begin{bmatrix} I_1 + I_2 \\ I_3 + I_4 \\ I_5 + I_6 \end{bmatrix} \qquad (4.5)$$

where $I_n$ refer to successive measurements with different phase-cycle pairs for the same coherence and population time.

The separated rephasing and non-rephasing fields are obtained by *spectral interferometery*[13]. After Fourier-transforming over the pixel to the "pseudo-time" axis $\xi \propto 1/\lambda$, the intensity terms that do not depend on the local oscillator $E_{\mathrm{LO}}$ are localized around $\xi = 0$, while the rest of the terms are near $\pm 1/\tau_{\mathrm{LO}}$. The two types of signals are separated in the Fourier plane by windowing with a supergaussian.

The $I_{\mathrm{DC}}$ terms are used to obtain the local oscillator estimate $E_{\mathrm{LO}} \approx \sqrt{|I_{\mathrm{DC}}|}$. The static scatter terms $I_{\mathrm{pump}}$ and $I_{\mathrm{probe}}$ are removed by performing auxilliary measurements using a shutter. The rephasing and non-rephasing signals may then be reconstructed by noting that

$$E_s(\tau, T, \xi) = \frac{E_s E_{\mathrm{LO}}^{\star}}{\sqrt{|I_{\mathrm{LO}}|}} \qquad (4.6)$$

In this procedure, the phase of the local-oscillator is lost leading to an unknown phase factor applied to the signals. To reconstruct it, an auxilliary pump-probe measurement at the same population time is used. This procedure is called *phasing* the 2D spectrum.

83

*Phasing*

A pump-probe signal is obtained when a pump pulse interacts twice ($\tau = 0$) with the sample to create a population that is then detected with the probe at some population time $T$ later. The measured signal is *self-heterodyned*, that is, the third-order field $E_s$ is phase-matched with the probe field and interferes at the detector to generate a pump-dependent intensity,

$$I_{pp}(T) = I_{probe} + I_{pump} + \text{Re}\{E_{probe}^{\star}E_s(I_{pump})\} \tag{4.7}$$

$$S_{pp}(T) \equiv \frac{I_{pp}(T) - I_{probe}}{\sqrt{|I_{probe}|}} \tag{4.8}$$

This signal represents the real absorptive projection of the third-order response of the sample at $\tau = 0$. The full complex signal is obtained by the heterodyned-2DES experiment with an unknown relative phase. The phasing process consists of applying a phase-correction to the measured 2D signal to make it match the pump-probe, assuming that the pump scatter term $I_{pump}$ is small. This is achieved by nonlinear least-squares minimization of the residual at some population time,

$$R^2 = \sum_{\omega_t} \left\| S_{pp}(T, \omega_t) - \frac{1}{2} \text{Re}[\left(S_{RE}^{(3)}(\tau = 0, T, \omega_t) + S_{NR}^{(3)}(\tau = 0, T, \omega_t)\right) \exp(-i\phi(\omega_t))] \right\|_2$$

$$= \sum_{\omega_t} \left\| \text{Re}[S_{pp}(T, \omega_t) - S_{TG}^{(3)}(T, \omega_t) \exp(-i\phi(\omega_t))] \right\|_2 \tag{4.9}$$

where $\phi(\omega_t)$ is a second-order polynomial, and the transient-grating signal $S_{TG}^{(3)}$ has been defined[*]. Here, exponential term represents the relative phase accumulated by the local oscillator compared to the probe due to the delay plate. After the polynomial coefficients are found, the global phase is applied to measured 2D spectra for all subsequent $(\tau, T)$ combinations.

---

[*]$S_{TG}^{(3)}$ contains the same information information as the pump-probe signal, but can be obtained in a background-free geometry and is less susceptible to scatter. In order to obtain the absorptive part of the third-order response, however, it requires phasing.

The real absorptive 2D spectrum is then obtained as the real part of the Fourier-transformed rephasing and non-rephasing spectrum.

$$S_{2d}^{(3)}(\omega_\tau, T, \omega_t) = \frac{1}{2}\operatorname{Re}\left[S_{RE}^{(3)}(-\omega_\tau, T, \omega_t) + S_{NR}^{(3)}(\omega_\tau, T, \omega_t)\right] \qquad (4.10)$$

In practice, after windowing the signal using a Kaiser window and zero-padding, the FFT is applied over $\tau$ to obtain the detection axis[14]. Prior to the transformation, the time-zero point $\tau = 0$ is scaled by 1/2 to prevent a baseline offset in the single-sided FFT. See Bracewell for details. The detection axis $\omega_t$ is interpolated to even frequency spacing by the method of Dorrer et al.[15].

## 4.2  Implementation of 2DESS

We used an optical liquid-nitrogen immersion cryostat[16] (Janis) extended with a sample holder and custom feedthrough designed to withstand high voltages without breakdown (see Figure 4.4). The use of an immersion cryostat simplifies electrical connections to the sample as the sample cell does not need to be sealed, and allows very rapid cooling by submersing the sample in liquid nitrogen[16]. The sample cell consisting of conductive transparent indium-titanium oxide (ITO) coated microscope slides is attached to a sample rod (G10 composite) by two copper electrodes. Indium wire is applied between the copper electrodes and the sample cell to provide better electrical contact and to prevent cracking of the glass slides. Voltage is applied to the electrodes by a feedthrough made of hollow alumina rods with an epoxied copper rod core, to which teflon-jacketed coaxial cable (RG 400) has been soldered.

The cryostat was originally designed to be used by quenching the sample in liquid nitrogen, rapid cooling the sample. We have found that ambient humidity causes tiny crystals to form in the liquid nitrogen which cause intermittent scatter effects. In absorption measurements this is not a significant probem because scatter shows up as a fluctuating baseline that can be averaged out. Unlike in conventional Stark experiments, in the 2DES experiment the scatter shows up as dynamic

non-phase-matched signal that interferes with the local oscillator to produce high amplitude fluctuation that can swamp the signal. We fill the sample chamber by condensing filtered nitrogen gas instead. In this modality the sample is cooled from room temperature to 77 K in about 5 min, with an additional 15 min required to fully submerge the sample. Swapping samples is done by purging the chamber with nitrogen gas until all liquid nitrogen evaporates and then repeating the cooling process.

To generate the high-voltage waveform, an arbitrary waveform generator (AWG, Agilent 33500B) is configured to generate a tapered-cosine window of variable amplitude, which is amplified 1,000 V/V by a high-voltage power supply (TReK 10/10B-HS) to a maximum applied voltage of 10 kV. The AWG is synchronized with the pulse-shaper to produce field-on/field-off waveform of 50% duty cycle such that a phase-cycle block is collected each half-cycle. The applied voltage is recorded using an ADC (National Instruments) and is used to tag the measured spectra.

After the signal is collected, the measured spectra are split into two groups based on applied voltage and the 2DES analysis is performed on each group. The resulting phased 2D is then subtracted to generate a 2DESS spectrum. The transient-grating Stark measurement (TGESS) is performed in the same way, but in that case the length of the phase-cycle block is 4 waveforms instead of 6. The Stark measurement is performed on the same setup by blocking all beams but the local oscillator at the mask (see §4.1) and detecting the change in the transmission spectrum as a function of applied field. This experiment is routinely done to verify that the voltage is being applied to the sample, before a more time-consuming experiment is performed.

### 4.3   *Sample Cell Preparation*

A primary challenge in Stark spectroscopy is consistently reaching a large applied voltage. The signal scales roughly quadratically with the field, so small improvements near the limit of the dielectric breakdown yields large dividends. Using our setup, we have been consistently able to reach
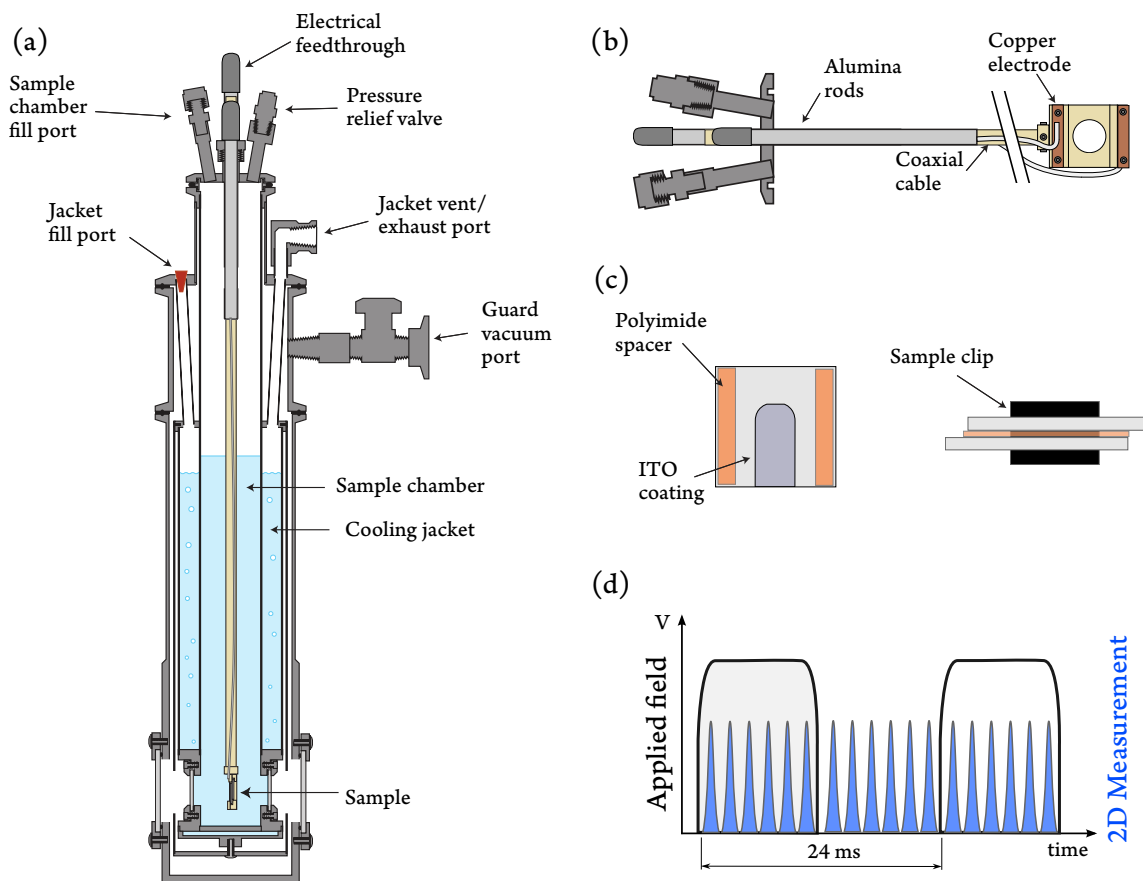
**Figure 4.4** 2DESS experiment setup. (a) Liquid nitrogen immersion cryostat (b) detail of custom sample holder showing copper mounting electrodes and feedthrough (c) ITO sample-cell design showing etching pattern and assembly (d) 2DESS timing diagram. Laser triggers corresponding to six phases are shown in blue. AWG waveform is shown in black. Image of cryostat adapted from[16]. The original image was graciously provided by Steven Andrews. Used with permission.

applied approaching 2 MV/cm. This is achieved by careful treatment of the ITO slides making up the sample cell and by optimizing the quality of the glassy-matrix that is used to suspend the sample.

*Sample cell*

The sample cell consists of two etched ITO slides separated by a 50 μm polyimide spacer that are held together with micro-size binder clips or optical adhesive. The ITO coated microscope slides obtained from Delta Technologies ($25 \times 25 \times 1.1$mm, $30\,\Omega$ to $60\,\Omega$) are cleaned with acetone and then ethanol, and a mask is painted on using nail-polish. The shape of the mask is chosen so as to provide a large-enough area of uniform field while preventing "creepage" along the surface. We found that a disk of 4 mm diameter provides enough area to find a scatter-free spot while preventing breakdown. The slides then etched following the protocol in Appendix B.

When preparing the sample-cell for water-soluble samples like those in Chapter 6, the etched ITO slides are coated with a thin uniform layer of PMMA by spin-coating. We have found that this increases the effectiveness of cryoprotectants by decreasing water adhesion and increases the effective mean-free-path to prevent dielectric breakdown. After spin-coating, the excess coating on the edges of the electrodes was removed by rubbing with toluene. About 20 μL of sample was then applied onto one slide and then covered by the second and held together by binder clips. For the experiments on photosynthetic reaction centers, this procedure is performed in a glovebag filled with nitrogen to avoid significant exposure to oxygen.

For experiments on chlorophyll a in ethanol and TIPS-pentacene in 3-methylpentane, the PMMA coating step was skipped. Due to the slow cooling rate of the cryostat, the sample cell had to be sealed to prevent evaporation of the volatile solvents. A UV-curable epoxy (Norland 62) was applied to polyimide spacers and to one side of the cell. After the cell was exposed to UV for 3 min, the sample was loaded by capillary action through the exposed side. After this, the cell was

rotated so that the remaining side was facing down and then it was sealed with a small amount of glycerol.

The use of glass spacer beads and epoxy has also been used to seal the sample cell in an atmosphere of nitrogen. This was required to run experiments on pentacene films which are sensitive to oxygen.

Each cell was then mounted to the sample holder and indium wire was placed between the copper electrodes and the ITO slides to improve electrical contact. After the experiment, the cell is discarded.

*Samples*

For experiments on TIPS-pentacene of Chapter 5, the epoxied cell protocol was used. To prepare the sample, TIPS-pentacene was dissolved in 3-methylpentane such that the final optical density was 0.3 at 1.93 eV at room temperature for a 50 μm path length cell. All reagents were purchased from Sigma-Aldrich.

Active photosystem II reaction centers (see Chapter 6) were prepared by the protocol in Appendix A. Briefly, samples were isolated from spinach by first isolating PSII membrane fragments by the method of Berthold et al.[17] and then converting them to active PSII RCs by treatment with Triton-X100 and β-DM by an extension of a protocol developed by Leeuwen et al.[18]. The sample was concentrated with a 30K NMWL centrifugal filter (Millipore) and diluted with a 50/50 mixture of glycerol/ethylene glycol (% w/w) such that the final OD in 50 μm was 0.3. Just before loading the sample, 1% by volume of ice-blockers[19,20] X-1000 and Z-1000 was added as well. Full description of the protocol and buffers can be found in the appendix.

### 4.4 Conversion Factors

Dipole moments are conventionally measured in Debye, $1\,\text{D} \equiv 3.34 \times 10^{-30}\,\text{C m}$. Polarizibility is usually expressed in cgs units as $1\,\text{Å}^3 \equiv 1.113 \times 10^{-40}\,\text{C m}^2\,\text{V}^{-1}$.

### References

1. F. D. Fuller et al.: Pulse shaping based two-dimensional electronic spectroscopy in a background free geometry. Opt. Express **22**(1) (2014), 1018–1027. doi: 10.1364/OE.22.001018.

2. A. Loukianov et al.: Two-dimensional Electronic Stark Spectroscopy. The Journal of Physical Chemistry Letters (2017), acs.jpclett.6b02695. doi: 10.1021/acs.jpclett.6b02695.

3. T. Wilhelm et al.: Sub-20-fs pulses tunable across the visible from a blue-pumped single-pass noncollinear parametric converter. Optics Letters **22**(19) (1997), 1494. doi: 10.1364/OL.22.001494.

4. G. Cerullo and S. De Silvestri: Ultrafast optical parametric amplifiers. Review of Scientific Instruments **74**(1 I) (2003), 1–18. doi: 10.1063/1.1523642.

5. R. Boyd: Nonlinear optics. Third. Burlington, MA: Academic Press, 2008.

6. E. Riedle et al.: Generation of 10 to 50 fs pulses tunable through all of the visible and the NIR. Applied Physics B **71**(3) (2000), 457–465. doi: 10.1007/s003400000351.

7. M. Bradler et al.: Femtosecond continuum generation in bulk laser host materials with sub-µJ pump pulses. Applied Physics B: Lasers and Optics **97**(3) (2009), 561–574. doi: 10.1007/s00340-009-3699-1.

8. S. Kane and J. Squier: Grism-pair stretcher–compressor system for simultaneous second- and third-order dispersion compensation in chirped-pulse amplification. Journal of the Optical Society of America B **14**(3) (1997), 661. doi: 10.1364/JOSAB.14.000661.

9. B. Hou et al.: Compressor optimization with compressor-based multiphoton intrapulse interference phase scan (MIIPS). Optics Letters **37**(8) (2012), 1385–1387. doi: 10.1364/OL.37.001385.

10. D. E. Wilcox and J. P. Ogilvie: Comparison of pulse compression methods using only a pulse shaper. Journal of the Optical Society of America B **31**(7) (2014), 1544. doi: 10.1364/JOSAB.31.001544.

11. J. A. Myers et al.: Two-color two-dimensional Fourier transform electronic spectroscopy with a pulse-shaper. Opt. Express **16**(22) (2008), 17420–17428. doi: 10.1364/OE.16.017420.

12. Z. Zhang et al.: Phase-cycling schemes for pump-probe beam geometry two-dimensional electronic spectroscopy. Chemical Physics Letters **550** (2012), 156–161. doi: 10.1016/j.cplett.2012.08.037.

13. L. Lepetit et al.: Linear techniques of phase measurement by femtosecond spectral interferometry for applications in spectroscopy. Journal of the Optical Society of America B **12**(12) (1995), 2467. doi: 10.1364/JOSAB.12.002467.

14. R. N. Bracewell: The Fourier Transform and its Applications. 3rd. Singapore: McGraw-Hill, 2000.

15. C. Dorrer et al.: Spectral resolution and sampling issues in Fourier-transform spectral interferometry. Journal of the Optical Society of America B **17**(10) (2000), 1795. doi: 10.1364/JOSAB.17.001795.

16. S. S. Andrews and S. G. Boxer: A liquid nitrogen immersion cryostat for optical measurements. Review of Scientific Instruments **71**(9) (2000), 3567–3569. doi: 10.1063/1.1287343.

17. D. A. Berthold et al.: A Highly Resolved, Oxygen Evolving Photosystem II Preparation from Spinach Thylakoid Membranes. Federation of European Biochemical Societies Letters **134**(2) (1981), 231–234.

18. P. J. van Leeuwen et al.: Rapid and simple isolation of pure photosystem II core and reaction center particles from spinach. Photosynthesis Research **28**(3) (1991), 149–153. doi: 10.1007/BF00054128.

19. B. Wowk et al.: Vitrification enhancement by synthetic ice blocking agents. Cryobiology **40**(3) (2000), 228–236. doi: 10.1006/cryo.2000.2243.

20. B. Wowk and G. M. Fahy: Inhibition of bacterial ice nucleation by polyglycerol polymers. Cryobiology **44**(1) (2002), 14–23. doi: 10.1016/S0011-2240(02)00008-1.

## CHAPTER 5

### Demonstration of Two-dimensional Electronic Stark Spectroscopy

### *5.1    Introduction*

Characterizing ultrafast energy and charge transfer is important for our understanding of systems
ranging from natural photosynthetic complexes to organic semiconductors. Two-dimensional
electronic spectroscopy (2DES) has been shown to be a powerful method for studying electronic
structure, dynamics and energy transfer in a wide range of systems[2–4]. As a third-order non-
linear spectroscopy, 2DES is closely related to transient absorption spectroscopy. In 2DES the
excitation pulse in a transient absorption experiment is split into two pulses separated by a time
$\tau$. Following the second excitation pulse, a third pulse probes the sample after a "waiting time" $T$.
The complex signal field is resolved as a function of both $\tau$ and the time following the third pulse
($t$). The Fourier transform of the signal with respect to $\tau$ and $t$ yields the respective excitation and
detection axes of the 2D spectrum for a given waiting time $T$. At $T = 0$, the 2D spectrum pro-
vides rich information about electronic structure: the peak shapes along the diagonal provide a
measure of homogeneous and inhomogeneous broadening, while cross-peaks indicate electronic
coupling[3]. The waiting time evolution of the 2D spectrum reveals the relaxation dynamics and
has been used to map energy transfer pathways[2,5]. In many systems of interest, identifying charge

transfer states, which are often nonradiative, is considerably more difficult, and theoretical studies have shown that 2D spectra are often relatively insensitive to charge separation pathways[6].

In Stark spectroscopy, also commonly referred to as electro-absorption spectroscopy, the linear absorption of the sample is measured with and without the application of a large DC (Stark) electric field, and the differential linear absorption is reported. This approach, which is a one-dimensional measurement, has proven to be a valuable method for uncovering charge transfer (CT) states in photosynthetic reaction centers[7–9] and other systems[10,11]. The presence of a large large electric field Stark-shifts energy levels and also influences the movement of charge. A number of time-resolved measurements have used electric-field modulation to investigate charge carrier generation and dynamics in a range of materials using photoluminescence[12], photocurrent[13], second-harmonic generation[14] and pump−probe spectroscopies[11,15–18]. The magnitude of the electric-field-dependent signal is often small[15], necessitating a sensitive spectroscopic method. Here we combine 2DES with Stark spectroscopy, extending the dimensionality of previous Stark spectroscopy measurements by performing differential 2DES with and without the application of a Stark electric field. The resulting two-dimensional electronic Stark spectroscopy (2DESS) resolves the Stark shifts of the system along both excitation and detection frequency axes as a function of waiting time. Like Stark spectroscopy, the method promises to reveal CT states. The additional frequency dimension of 2DESS should reveal coupling of these states to other states of the system. For systems where the Stark field modifies the charge separation kinetics, the waiting time dependence of the 2DESS spectrum promises to directly report the difference in kinetics, highlighting the states involved in the charge separation process. The same experimental setup can readily perform transient- grating electronic Stark spectroscopy (TGESS). Given that transient-grating spectroscopy offers improved sensitivity compared to pump−probe spectroscopy and enables phase-resolved measurements[19], we expect that TGESS offers advantages over electric-field-modulated pump−probe spectroscopy. Here we demonstrate 2DESS and

93

TGESS on $6,13-\mathrm{bis}$(triisopropylsilylethynyl pentacene) in 3-methylpentane at 77 K. TIPS-pentacene was chosen for its large Stark response and recent interest in this material for photovoltaic applications[20].

## 5.2 Theory

The shift in energy $\Delta\mathcal{E}$ of an electronic transition in response to an applied electric field $\boldsymbol{F}$ is given by

$$\Delta\mathcal{E} = -\Delta\widehat{\boldsymbol{\mu}} \cdot \boldsymbol{F} - \frac{1}{2}\boldsymbol{F} \cdot \Delta\widehat{\boldsymbol{\alpha}} \cdot \boldsymbol{F} \tag{5.1}$$

where $\Delta\widehat{\boldsymbol{\mu}}$ and $\Delta\widehat{\boldsymbol{\alpha}}$ are the respective changes in dipole moment and polarizability between the initial and final states[21]. The large $\Delta\widehat{\boldsymbol{\mu}}$ associated with CT states enables their observation by Stark spectroscopy. The sensitivity of Stark spectroscopy to $\Delta\widehat{\boldsymbol{\alpha}}$ provides insight into the interactions between a molecule and its local environment. A Stark spectrum is frequently decomposed into a linear combination of first- and second-derivatives of the linear absorption spectrum with respect to frequency. For isolated transitions from nonoriented, immobilized samples, the first and second derivative contributions to the Stark spectrum are associated with $\Delta\widehat{\boldsymbol{\alpha}}$ and $\Delta\widehat{\boldsymbol{\mu}}$ respectively[21]. Additionally, a zero derivative contribution may be present due to a change in the transition dipole moment in the presence of the Stark field. In (5.1), $\boldsymbol{F}$ is the local field experienced by a molecule which differs from the macroscopic field due to intermolecular interactions and solvation effects[21,22]. We avoid the dependence on a particular solvation model by describing the local field as $\boldsymbol{F} = f\boldsymbol{E}$, where $f$ is a dimensionless scalar local-field correction factor and $\|\boldsymbol{E}\| = V/d$ is the external field, calculated as an applied voltage drop $V$ over a plate separation $d$[21]. This approach straightforwardly generalizes to nonlinear interactions[23].
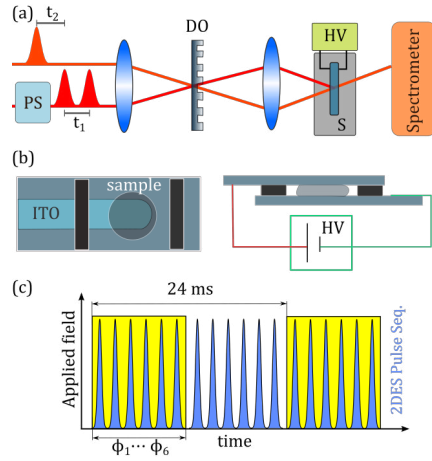
**Figure 5.1** Experimental setup for two-dimensional electronic Stark spectroscopy. (a) The hybrid pulse-shaping/diffractive optics-based 2DES setup[24], where PS = pulse-shaper, DO = diffractive optic, HV = high voltage, S = sample. The lenses are shown for simplicity only; in the setup a spherical mirror (f = 500 mm) is used to focus the beams onto the diffractive optic (DO), and a patterned spherical mirror (f = 200 mm) is used to relay the focus at the DO to the sample position. The reflective coating is etched away to selectively attenuate the local oscillator. (b) The Stark cell design. (c) The timing diagram for the sequence of phase-cycled optical pulses and the applied electric field in a 2DESS experiment.

## 5.3 Methods

The experimental setup for 2DESS and TGESS is shown in Figure 5.1 and employs a hybrid diffractive-optics/pulse-shaping approach for the 2DES measurements[24]. The output of a regenerative amplifier (SpectraPhysics Spitfire Pro) operating at 500 Hz was used to pump two dual-stage non-collinear optical parametric amplifiers (NOPAs)[25] to provide the pump (centered at 620 nm, 60 nm full-width-half-maximum (FWHM) bandwidth) and probe (centered at 620 nm, 85 nm FWHM bandwidth) pulses. Both pump and probe pulses were compressed with grism compressors[26]; for the pump pulse this serves to enable broader bandwidth operation of the Dazzler pulse-shaper, which produces a collinear 16 fs pulse pair separated by the desired $\tau$ and with relative phase $\phi_n$. A separate grism compressor provided the full pulse compression for the probe pulse (17 fs). The pump was chopped and advanced relative to the probe by delay $T$ using a

retroreflector on a linear translation stage. The pump and probe were focused onto a diffractive optic to generate the background-free passively phase-stable 2DES geometry and a delayed local oscillator for heterodyne detection. The beams, with parallel relative polarizations and pulse energies of 34 nJ and 30 nJ (pump and probe respectively), were spatially overlapped and focused to a 180 μm spot on a Stark sample cell in a liquid nitrogen immersion cryostat (Janis)[27].

To prepare the sample, TIPS-pentacene was dissolved in 3-methylpentane such that the final optical density was 0.3 at 1.93 eV at room temperature for a 50 μm path length cell. All reagents were purchased from Sigma-Aldrich. The concentrated sample was loaded into a custom sample cell composed of etched conductive (ITO) cover slides separated by a 50 μm (nominal) polyimide spacer and sealed on three sides with Norland 68 optical adhesive. After loading, the cell was sealed on the remaining side by a layer of glycerol. An arbitrary waveform generator (AWG) (Agilent 33500B) synchronized to the laser trigger was used to generate a variable-amplitude lowpass-filtered square-wave with period of 24 ms and 50 % duty cycle. The AWG output was used to drive a high voltage power supply (TReK 10/10B-HS) that induced an applied electric field of up to 2.2 MV/cm/f in the sample. The heterodyned signal was detected with a spectrometer (Horiba Jobin-Yvon iHR320 and PIXIS 1340X100B CCD) and was read-out at every laser shot (500 Hz).

The 2DESS data was generated as follows. For each $\tau$ delay, the external field was modulated (Figure 5.1c) such that a group of six phase cycles ($\phi_1 - \phi_6$) was collected for each half-cycle of the modulation. For 10% of the CCD integration time the probe was blocked with a shutter to collect background. The total CCD integration time per $\tau$ was 5 s. At each delay $T$, 60 $\tau$ points were collected from 0 fs to 390 fs (step size of 6.61 fs). A full 2DESS spectrum took about 5 min to acquire. After spectral interferometry, phase-cycling, and Fourier-transformation of the $\tau$ axis, the isolated rephasing and nonrephasing spectra were combined and the data "phased" to obtain 2D absorptive electronic spectra[24]. The difference between the field-on and field-off spectra obtained in this way yield the 2DESS spectrum. TGESS can be performed with this setup by setting
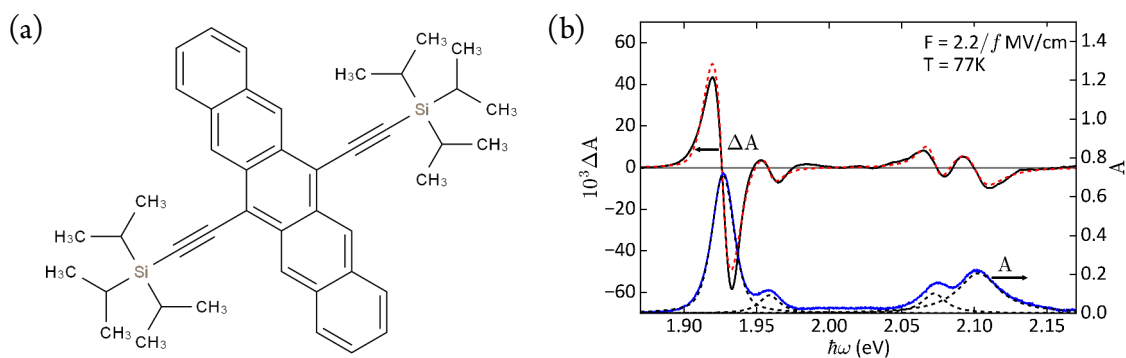
**Figure 5.2** (a) Flat chemical structure of TIPS-pentacene. (b) Top panel: Stark spectrum of TIPS – pentacene in 3-methylpentane at 77 K and 2.2 MV/cm/f applied field is shown as a solid black line. Bottom panel: Linear absorption spectrum of TIPS – pentacene in 3-methylpentane at 77 K. Dashed lines show a least-squares fit to the linear absorption spectrum (see Appendix C for details). A fit of scaled first- and second- derivatives of these lineshapes is shown as a red dashed line in the top panel; all parameters other than the amplitude of the derivatives were held fixed.

$\tau = 0$ and scanning $T$ to study electric-field-dependent kinetics. The TGESS signal is a subset of the 2DESS data and can be tupautomatically extracted via phase-cycling from 2DESS measurements[24]. Since TGESS does not require scanning of the $\tau$ delay, it can also be performed without the need for the pulse-shaper shown in Figure 5.1.

## 5.4 Results

The linear absorption and Stark spectrum of TIPS-pentacene in 3-methylpentane at 77 K are shown Figure 5.2. The dominant peak at 1.93 eV in the linear absorption spectrum is assigned to the $S_0 \rightarrow S_1$ transition of TIPS-pentacene in 3-methylpentane, while the higher energy peaks are consistent with two vibrational progressions of frequency 250 cm$^{-1}$ and 1,165 cm$^{-1}$, giving rise to transitions at 1.96 eV, 2.07 eV and 2.10 eV. These vibrational modes are in reasonable agreement with intramolecular modes identified in Raman studies of pentacene[28,29] and TIPS-pentacene[30], as well as with recent 2DES studies of thin films of TIPS-pentacene and other pentacene deriva-

tives[31]. We fit the linear absorption spectrum using pseudo-Voigt and Lorentzian lineshapes as detailed in the Supporting Information, yielding the fit shown in Figure 5.2. Two low-amplitude transitions were also identified at 2.25 eV and 2.28 eV in the linear absorption spectrum but lie outside of the spectral range of our 2DESS measurements. The Stark spectrum in the $S_0 \rightarrow S_1$ region resembles the first-derivative of the linear absorption spectrum, indicating that $\Delta\hat{\alpha}$ dominates the Stark response. Although second-derivative features have been included in the model, their contribution to the quality of the fit is negligible (see details of the fitting in the Supporting Information). These observations are consistent with recent Stark spectroscopy measurements in solid pentacene films that report $\Delta\hat{\alpha}$ contributions associated with the vibrational progression of the Frenkel exciton states[32]. This is in contrast to earlier work in which a combination of $\Delta\hat{\alpha}$ and $\Delta\hat{\mu}$ contributions were invoked to account for the respective first- and second-derivative features in the Stark spectrum of solid pentacene films[10]. For our solution studies we expect the dipole moment change to be dominated by $\Delta\hat{\alpha}$ due to the absence of intermolecular CT states that were proposed to give rise to the $\Delta\hat{\mu}$ contributions in the film studies[10].

Figure 5.3 shows the 2DES and 2DESS spectra of TIPS-pentacene at 77 K at a waiting time of $T = 1$ ns. The 2DES spectrum shows positive features along the diagonal at energies consistent with the linear absorption spectrum. In 2DES spectra, positive features arise from ground state bleach (GSB) and stimulated emission (SE) signals, while negative features indicate excited state absorption (ESA). At early waiting times, positive signals at the cross-peak position between two transitions indicate a common ground state between them. The dominant peak at 1.93 eV in the 2DES spectrum arising from the $S_0 \rightarrow S_1$ transition exhibits persistent diagonal elongation at $T = 1$ ns reflecting inhomogeneous broadening. The lower amplitude, higher-energy diagonal peaks and cross-peaks are consistent with the transitions assigned to two vibrational progressions in our fitting of the linear absorption spectrum. Above the diagonal the 2DES spectrum shows a strong ESA signal at a probe energy of $\approx$2.15 eV.
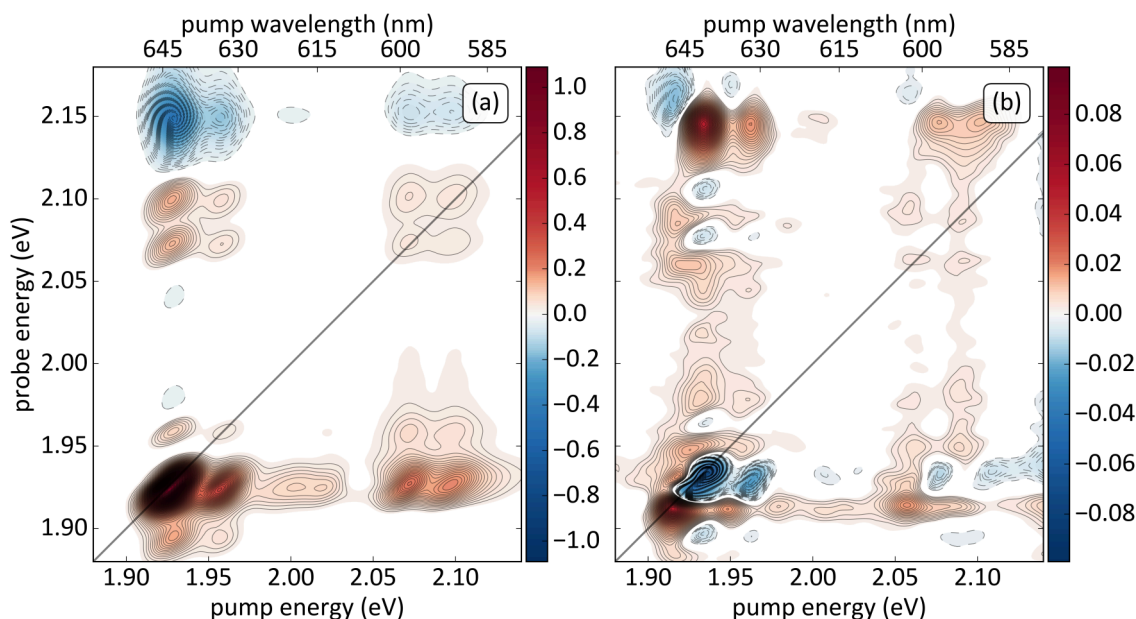
**Figure 5.3** Two dimensional spectroscopy of TIPS – pentacene in 3-methylpentane at 77 K. (a) Normalized 2D electronic spectrum (2DES) at a waiting time of $T = 1$ ns at a contour spacing of 0.01 units, omitting 3% of full-scale around zero. (b) 2D electronic Stark spectrum (2DESS) at 2.2 MV/cm/f applied field and a waiting time of $T = 1$ ns. The spectrum was multiplied by the same normalization factor as in (a). Contours have spacing of 0.001 units, omitting 3% of full-scale (0.1 units) around zero. To obtain this data, 60 $\tau$ points were collected with an integration time of 5 s per $\tau$ for a total acquisition time of about 5 min.

The 2DESS data show positive and negative features at a number of different excitation/detection energies. As a differential (field on - field off) measurement, the signed features in a 2DESS spectrum have several origins. They may arise from frequency shifts of the molecular transitions, as well as changes in transition-dipole moment with applied field. Reorientation effects may also play a role but are negligible here, where samples are frozen at 77 K. Positive 2DESS features may reflect increased positive 2DES signal amplitude (from GSB or SE) or a decrease in negative signal (ESA) in the presence of the field, while negative 2DESS features will show the opposite of these trends. The 2DESS signal near the $S_0 \rightarrow S_1$ transition resembles a first-derivative shape along the diagonal, consistent with the Stark spectrum. The relatively weaker higher energy diagonal peaks
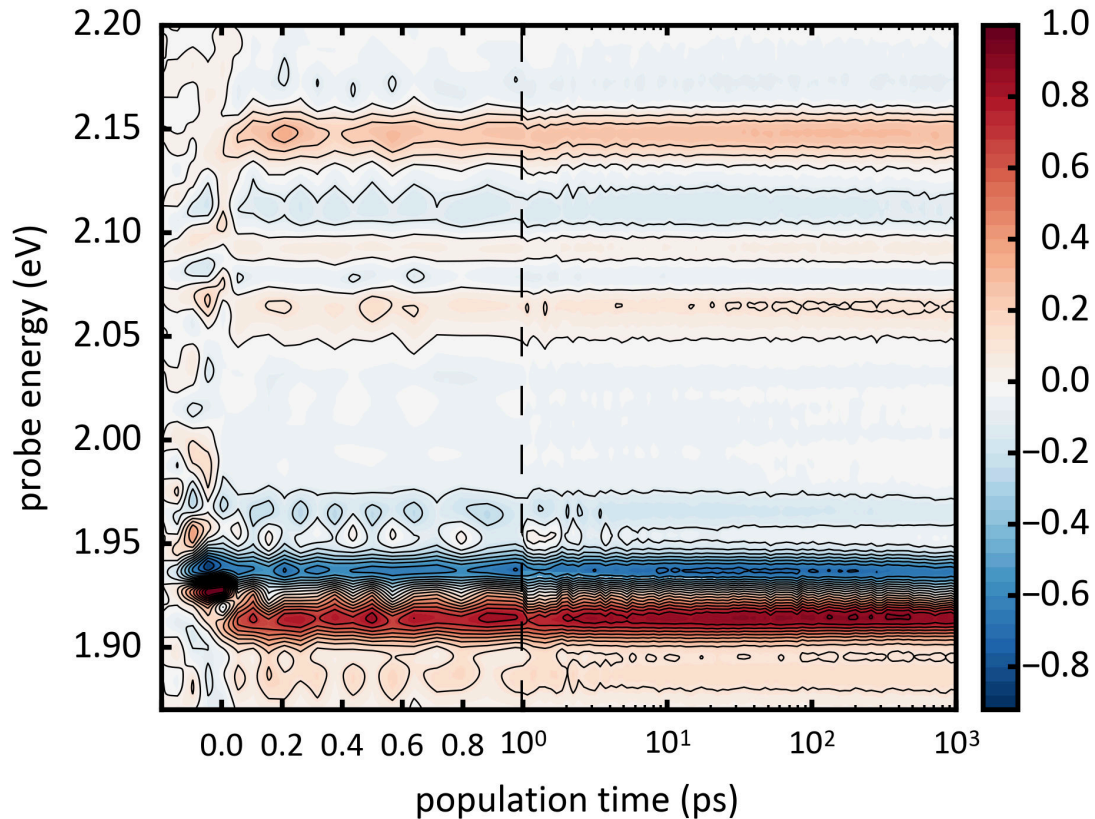
**Figure 5.4** Normalized transient grating Stark spectroscopy of TIPS – pentacene in 3-methylpentane at 77 K, recorded with a 2.2 MV/cm/f applied field. In this case, 100 $T$ points were collected with a camera integration time of 10 s per $T$ with a hyperbolic spacing. The data acquisition took 17 min.

show negligible signal, but the cross-peaks above and below the diagonal are clearly visible, due to amplification from the intense $S_0 \rightarrow S_1$ transition. The positive and negative features of the cross-peaks are consistent with a similar first-derivative type of shift of the higher energy peaks of the vibrational progression, consistent with expectations that these transitions shift in the same way as the fundamental electronic transition. As in the Stark spectrum, these first derivative shapes along the diagonal are consistent with the TIPS-pentacene transitions being dominated by changes in $\Delta\hat{\alpha}$. In the Supporting Information we provide a comparison of the Stark spectrum with the diag-

onal slice from the 2DESS data at 50 fs and 1 ns. The 2DESS spectrum also shows a large positive signal with small negative features above the diagonal at a probe energy of ≈2.15 eV. The 2DES spectrum shows a strong negative feature due to ESA at this location. We note that this ESA transition is shifted in a significantly different way from the other transitions in the 2DESS spectrum, suggesting that it is highly sensitive to the Stark field and may have some CT character.

## 5.5   *Discussion*

Like Stark spectroscopy, the 2DESS method requires immobilization of the molecule of interest, which can be achieved in a glassy matrix or by thin film preparation[21]. Our choice of 3-methylpentane as the solvent for this study was motivated by the need to obtain a high-quality optical glass at 77 K, as well as sufficient optical density over the 50 μm path length cell. We note that in this solvent, the vibrational progression is considerably better pronounced than in studies of TIPS-pentacene films[31]. In thin films or solids, intermolecular interactions lead to excitonic coupling and CT states as well as rich photophysics such as singlet fission. We expect that the combination of Stark spectroscopy and 2DESS will enable the identification of CT states and their coupling to other transitions. While CT states can be identified by their Stark response, charge separation kinetics may also be altered by the applied field, and will be evident in the waiting time dependence of the 2DESS signal. In analogy to previous studies that have used electric-field modulation to study charge carrier generation and kinetics[18] using pump–probe or other time-resolved spectroscopies, TGESS offers a high sensitivity approach. In the case of TIPS-pentacene in 3-methylpentane, no charge separation is observed, as is evident from the TGESS data shown in Figure 5.4. Following the initial changes in dipole moment and polarizability associated with photoexcitation, there is little time evolution of the signal over the ≈1 ns of the experiment with the exception of modulation due to vibrational wavepacket motion within the first few picoseconds. In conclusion, we have demonstrated 2DESS and TGESS on TIPS-pentacene at 77 K. We expect that 2DESS

will be useful for characterizing the electronic structure of molecular systems by augmenting the information about the change in dipole moment and polarizability of transitions available from Stark spectroscopy. The additional frequency dimension of 2DESS may help distinguish dipole moment and polarizability changes in samples with overlapping transitions, enabling the identification of CT states and their coupling to other transitions. The additional waiting time dimension of 2DESS may enable identification of charge separation processes and the states that drive them. The electric-field-dependent kinetics can also be characterized with TGESS, which offers a high sensitivity alternative to electric-field-modulated pump–probe spectroscopy, a method that has been useful for understanding charge photogeneration, mobility, and dynamics in photovoltaic materials[18]. In combination with 2DES, we expect the 2DESS and TGESS methods to further our understanding of the electronic structure, energy transfer, and charge separation processes in natural and artificial light harvesting systems.

## *References*

1. A. Loukianov et al.: Two-dimensional Electronic Stark Spectroscopy. The Journal of Physical Chemistry Letters (2017), acs.jpclett.6b02695. doi: 10.1021/acs.jpclett.6b02695.

2. T. Brixner et al.: Two-dimensional spectroscopy of electronic couplings in photosynthesis. Nature **434**(7033) (2005), 625–628. doi: 10.1038/nature03429.

3. D. M. Jonas: Two-dimensional Femtosecond Spectroscopy. Annual Review of Physical Chemistry **54**(1) (2003), 425–463. doi: 10.1146/annurev.physchem.54.011002.103907.

4. K. L. M. Lewis and J. P. Ogilvie: Probing Photosynthetic Energy and Charge Transfer with Two-Dimensional Electronic Spectroscopy. J. Phys. Chem. Lett. **3**(4) (2012), 503–510. doi: 10.1021/jz201592v.

5. J. P. Ogilvie and K. J. Kubarych: Chapter 5 Multidimensional Electronic and Vibrational Spectroscopy. An Ultrafast Probe of Molecular Relaxation and Reaction Dynamics. 1st ed. Vol. 57. 09. Elsevier Inc., 2009, pp. 249–321. doi: 10.1016/S1049-250X(09)57005-X.

6.  A. Gelzinis et al.: Tight-binding model of the photosystem II reaction center: Application to two-dimensional electronic spectroscopy. New Journal of Physics **15** (2013). doi: [10.1088/1367-2630/15/7/075013](10.1088/1367-2630/15/7/075013).

7.  M. A. Steffen et al.: Dielectric asymmetry in the photosynthetic reaction center. Science **264**(5160) (1994), 810–6. doi: [10.1126/science.264.5160.810](10.1126/science.264.5160.810).

8.  R. N. Frese et al.: Electric field effects on the chlorophylls, pheophytins, and beta-carotenes in the reaction center of photosystem II.. Biochemistry **42**(30) (2003), 9205–9213. doi: [10.1021/bi0273516](10.1021/bi0273516).

9.  E. Romero et al.: Mixed exciton-charge-transfer states in photosystem II: Stark spectroscopy on site-directed mutants. Biophysical Journal **103**(2) (2012), 185–194. doi: [10.1016/j.bpj.2012.06.026](10.1016/j.bpj.2012.06.026).

10. L. Sebastian et al.: Charge transfer transitions in solid tetracene and pentacene studied by electroabsorption. Chemical Physics **61**(1-2) (Oct. 1981), 125–135. doi: [10.1016/0301-0104(81)85055-0](10.1016/0301-0104(81)85055-0).

11. S. G. Boxer: Stark Realities. Journal of Physical Chemistry B **113** (2009), 2972–2983.

12. R. Kersting et al.: Ultrafast field-induced dissociation of excitons in conjugated polymers. Physical Review Letters **73**(10) (1994), 1440–1443. doi: [10.1103/PhysRevLett.73.1440](10.1103/PhysRevLett.73.1440).

13. H. Bleier et al.: Photoconductivity in trans-polyacetylene: Transport and recombination of photogenerated charged excitations. Physical Review B **38**(9) (1988), 6031–6040. doi: [10.1103/PhysRevB.38.6031](10.1103/PhysRevB.38.6031).

14. A. Devižis et al.: Ultrafast dynamics of carrier mobility in a conjugated polymer probed at molecular and microscopic length scales. Physical Review Letters **103**(2) (2009), 1–4. doi: [10.1103/PhysRevLett.103.027404](10.1103/PhysRevLett.103.027404).

15. S. G. Boxer et al.: Mechanism of charge separation in photosynthetic reaction centers: electric field effects on the initial electron transfer kinetics. Jerusalem Symposia on Quantum Chemistry and Biochemistry. **22**. Perspect. Photosynth. 1990, 39–51.

16. W. Graupner et al.: Direct Observation of Ultrafast Field-Induced Charge Generation in Ladder-Type Poly(Para-Phenylene). Physical Review Letters **81** (1998), 3259–3262. doi: [10.1103/PhysRevLett.81.3259](10.1103/PhysRevLett.81.3259).

17. J. Cabanillas-Gonzalez et al.: Photoinduced transient stark spectroscopy in organic semi-conductors: A method for charge mobility determination in the picosecond regime. Physi-

cal Review Letters **96**(10) (2006), 6–9. doi: 10.1103/PhysRevLett.96.106601.

18. J. Cabanillas-Gonzalez et al.: Pump-probe spectroscopy in organic semiconductors: Monitoring fundamental processes of relevance in optoelectronics. Advanced Materials **23**(46) (2011), 5468–5485. doi: 10.1002/adma.201102015.

19. G. D. Goodno et al.: Spectroscopy Using Diffractive Optics. Journal of the Optical Society of America B **15**(6) (1998), 1791–1794.

20. B. J. Walker et al.: Singlet exciton fission in solution. Nature Chemistry **5**(12) (2013), 1019–1024. doi: 10.1038/nchem.1801.

21. G. U. Bublitz and S. G. Boxer: Stark spectroscopy: applications in chemistry, biology, and materials science. Annual review of physical chemistry **48** (1997), 213–242. doi: 10.1146/annurev.physchem.48.1.213.

22. S. Basu: Theory of Solvent Effects on Molecular Electronic Spectra. Advances in Quantum Chemistry. Ed. by P.-O. Löwdin. **1**. Academic Press, 1964, 145–169. doi: 10.1016/S0065-3276(08)60377-9.

23. J. A. Armstrong et al.: Interactions between light waves in a nonlinear dielectric. Physical Review **127**(6) (1962), 1918–1939. doi: 10.1103/PhysRev.127.1918.

24. F. D. Fuller et al.: Pulse shaping based two-dimensional electronic spectroscopy in a background free geometry. Opt. Express **22**(1) (2014), 1018–1027. doi: 10.1364/OE.22.001018.

25. T. Wilhelm et al.: Sub-20-fs pulses tunable across the visible from a blue-pumped single-pass noncollinear parametric converter. Optics Letters **22**(19) (1997), 1494. doi: 10.1364/OL.22.001494.

26. S. Kane and J. Squier: Grism-pair stretcher–compressor system for simultaneous second- and third-order dispersion compensation in chirped-pulse amplification. Journal of the Optical Society of America B **14**(3) (1997), 661. doi: 10.1364/JOSAB.14.000661.

27. S. S. Andrews and S. G. Boxer: A liquid nitrogen immersion cryostat for optical measurements. Review of Scientific Instruments **71**(9) (2000), 3567–3569. doi: 10.1063/1.1287343.

28. R. G. Della Valle et al.: Intramolecular and Low-Frequency Intermolecular Vibrations of Pentacene Polymorphs as a Function of Temperature. The Journal of Physical Chemistry B **108**(6) (2004), 1822–1826. doi: 10.1021/jp0354550.

29. A. Brillante et al.: Structure and dynamics of pentacene on SiO 2: From monolayer to bulk structure. Physical Review B - Condensed Matter and Materials Physics **85**(19) (2012), 1–9. doi: 10.1103/PhysRevB.85.195308.

30. A. J. Musser et al.: Evidence for conical intersection dynamics mediating ultrafast singlet exciton fission. Nature Physics **11**(4) (2015), 352–357. doi: 10.1038/nphys3241.

31. A. a. Bakulin et al.: Real-time observation of multiexcitonic states in ultrafast singlet fission using coherent 2D electronic spectroscopy. Nature Chemistry **8**(January) (2016), 16–23. doi: 10.1038/nchem.2371.

32. S. Haas et al.: Field-modulation spectroscopy of pentacene thin films using field-effect devices: Reconsideration of the excitonic structure. Physical Review B - Condensed Matter and Materials Physics **82**(16) (2010), 2–5. doi: 10.1103/PhysRevB.82.161301.

# CHAPTER 6

## 2DESS Applied to the Photosystem II RC

### 6.1    Introduction

In this chapter, I apply the 2D electronic Stark spectroscopy (2DESS) developed in the previous chapters to the spinach Photosystem II reaction center preparation $D_1D_2$ Cyt $b_{559}$. The features observed show some similarity to the lineshapes of the dimer+CT system simulated in Chapter 3. Unlike the measurements on TIPS – pentacene in Chapter 5, the 2DESS and transient-absorption Stark measurements exhibit spectrally-dependent kinetics. Though extracting quantitative information from these data is challenging and improvements in signal-to-noise are required, the potential of this experiment to enable sensitive, high time-resolution detection of charge-transfer states and their coupling to other charge transfer and exciton states is evident.

### 6.2    Methods

The setup and experimental procedure are discussed in detail in Chapter 4. In these experiments, the NOPA light sources were tuned to be centered at 660 nm, and to have approximately 100 nm of bandwidth (FWHM). When compressed by the grisms, the pulses are 15 fs in duration. The Stark, TGESS, and 2DESS signals were collected at an applied voltage of 8.5 kV, corresponding to an external field of 1.7 MV/cm in the sample cell. The sample was prepared from spinach following the method of van Leeuwen[1] described in Appendix A.

Data was analyzed as discussed in §4.2. By convention, the 2DESS and TGESS spectra are
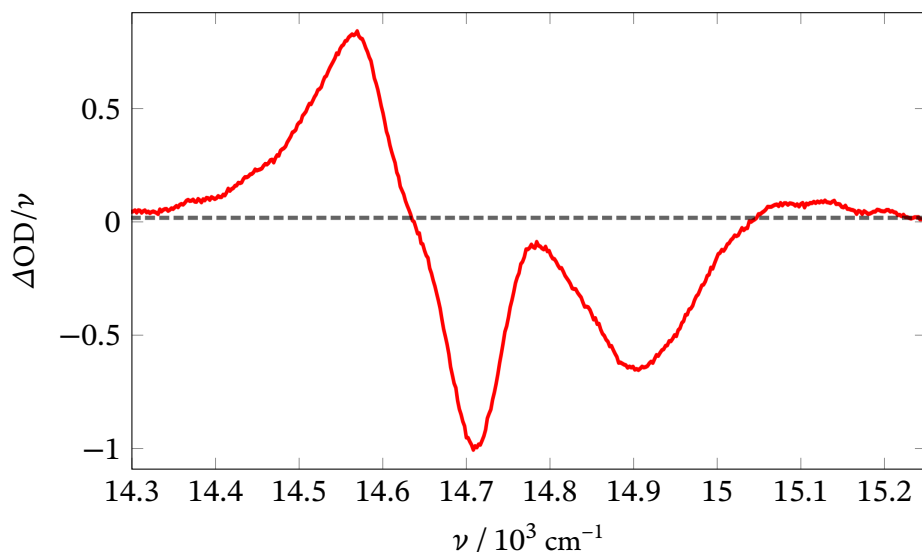
**Figure 6.1** Normalized Stark spectrum of $D_1D_2$ Cyt $b_{559}$ preparation at 77K obtained at 2.0 MV/cm applied field. The peak are located at 14.57 kK, 14.71 kK, 14.90 kK and 15.10 kK. The maximum between two negative features is at 14.77 kK.

obtained by subtracting the field-off measurements from field-on measurements,

$$S_{\text{Stark}} = S_{\text{field on}} - S_{\text{field off}} \tag{6.1}$$

All spectra are normalized to the maximum absolute value. For Stark data, the ratio of the Field off amplitude to the Stark signal amplitude is indicated by a scaling factor in the upper right of each plot. Contours are plotted exponentially with base $e$, with the smallest contour corresponding to 0.05 units. For convenience wavenumber is in kilokayser, $1\,\text{kK} \equiv 10^3\text{cm}^{-1}$.

### 6.3 Results

A Stark spectrum obtained at 77 K is shown in Figure 6.1. It exhibits three prominent features, 14.57 kK, 14.71 kK and 14.90 kK as well as broad sidebands on the blue and red sides. The measured spectrum agrees qualitatively with that obtained by Novoderezhkin et al.[2,3], however the local maximum near 14.77 kK does not cross zero as it does in that work. From voltage-dependent
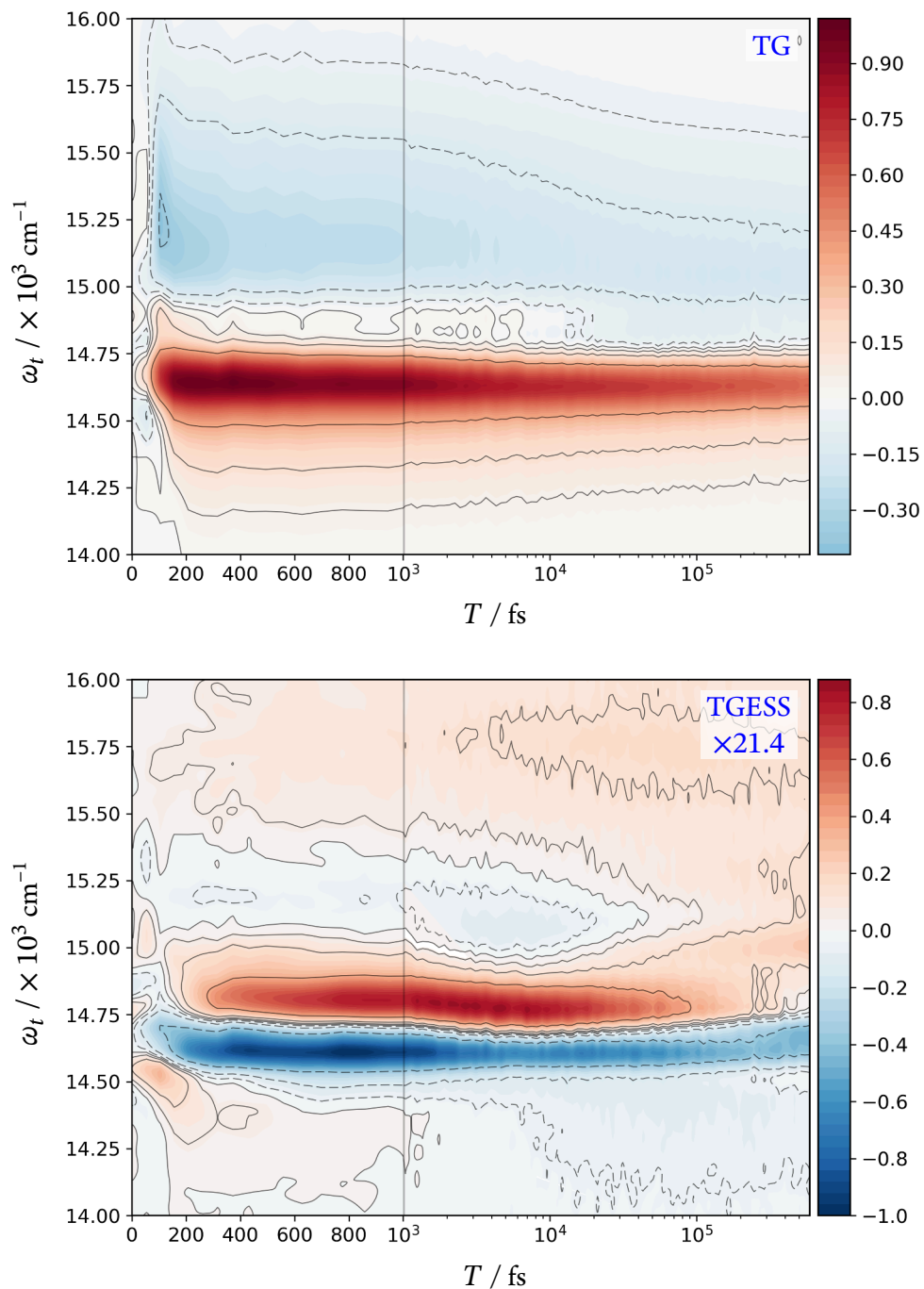
**Figure 6.2** Transient-grating (top) and TGESS spectra (bottom) of $D_1D_2$ Cyt $b_{559}$ preparation at 77K. Population time T was scanned hyperbolically to obtain both slow and fast kinetic components.

studies, we have seen that this feature decreases in magnitude as the field is applied. It is likely not observed by Novoderezhkin et al. because that data was obtained at an applied field of 0.22 MV/cm, an order-of-magnitude less than observed here. This field-dependent feature is much more evident in the 2DESS spectrum, as discussed below.

A measured TGESS spectrum is shown in Figure 6.2. Here, a negative feature indicates a loss of absorption due to the applied field. After rapid decay of a positive feature near 14.5 kK, the dominant field dependent bands occur at 14.62 kK and 14.77 kK. The strongly field-active positive band appears to grow in on a time-scale of 3 ps. The large positive feature at 14.77 kK and negative feature near 15.0 kK evolve and red-shift on $\approx$10 ps timescale.

As compared to the panel above, the TGESS spectrum exhibits features that are not evident in the TG spectrum. The most field-active positive band at 14.77 kK is clearly visible in TGESS but is quite difficult to resolve in the TG spectrum. Conversely, the large negative feature in the blue region of the TG spectrum has absolute peak amplitude of half the positive feature, yet contributes almost nothing to the TGESS, suggesting a low charge-transfer character there, consistent with the Stark spectrum.

By scanning over the excitation frequency axis $\omega_\tau$ in the 2DESS measurement, additional information about the structure of the field-active bands is revealed. As in the TGESS data, the short-lived feature is visible at 200 fs located near the diagonal (Figure 6.3). The large negative feature is localized near the diagonal, perhaps consisting of two subpeaks at $\omega_\tau = 14.70$ kK and 14.67 kK. The positive feature at $\omega_\tau = 14.77$ kK is delocalized along the excitation axis, corresponding to a decrease in intensity of the ESA feature in the 2D spectrum in the field-on case. This feature grows in intensity on the timescale of several ps (Figure 6.4) and localizes on the diagonal. The small positive feature seen in the 200 fs is not observed in the TGESS spectrum at later times due to a broadening of the negative feature at $\omega_t = 14.7$ kK, but persists throughout the spectrum. Note that these features at 200 fs are aligned well with the Stark spectrum in Figure 6.1
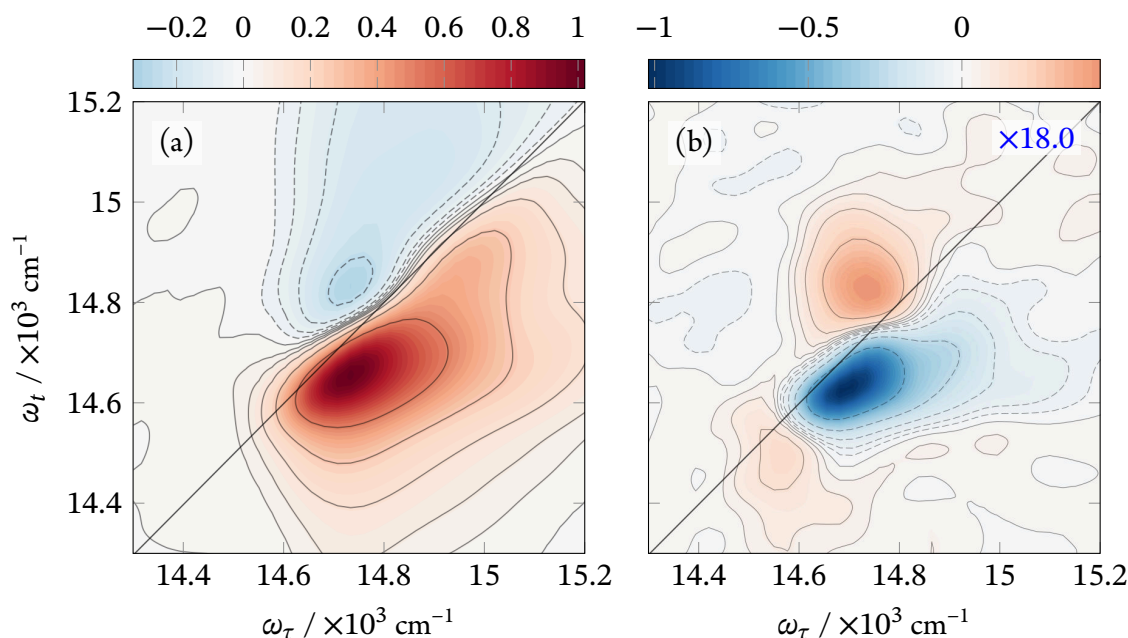
**Figure 6.3** (a) 2D and (b) 2DESS spectra of photosystem II $D_1D_2$ Cyt $b_{559}$ preparation obtained at population time $T = 200$ fs at 77 K. Applied field was 1.9 MV/cm.

when projected onto the excitation axis.

The negative feature visible in the TGESS at $\omega_t = 14.7$ kK broadens along the excitation axis on the timescale of several ps. By 10 ps, this feature is localized at two peaks, $\omega_\tau = 14.7$ kK and 14.9 kK. This localization becomes more pronounced at longer population times as energy is transferred to long-lived intermediates. The large positive feature moves to the diagonal and broadens along the excitation axis reaching its largest amplitude at 3 ps, until it splits into multiple peaks that decay at long times.

## 6.4 Discussion

Proposed mechanisms of primary charge-separation in photosystem II RC is discussed in detail in Chapter 1. In brief, two charge-separation pathways have been proposed[4], perhaps proceeding simultaneously. The "$Chl_{D1}$ pathway" is initiated when $Chl_{D1}$ acts as an electron donor to the $D_1$

**Figure 6.4** (a) 2D and (b) 2DESS spectra of photosystem II $D_1 D_2$ Cyt $b_{559}$ preparation obtained at population time $T = 3\,\mathrm{ps}$ at 77 K. Applied field was 1.9 MV/cm.

pheophytin and then proceeds to the final $P_{D1}{}^+ \, Phe_{D1}{}^-$ state on the timescale of $\approx 60\,\mathrm{ps}$[4,5].

$$RC^* \longrightarrow (Chl_{D1}^{\delta+} \, Phe_{D1}^{\delta-})^*_{\approx 14.7kK} \xrightarrow[700\,\mathrm{fs}]{} Chl_{D1}{}^+ \, Phe_{D1}{}^- \xrightarrow[58\,\mathrm{ps}]{} P_{D1}{}^+ \, Phe_{D1}{}^- \qquad (6.2)$$
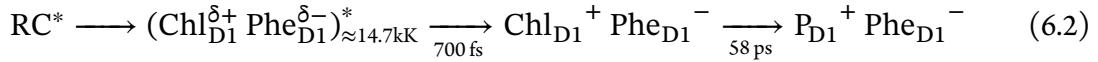
The "$P_{D1}$ pathway" was also proposed, for which the charge separation is initiated from the $P_{D1}P_{D2}$ dimer. It was hypothesized that charge-separation proceeds at a faster rate in this pathway than in the $Chl_{D1}$ pathway, though the existence and kinetics of this pathway remains controvertial.

$$RC^* \longrightarrow (P_{D1}^{\delta-} \, P_{D2}^{\delta+} \, Chl_{D1})^*_{\approx 14.8kK} \longrightarrow (P_{D2}^+ \, P_{D1}^-)^{\delta*}_{\approx 14.5kK} \xrightarrow[200\,\mathrm{fs}]{} P_{D1}{}^- \, P_{D2}{}^+$$

$$\xrightarrow[3\,\mathrm{ps}]{} Chl_{D1}{}^- \, P_{D1}{}^+ \xrightarrow[37\,\mathrm{ps}]{} P_{D1}{}^+ Phe_{D1}{}^- \qquad (6.3)$$

The apparent lifetimes previously observed in the kinetics are 0.5 ps, 3 ps and 20 ps[4,6]; the rates listed in the pathways above were obtained by target analysis using the discussed models[4,7],
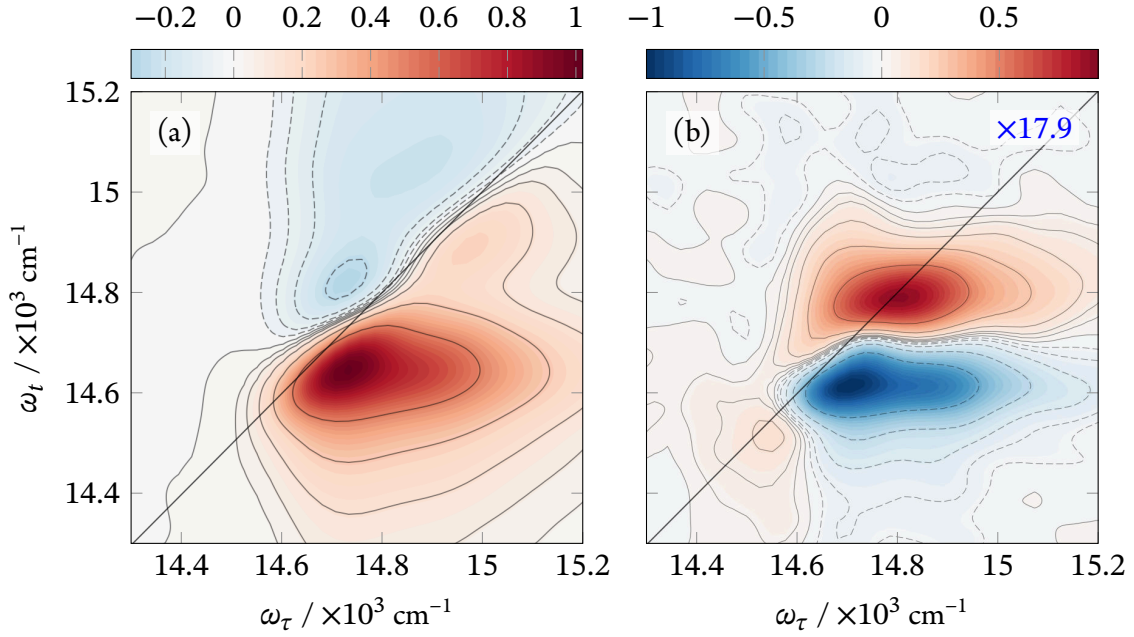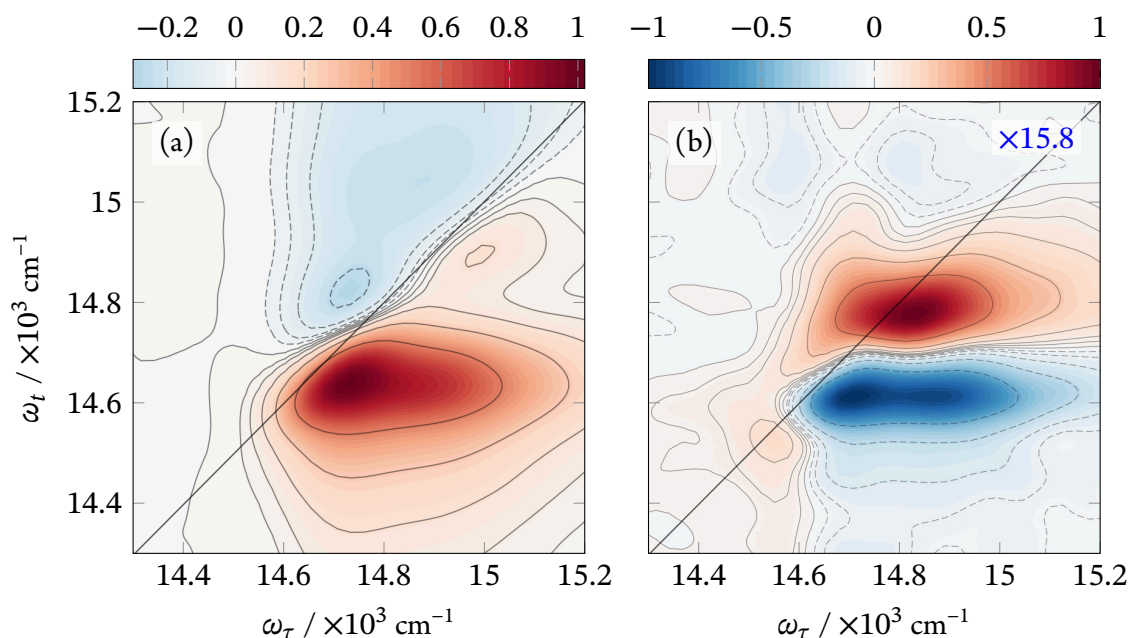
**Figure 6.5** 2D and 2DESS spectra of photosystem II $D_1D_2$ Cyt $b_{559}$ preparation obtained at population time $T = 10\,\text{ps}$ at 77 K. Applied field was 1.9 MV/cm.

with the excitonic states assigned tentative center bands based on the fitting. This assignment was later refined using a Stark/mutagenesis study[3].

The transient absorption spectrum shown in Figure 6.2(top) shows the similar kinetic rates as those seen in the literature[4,5]. The TGESS data however exhibit different kinetics, and in particular show a shift of bands as additional bands appear on the time scale of several ps. The 2DESS spectrum shows features near proposed mixed exciton-CT states at $\omega_t = 14.5\,\text{kK}$, 14.7 kK and 14.8 kK. In addition to these positions along the excitation axis, a growth of the cross-peak at $\omega_\tau = 14.9\,\text{kK}$ is evident on the timescale of tens of 10 ps, suggesting the presence of a field-sensitive CT state there. As discussed in the modeling Chapter 3, the interpretation of Stark spectra of coupled systems is complicated, so a direct assignment of bands to CT states is premature at this time. However, the additional structure evident in the 2DESS data is encouraging, and in combination with higher sensitivity experiments and global kinetic modeling, this technique offers to provide
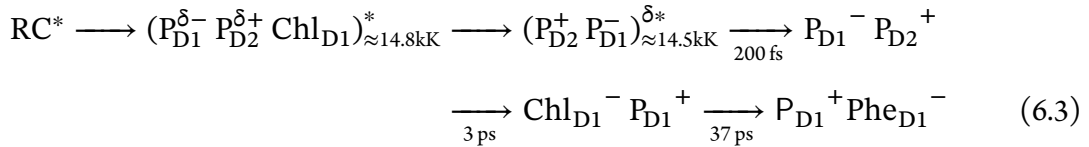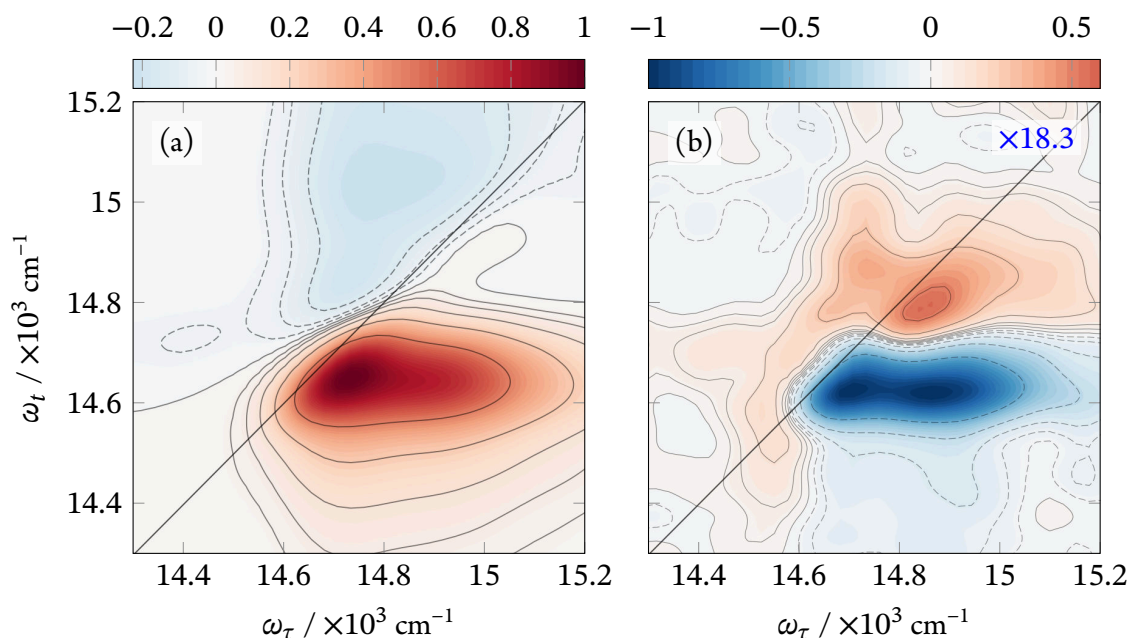
**Figure 6.6** (a) 2D and (b) 2DESS spectra of photosystem II $D_1D_2$ Cyt $b_{559}$ preparation obtained at population time $T = 50\,\mathrm{ps}$ at 77 K. Applied field was $1.9\,\mathrm{MV/cm}$.

insight into this charge-separation process.

## 6.5 Conclusion

Although it is well-known that in the PSII RC the final charge-separation is mediated by a series of charge-transfer intermediates, the detailed mechanism remains open to debate. In particular, there is evidence that there are multiple pathways that lead to the final charge-separated state that differ in the identity of the primary radical pair. A major difficulty in differentiating between proposed kinetic models is spectral overlap of the pigments participating in the reaction and the elusive nature of the charge-transfer states.

The 2DESS technique demonstrates that there is additional spectral structure in the primary charge-separation process in PSII RC that is not evident in 2DES and Stark data. To properly describe this structure, the modeling of Chapter 3 must be extended to kinetics. In combination with

robust global-fitting methods, we expect that this modeling will provide further insight for into charge-separation mechanisms in the PSII RC, allowing us to compare recently-proposed compartmental models to the data. The 2DESS and TG Stark techniques should be widely applicable to the study of ultrafast charge-transfer processes in a broad range of systems.

## References

1. P. J. van Leeuwen et al.: Rapid and simple isolation of pure photosystem II core and reaction center particles from spinach. Photosynthesis Research **28**(3) (1991), 149–153. doi: 10.1007/BF00054128.

2. V. I. Novoderezhkin et al.: Mixing of exciton and charge-transfer states in Photosystem II reaction centers: modeling of Stark spectra with modified Redfield theory. Biophysical journal **93**(4) (2007), 1293–1311. doi: 10.1529/biophysj.106.096867.

3. E. Romero et al.: Mixed exciton-charge-transfer states in photosystem II: Stark spectroscopy on site-directed mutants. Biophysical Journal **103**(2) (2012), 185–194. doi: 10.1016/j.bpj.2012.06.026.

4. E. Romero et al.: Two different charge separation pathways in photosystem II. Biochemistry **49**(20) (2010), 4300–4307. doi: 10.1021/bi1003926.

5. A. R. Holzwarth et al.: Kinetics and mechanism of electron transfer in intact photosystem II and in the isolated reaction center: Pheophytin is the primary electron acceptor. Proceedings of the National Academy of Sciences **103**(1) (2006), 6895–6900. doi: 10.1073/pnas.0505371103.

6. S. R. Greenfield and M. R. Wasielewski: Excitation energy transfer and charge separation in the isolated Photosystem {II} reaction center. Photosynthesis Research **48**(1) (1996), 83–97. doi: 10.1007/BF00040999.

7. V. I. Novoderezhkin et al.: Multiple charge-separation pathways in photosystem II: Modeling of transient absorption kinetics. ChemPhysChem **12**(3) (2011), 681–688. doi: 10.1002/cphc.201000830.

# CHAPTER 7

## Conclusions and Future Work

### 7.1  Summary and Innovations of This Work

This thesis presents my work to develop the conceptual and experimental approaches to study the primary-charge separation pathways of photosystem II. This photosynthetic enzyme has the unique capability to convert photoexcitation to stable charge-separation with near unity quantum efficiency. The conversion process proceeds via a sequence of ultrafast energy- and charge-transfer steps between multiple pigments, precisely located to facilitate charge-separation and prevent re-combination. Direct observation of charge-transfer states is challenging in practice as they are typically non-radiative.

Motivated by the success of Stark spectroscopy in revealing charge transfer states in photo-synthetic reaction centers, I have developed the 2D electronic Stark spectroscopy method. 2DESS combines the high-sensitivity of background-free heterodyne-detected 2D electronic spectroscopy with the ability of Stark spectroscopy to detect populations with large permanent dipoles. By trac-ing the spectral evolution of populations, 2DESS promises to reveal the formation and coupling of charge-transfer states to excitonic states and their role in charge-separation.

To demonstrate the potential of this technique, 2DESS and Stark spectroscopy was modeled in the modified Redfield formalism (Chapter 3) using parameters inspired by the $P_{D1}P_{D2}$ dimer of photosystem II RC. There I showed that under certain (common) conditions, the Stark spec-trum represents a projection of the 2DESS spectrum onto the excitation axis at early times. States

115

with large-CT character tend to have the largest signatures on the cross-peaks, which would cancel upon projection onto the excitation axis. This suggests that amplitudes of Stark spectra can be misleading for the purposes of assigning magnitudes of dipoles. It also suggests that Stark spectra should be inherently asymmetric and that care must be taken when fitting the Stark spectrum with sums of Gaussian lineshapes when using the Liptay formalism for weakly coupled systems. Further, it was found that in the case of large static fields and in the presence of large $\Delta\hat{\mu}$ inherent for CT states, the lineshape formalism breaks down completely. 2DESS does not have this problem and in addition allows one to observe the coupling directly. Further modeling is underway to explore how 2DESS can elucidate charge separation pathways through studies of the 2DESS signal as a function of population time.

In practice, Stark signals are quite weak, becoming detectable for applied fields near the dielectric strength of the material. Applying fields on the order of MV/cm is challenging and required the development of a custom sample cell and a modified liquid nitrogen cryostat. The apparatus and high-voltage electronics are detailed in Chapter 4. Any defects in the glassy sample facilitate breakdown and can also contaminate the weak optical signal with scatter. To prevent this, several protocols were developed to study samples in solvents and biological buffers. These can be found in the appendices. Based on this work, I demonstrated the first 2DESS experiment on TIPS – pentacene[1], found in Chapter 5.

Finally, I applied the 2DESS technique to the photosystem II RC $D_1 D_2$ Cyt $b_{559}$ preparation. I developed a protocol to consistently provide a large amount of high-quality sample for Stark experiments and developed a spin-coating technique for improving the glass-quality of the sample. With these improvements, I was able to apply fields on the order of 2 MV/cm, a value nearly double that reported previously for this sample. I then demonstrated that 2DESS and TGESS signals reveal new kinetics in $D_1 D_2$ that suggest the formation rates and locations the CT states. In combination with modeling, work is underway to interpret the complex signatures that I observed.

This technique is young, and many improvements to facilitate interpretation of complex systems are possible. They are discussed briefly in the following section.

## 7.2 Future Work

The work presented here demonstrates the feasibility and potential of the 2DESS method to facilitate the study of spectrally-congested excitonic-CT systems. Work is ongoing to further develop this technique to extract quantitative information from the resulting complicated spectra. Much like this thesis, this work can be split broadly into two categories: theory and experiment.

### Theory Improvements

As demonstrated in Chapter 6, the 2DESS spectrum exhibits interesting kinetic changes that are obscured in the broad features of the 2D spectrum. The simulation of a more complete reaction center model that reproduces these kinetics is a major task. As mentioned previously, the modeling requires a number of parameters that, in general, must be obtained by fitting. While the current simulation is too computationally expensive to include in the fitting directly, work is underway that will enable the 2DESS rotational averaging to be performed analytically, reducing the cost by three orders of magnitude. This reduction in cost will the introduction of static disorder, which was found to be a necessary component of 2D simulations to reproduce realistic system behavior[2,3].

The 2DESS technique may also be useful for detecting the breakdown of the Born-Oppenheimer approximation. Under this approximation, the vibrational structure should shift just as the underlying electronic transition in the 2DESS spectrum. It would be interesting to model several vibrational modes explicitly in the Hamiltonian, comparing the resulting 2DESS spectra with those modeled using the spectral density approach. This development may provide insight into the nature of vibronic coherences, which should be strongly modulated by the applied static field.

117

*Future Experiments*

As shown in the modeling Chapter 3, much of the interesting information of 2DESS is located in the cross-peaks. For this reason, future experimental work is focused on improving the signal to noise of the experiment such that these locations are easier to detect. Much of the fluctuation in the 2DESS spectrum is caused by the power fluctuation of the laser system. In addition to increasing the speed of acquisition of the experiment, the most direct improvement would be to detect the pump spectrum shot-to-shot and normalize the 2DESS by it. Additionally, optical polarization techniques can be used to enhance cross-peaks while suppressing diagonal features in 2D spectra. This peak-selection can be used to simplify the resulting 2DESS spectra, facilitating the interpretation of spectrally-congested systems.

Two-color 2DESS experiments provide an alternative method to select cross-peaks. It would be particularly exciting to observe the cross-peaks of proposed anion bands of CT state intermediates as they couple to the Qy region. These features should be significantly enhanced as compared to conventional 2D. In cases where spectrally-resolved excitation is not required, TGESS can be utilized to extract field-dependent kinetics with improved sensitivity as compared to pump-probe studies used for studying organic photovoltaics[4].

The degradation of biological samples under experimental conditions is a major concern that must be addressed in any study. The early studies of photosystem II reaction center in particular were controversial in that different workers observed that the reaction center could bind a varying number of photoactive pigments depending on the procedure used to isolate it[5]. Though the procedure has become fairly standardized and techniques exist to characterize the quality of the sample (see Carpentier[6]), there are still questions raised as to whether the study of the $D_1 D_2$ Cyt $b_{559}$ preparation at liquid nitrogen temperatures is relevant to the function of the complete complex in physiological conditions. There is evidence that the RC exhibits similar kinetics at both 77 K and at room temperature[7], however there are obvious advantages to studying the RC in its native

environment at room temperature and in a membrane.

In order to immobilize the RC at room temperature, it may be possible to embed the complex in nanopores of a cross-linked silica gel[8] or a nanotube array in aluminum oxide[9]. As both approaches would allow ionic conduction, the applied Stark field would have to be modulated rapidly to prevent ionic-shielding effects. This could perhaps be achieved by placing the sample into a radio-frequency transmission line. An alternative approach is generate the Stark field optically, using a terahertz-generation technique. This would allow ps temporal-resolution control of the Stark field, potentially enabling a direct control of the charge-separation kinetics. Unlike the solution samples used in this thesis, the protein complexes embedded in substrates can be made uniformally-oriented, possibly enabling direct control over the active charge-separation pathways.

With these improvements, we expect 2DESS to be useful for unraveling the dynamics of other ultrafast charge-transfer reactions in other photosynthetic reaction centers, or in the function of organic photovoltaics and singlet-fission processes.

## References

1. A. Loukianov et al.: Two-dimensional Electronic Stark Spectroscopy. The Journal of Physical Chemistry Letters (2017), acs.jpclett.6b02695. doi: 10.1021/acs.jpclett.6b02695.

2. A. Gelzinis et al.: Tight-binding model of the photosystem II reaction center: Application to two-dimensional electronic spectroscopy. New Journal of Physics **15** (2013). doi: 10.1088/1367-2630/15/7/075013.

3. K. L. M. Lewis et al.: Simulations of the Two-Dimensional Electronic Spectroscopy of the Photosystem II Reaction Center. The Journal of Physical Chemistry A **117**(1) (Jan. 2013), 34–41. doi: 10.1021/jp3081707.

4. J. Cabanillas-Gonzalez et al.: Pump-probe spectroscopy in organic semiconductors: Monitoring fundamental processes of relevance in optoelectronics. Advanced Materials **23**(46) (2011), 5468–5485. doi: 10.1002/adma.201102015.

5. C. Eijckelhoff et al.: Purification and spectroscopic characterization of photosystem II reac-

tion center complexes isolated with or without Triton X-100. Biochemistry **35**(39) (1996), 12864–12872. doi: 10.1021/bi960991m.

6.  R. Carpentier: Photosynthesis Research Protocols. Vol. 684. 2011. doi: 10.1007/978-1-60761-925-3. arXiv: arXiv:1011.1669v3.

7.  A. R. Holzwarth et al.: Kinetics and mechanism of electron transfer in intact photosystem II and in the isolated reaction center: Pheophytin is the primary electron acceptor. Proceedings of the National Academy of Sciences **103**(1) (2006), 6895–6900. doi: 10.1073/pnas. 0505371103.

8.  L. M. Ellerby et al.: Encapsulation of Proteins in Transparent Porous Silicate-Glasses Prepared by the Sol-Gel Method. Science **255**(5048) (1992), 1113–1115. doi: 10.1126/ science.1312257.

9.  A. Marek et al.: Nanotube array method for studying lipid-induced conformational changes of a membrane protein by solid-state NMR. Biophysical Journal **108**(1) (2015), 5–9. doi: 10.1016/j.bpj.2014.11.011.

# Appendices

**APPENDIX A**

**Isolation of Photosystem II Reaction Centers from Spinach**

## A.1 Introduction

The isolation procedure consists of two steps: extracting Photosystem II-enriched thylakoid membrane fragments (BBY particles) following the procedure[1] of Berthold, Babcock, and Yocum, followed by the purifcation of PSII core fragments by treatment of the BBY particles with beta-DM by the method of van Leewuen[2]. The core antenna domains as well as extrinsic proteins may be removed by treatment with a non-denaturing detergent Triton X-100 to obtain the PSII reaction center, by the method described in the same paper. Following the isolation, the RC sample is concentrated to the proper optical density for Stark experiments, diluted with an buffer containing ethylene glycol and glycerol for cryoprotection and then stored in liquid nitrogen until use.

The entire process typically takes three days. Here I describe the required equipment, isolation steps, as well as the process control steps I use to ensure a consistent preparation.

## A.2 Required Materials and Equipment

*Materials*

- Spinach (*Spinacea oleracea*) plants obtained from a local market. The leaves should be mature – this ensures a higher yield of BBY particles and less enzymatic activity than in "baby" spinach.
- Cheesecloth
- Liquid nitrogen

*Reagents*

- Acetone, Sigma-Aldrich
- Bis-Tris, Sigma-Aldrich B9754
- BSA, Fisher Scientific BP1605
- Calcium chloride dihydrate, Sigma-Aldrich C7902
- EDTA, Fisher Scientific E478
- HEPES, Fisher Scientific BP310

- Hydrochloric acid, Fisher Scientific
- Magnesium chloride hexahydrate, Fisher Scientific BP214
- Magnesium sulfate heptahydrate, Sigma-Aldrich M1880
- MES, Sigma-Aldrich M8250
- Sodium chloride, Fisher S7653
- Sodium hydroxide, Fisher S318
- Sucrose, Sigma-Aldrich S7903
- Triton X-100, Sigma-Aldrich X100
- n-dodecyl-β-D-maltopyranoside (beta-DM), Anatrace D310A
- Sepharose-Q Fast Flow, Sigma-Aldrich GE17-0510-10

*Stock Solutions*

All reagents are made up in concentrated stock and diluted to a final volume of 0.5 L with distilled water. The pH of all buffers are adjusted by adding HCl or NaOH at room temperature until a stable pH is achieved.

- HEPES, 0.5 M. Titrate to pH 7.5 with NaOH
- MES, 0.5 M. Titrate to pH 6.0 with NaOH
- EDTA, 0.5 M. Titrate to pH 8.0 with NaOH
- NaCl, 4.0 M
- $MgCl_2$, 0.5 M
- Bis – Tris, 0.5 M. Titrate to pH 6.5 with HCl
- $MgSO_4$, 0.2 M
- $CaCl_2$, 0.2 M

*Buffers for BBY Preparation*

- Grind buffer (BBY-1): 50 mM HEPES (pH 7.5), 400 mM NaCl, 2 mM $MgCl_2$, 1 mM EDTA, 2 mg/ml BSA
- Wash buffer (BBY-2): 50 mM HEPES (pH 7.5), 150 mM NaCl, 4 mM $MgCl_2$, 2 mg/ml BSA
- Triton buffer (BBY-3): 50 mM MES (pH 6.0), 15 mM NaCl, 5 mM $MgCl_2$.
- Triton solution (BBY-3T): 25 g/100 ml Triton X-100 solution in BBY-3. Weigh out Triton X-100 and pour buffer into it. Solution may need to be stirred overnight.
- Storage buffer (A): buffer A described below.

*Buffers for RC Isolation*

It is known that beta – DM degrades when exposed to moisture in the air and in solution. To ensure the effectiveness of the treatment, it is critical that the beta – DM stock is aliquoted by weight and stored in the freezer. Buffers containing beta – DM must be made up the day of the isolation and not stored.

- A: 0.4 M Sucrose, 20 mM $MgCl_2$, 5 mM $CaCl_2$, 10 mM $MgSO_4$, 20 mM Bis – Tris
- A-beta: A buffer, 0.03 g/100ml beta – DM
- B: same as A buffer but with 0.2 M Sucrose
- B-beta: B buffer, 0.03 g/100ml beta – DM
- B-beta T: 10 g/100ml Triton X-100 solution in B-beta buffer
- X: 10 g/100ml beta – DM in A-beta
- C2-beta: 80 mM $MgSO_4$ added as salt to B-beta
- Storage stock D x2: 40 mM $MgCl_2$, 10 mM $CaCl_2$, 20 mM $MgSO_4$, 40 mM Bis – Tris
- Dx2-beta: 0.06 g/100ml beta – DM in Dx2 stock

*Required Equipment*

- Blender
- High-speed centrifuge (40,000 ×g capable)
- Table-top centrifuge
- UV-VIS spectrometer
- Rubber policemen
- Stirrer and hot-plate
- Sonicator
- Vortex mixer
- Homogenizer (tissue grinder) in 55 ml, 30 ml, and 10 ml sizes
- pH meter
- Triple-beam balance
- Timer
- Graduated cylinders
- Centrifuge tubes: 40 ml, 250 ml, and 10 ml
- Erlenmeyer flasks, 2L 150 ml 250 ml
- Large funnel
- Green light
- Ice
- Peristaltic pump
- 1 cm ID liquid chromatography column with top adaptor

### A.3 Isolation of BBY Particles

To prevent enzymatic breakdown and to minimize exposure of the isolate to light, it is important to work quickly.

- Spinach grind
  - Rinse 4 bags of spinach leaves with double-distilled $H_2O$. For each bag, put about half of the spinach into the blender along with 200 ml of BBY-1. After several quick chops to make leaves fall into solution, add the rest of the spinach and grind continuously for about 15 seconds until mixture is a homogeneous slurry. Strain mixture through 4 layers of cheesecloth covering a large funnel and drain into a 2 l E. flask on ice. Gently squeeze the cheesecloth to extract most of the retained liquid. Discard cheesecloth. Repeat for the rest of the bags.
- First spin
  - Pour spinach extract into centrifuge bottles (set of 6 bottles @ 50 ml per centrifuge, total volume of 1.5 l – try not to fill bottles to top).
  - Spin 10 min @ 6,000 ×g.
  - *During spin put BBY-2 buffer, two 50ml homogenizers and tubes, a rubber policeman, 500 ml flask, and 8 centrifuge tubes on ice. Get a large waste bucket/beaker*
- Wash suspension
  - Discard supernatant and add about 5 ml BBY-2 buffer to each bottle and resuspend with rubber policeman. Rinse the tubes with the buffer. Homogenize and then pour in 8 centrifuge tubes. Fill each tube to 40 ml mark with BBY-2 buffer.
- Second spin
  - Spin 10 min @ 12,000 ×g.
  - *During spin, clean homogenizer and tubes, put them and BBY-3 buffer on ice. Have a 250 ml flask with a stir bar on ice on a stir plate, ready for incubation.*
- Triton buffer suspension
  - WORK UNDER GREEN LIGHT. Discard supernatant. Use about 50 ml or less BBY-3 buffer to resuspend the pellet. The concentration should be more than 2 mg/ml to allow for Triton X-100 addition. Homogenize, rinse tubes and homogenizer with BBY-3 buffer. Measure the volume of the sample.
  - First concentration measurement
    - Measure out four 2.5 ml batches of 80% aqueous buffered acetone. Dissolve 5 μL of sample in three out of four batches (about 500x dilution), using a new pipetter tip every time and wiping the tip with a kimwipe before dispensing. Vortex mix and transfer 1.5 ml to a 2 ml Eppendorff tube. Centrifuge at $1,300 \times g$ for 3 minutes. Measure the absorption spectrum in a 1 cm cuvette at 647 nm, 664 nm and 750 nm. The chlorophyll extinction coeffcients are taken from[3] and are

given by

$$Chl_a = \quad -2.85A_{647\,nm} \quad +13.71A_{664\,nm} \quad (1.1)$$
$$Chl_b = \quad 22.39A_{647\,nm} \quad -5.42A_{664\,nm} \quad (1.2)$$
$$Total\ Chl = \quad 19.54A_{647\,nm} \quad +8.29A_{664\,nm} \quad (1.3)$$

- Calculate the concentration of BBY-3T buffer to add such that the final ratio is 25 mg Triton per mg chlorophyll with a final chlorophyll concentration of 2 mg/ml.
- Incubation with 25% Triton X-100 detergent
  - Pour homogenized sample into flask on ice with stir bar and add the volume of BBY-3 buffer calculated above. Now, with plastic pipette, carefully, slowly, steadily and drop by drop add the BBY-3T volume determined in the calculation into the flask while stirring on ice at medium speed. Incubation time is 28 min starting from the addition of the first drop. Keep the sample in the dark.
  - *During incubation, clean homogenizer and tube, and put them on ice with 12 centrifuge tubes, as well as buffer A.*
- Third spin
  - Pour sample into centrifuge tubes immediately following end of incubation.
  - Spin 30 min @ 48,000 ×g
- Fourth spin (starch removal)
  - Discard supernatant (PSI are now removed, the chlorophyll amount is now 40-50% that of sample before triton spin) and resuspend pellets with buffer A. Homogenize with 30 ml homogenizer and dilute to fill up four centrifuge tubes (160 ml).
  - Spin 5 min @ 2,000 ×g.
- Fifth spin
  - Retain supernatant. Pour sample into 4 new centrifuge tubes (only starch will be in pellets).
  - Spin 30 min @ 48,000 ×g.
  - *During spin, prepare for concentration measurement. Label and chill 6-8 storage vials. Put homogenizer and tube on ice.*
- Final resuspension
  - Discard supernatant and resuspend pellets in small amount of storage buffer. Homogenize and measure concentration of homogenate with spectrophotometer as before. Measure the total volume of sample and calculate total amount of chlorophyll. Adjust the concentration with storage buffer A such that the final concentration is 3 mg/ml.
- Storage
  - Pour a small amout of liquid nitrogen into a styrofoam container and put a cheesecloth in the liquid nitrogen. Dispense sample drop-by-drop (100 μl) into the liquid nitrogen. After all of the sample is flash-frozen, take out the cheese cloth and transfer the BBY droplets into Falcon tubes and store at −80 °C.
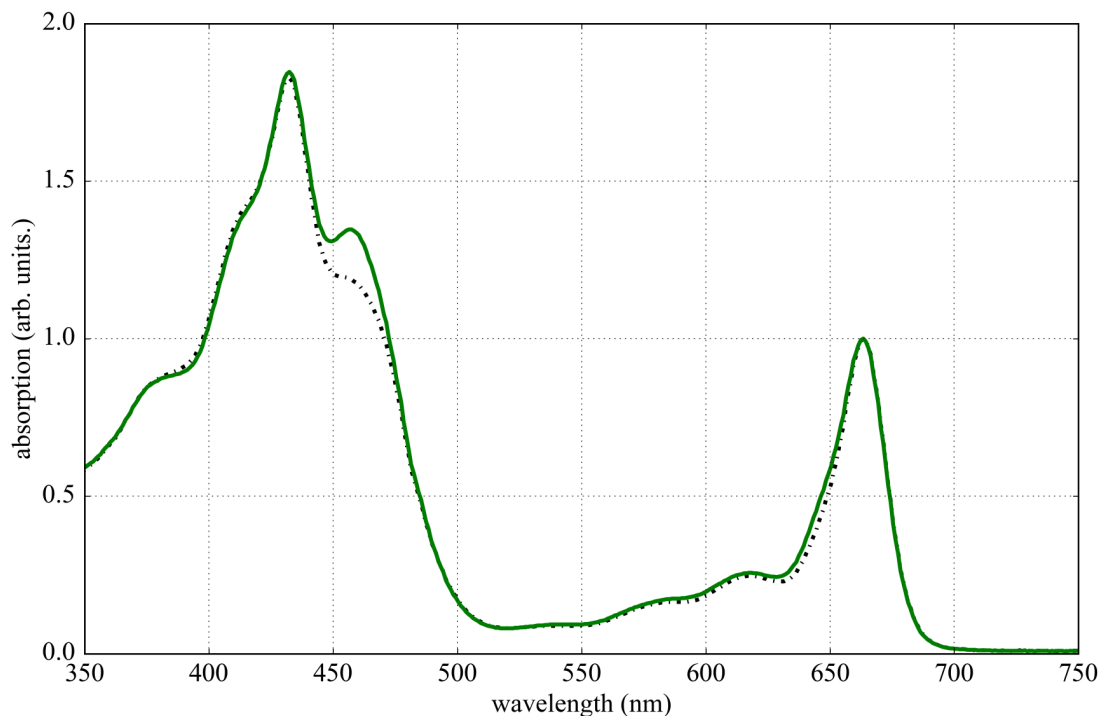
**Figure A.1** Typical BBY absorption spectra measured after 80% aqueous acetone extraction at room temperature as described above. The dashed line corresponds to step 1 of the extraction procedure; step 2 is marked by the solid line. Both spectra have been normalized to the peak absorption at 663 nm.

### A.4  *Photosystem II RC Preparation*

The buffers without beta-DM may be prepared in advance and stored at 4 °C. The buffers containing beta-DM must be made the day of the preparation and not stored. Column is packed according to manufacturer instructions and washed with several column volumes of distilled water, and then equilibrated with 10 CVs of A-beta.

- Thawing BBY
    - Thaw 15 mg Chl of sample in 15 ml Falcon tube by placing it into a beaker with tap water for 5 minutes. Dilute to 15 ml with A-beta in 30 ml homogenizer. Homogenize.
- BBY Wash
    - Transfer sample to 40 ml centrifuge tube and spin at 3,000 ×g at 4 °C for 3 min. Retain supernatant.
    - Dilute supernatant with A-beta in 40 ml centrifuge tube and spin at 48,000 ×g for 30 min. Retain pellet. Resuspend pellet to original concentration (5 ml) and homog-

enize in 10 ml homogenizer.

- BBY Solubilization
  - Transfer sample to 50 ml Erlenmeyer flask with small stir bar in it. Dilute sample with 2 ml of A-beta. Add 1 ml of X to sample dropwise with a pipette. Incubate at room temperature in the dark for 25 minutes. The final concentrations of reagents are 1.25% beta-DM and 1.75 mg Chl/mL[2].
  - Load sample into 10 ml centrifuge tube and spin at 48,000 ×g for 20 minutes at 4 °C. Retain supernatant. Store on ice.
- Sample loading
  - Load sample onto equilibrated column in 4 C cold room at a flowrate of 0.1 CV/min.
- Antennae wash
  - Wash column with A-beta until the absorption ratio of $A_{675\,nm}/A_{650\,nm}$ is greater than 3, which should take about 50 minutes at a flowrate of 0.5 CV/min. At this point, one could elute the sample with A-beta + 75 mM MgSO$_4$. *This is the PSII Core preparation.*
- Buffer exchange and Triton treatment
  - Rinse column with 5 CVs of B-beta at the same flow rate. This should take about 20 minutes. Elute all of the sample off of the column using B-beta + 75 mM MgSO$_4$. Dilute the resulting volume ten-fold using 25% (w/w) Triton X-100 in B-beta and incubate for 30 minutes while stirring gently.
- Load treated sample
  - Wash column with B-beta until flow is clean and absorption at 280 nm disappears. This takes about an hour.
- RC elution
  - Elute sample with C2-beta. Collect 1.5 ml fractions. Measure the absorption spectrum of each fraction and calculate the $A_{417\,nm}/A_{435\,nm}$ ratio. It should be 1.20[4]. It is critical that the spectrometer you use is calibrated. Pool the fractions that have the ideal ratio.
- Buffer exchange and sample concentration
  - Transfer sample to 30 kDa centrifugal filters and wash with Dx2-beta. Spin at 6,500 ×g at 4 °C. Repeat until sample volume is about 200 µl.
  - If making 2DESS samples, concentrate in 2 ml 30 kDA filters until retained volume is about 50 µl.
  - Measure UV-VIS spectrum by taking 2 µl of sample and diluting it in 1 ml of Dx2-beta ( 500-fold dilution). Dilute sample with Dx2-beta such that the optical density in 1 cm is about 0.6.
  - Dilute 1 : 1 in ethylene-glycol glycerol mixture and store in liquid nitrogen until use.

## A.5   Troubleshooting

- Sample constantly shows a ratio higher or lower
  - Check calibration of UV-VIS spectrometer
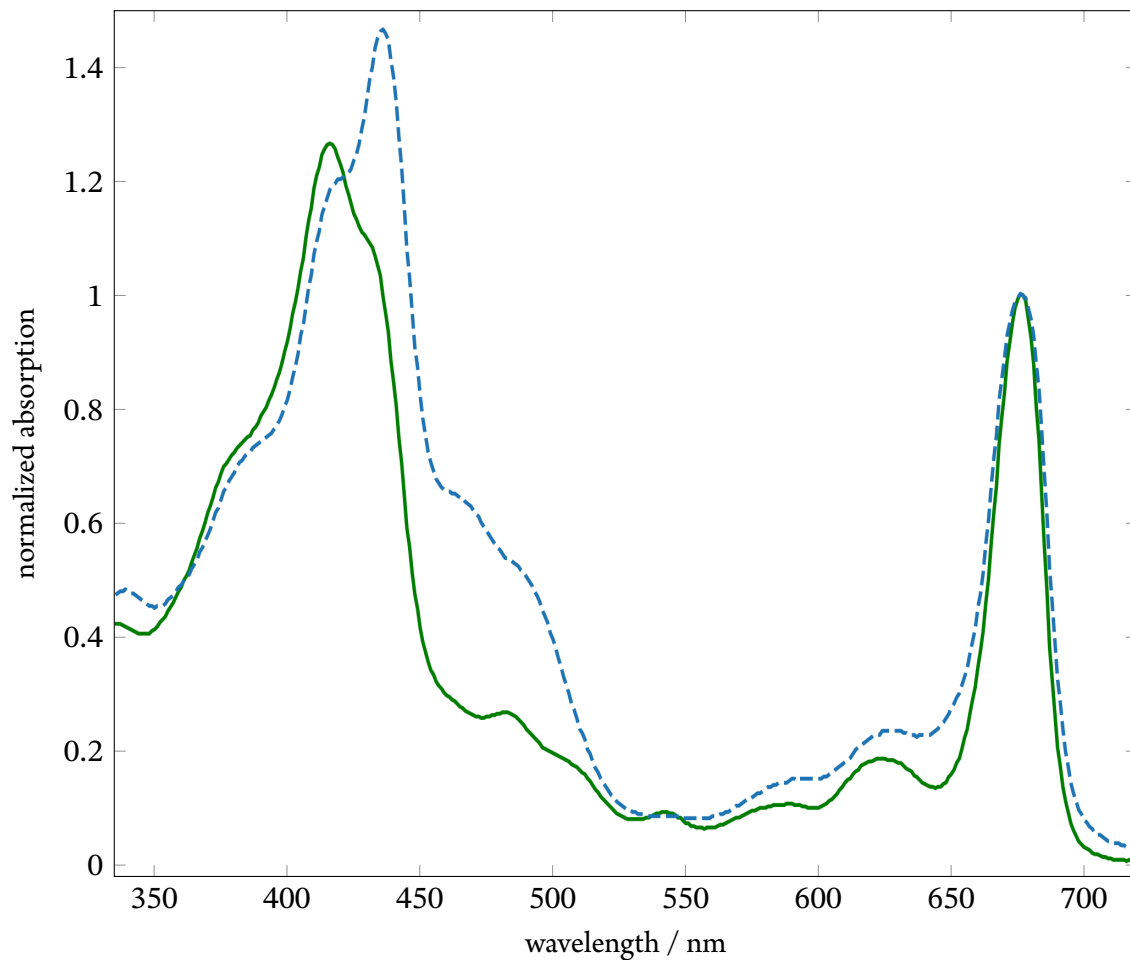
**Figure A.2** Typical absorption spectra of photosystem II core (dashed) and reaction center (solid) preparations. Both are taken at room temperature in buffer and normalized to 675 nm.

- - Increase or decrease Triton treatment volume
- Sample does not elute off of the column
  - Check that beta-DM is fresh. It loses effectiveness and will cause sample to percipitate out of solution on the column.

*References*

1. D. A. Berthold et al.: A Highly Resolved, Oxygen Evolving Photosystem II Preparation from Spinach Thylakoid Membranes. Federation of European Biochemical Societies Letters **134**(2) (1981), 231–234.

2. P. J. van Leeuwen et al.: Rapid and simple isolation of pure photosystem II core and reaction center particles from spinach. Photosynthesis Research **28**(3) (1991), 149–153. doi: 10.1007/BF00054128.

3. R. J. Porra et al.: Determination of accurate extinction coefficients and simultaneous equations for assaying chlorophylls a and b extracted with four different solvents: verification of the concentration of chlorophyll standards by atomic absorption spectroscopy. BBA - Bioenergetics **975**(3) (1989), 384–394. doi: 10.1016/S0005-2728(89)80347-0.

4. C. Eijckelhoff et al.: Purification and spectroscopic characterization of photosystem II reaction center complexes isolated with or without Triton X-100. Biochemistry **35**(39) (1996), 12864–12872. doi: 10.1021/bi960991m.

# APPENDIX B
## ITO Etching Protocol

### *B.1   Introduction*

This document describes a procedure for safely etching Indium Tin Oxide (ITO) slides in an acid bath. The process involves immersing ITO slides in a 100 mL solution of 50% DI water, 45% hydrochloric acid, and 5% nitric acid at 70 °C. The slides are then cleaned with acetone and ethanol. This document includes information on safe handling and disposal of hydrochloric acid, nitric acid, and acetone, as well as a detailed procedure for preparing and etching ITO slides.

### *B.2   Potential Hazards*

*Nitric Acid*

- Routes of exposure: inhalation, eye contact, skin contact, ingestion.
- Can cause severe burns to eyes and skin. Fumes can cause respiratory tract burns.
- Exposure to high concentrations of nitric acid vapor may cause pneumonitis and pulmonary edema which may be fatal. Continued exposure to nitric acid vapor or mist may result in chronic bronchitis and pneumonitis.
- Extremely corrosive
- Oxidizer. Do not store near flammable chemicals or with other acids/bases. Do not dispose of nitric acid in waste containers containing acetone, various alcohols, dichloromethane, and many other organic substances, as this may result in fires or explosions.

*Hydrochloric Acid*

- Routes of exposure: inhalation, eye contact, skin contact, ingestion.
- Can cause severe burns to eyes and skin. Fumes can cause respiratory tract burns.
- Material is extremely destructive to the tissue of the mucous membranes and upper respiratory tract.
- Corrosive

*Acetone*

- Routes of exposure: inhalation, eye contact, skin contact, ingestion.

- Toxic to central nervous system. May be toxic to kidneys, reproductive system, liver, and skin. Repeated or prolonged exposure can produce target organ damage.
- Flammable liquid. Keep away from heat, sparks and flame.

## B.3  Procedure controls

*Engineering Controls*

- Nitric acid, hydrochloric acid, and acetone must be in a vent hood when it is not sealed closed.
- Procedures with acids and acetone must be performed in a vent hood with plenty of space. There should be no flammable chemicals stored in the vent hood.
- Acids should be stored away from flammable substances in a secondary container.
- Acetone should be stored in the flammables cabinet.
- An eyewash and safety shower must be available in the immediate work area for any work with nitric acid.

*Work Practice Controls*

- Procedures with acids should not be performed alone.
- Care should be taken to not spill acids or acetone while handling.
- Concentrated acid containers should be closed and stored immediately after the initial dilution.
- Acetone container should be closed and stored in the flammables cabinet immediately after use.
- Wash hands and change gloves after completing acid bath procedure. Use the proper gloves for acid handling (heavy chemical gloves, neoprene) and acetone handling (butyl).

*Protective Equipment*

- Heavy chemical gloves or neoprene gloves for acid handling, butyl gloves for acetone handling
- Safety Glasses
- Lab Coat
- Close-toed shoes

*Transportation and Storage*

Nitric acid and hydrochloric acid containers will be stored in a secondary container within the acid storage cabinet under the fume hood. Concentrated nitric acid will not be transported outside of the lab.

Acetone containers will be stored in the flammables cabinet. Keep away from direct sunlight and heat and avoid all possible sources of ignition.

*Waste Disposal*

Waste from the acid bath will be poured into an acid-safe, labeled waste container dedicated to nitric acid and hydrochloric acid. It will not be mixed in waste containers with other organic solvents, alcohols, or acids. Acetone will be disposed of in a separate waste container dedicated to acetone and nail polish. Do not mix the acetone with acids in a waste container.

*Exposure/Unintended Contact*

- Eyes: Get medical aid immediately. Remove contact lenses if worn. Do NOT allow victim to rub eyes or keep eyes closed. Extensive irrigation with water is required (at least 30 minutes).
- Skin: In case of contact, immediately flush skin with plenty of water for at least 15 minutes while removing contaminated clothing and shoes. Get medical aid immediately. Wash clothing before reuse.
- Ingestion: If swallowed, do NOT induce vomiting. Get medical aid immediately. If victim is fully conscious, give a cupful of water. Never give anything by mouth to an unconscious person.
- Inhalation: If inhaled, get medical aid immediately. Remove victim to fresh air. If not breathing, give artificial respiration. If breathing is difficult, give oxygen.

*Spill Procedure*

For minor acid spills ($>1$ L), immediately cover the spill with an excess of sodium bicarbonate. If possible, confine spill to a small area using a spill kit or absorbent material. Sweep/wipe up the sodium bicarbonate and dispose of it in a separate solid waste container that does not contain flammable material. Ventilate the area as well as possible, and avoid inhaling vapors. For large spills ($<1$ L), get emergency assistance by calling 911.

For minor acetone spills ($>1$ L), evacuate the area immediately, isolate the hazard area, and keep out unnecessary and unprotected personnel. Eliminate all ignition sources. Increase ventilation to area. Contain and soak up spill with non-reactive absorbent material. Place the contaminated absorbent in a covered, labelled solid waste container for disposal.

## B.4   Materials

- Heavy chemical gloves or neoprene gloves
- Butyl gloves
- Safety goggles
- Flame-resistant lab coat
- Nitric Acid

- Hydrochloric Acid
- Acetone
- Ethanol
- Nail polish
- Sodium bicarbonate powder
- Liquid waste container labeled for nitric acid and hydrochloric acid
- Solid waste container for cotton pads contaminated with acetone
- Pyrex casserole dish
- 150 mL glass beaker
- 50 mL glass beaker
- Glass volumetric pipettes, 50 mL and 5 mL
- Acid-safe Teflon tweezers
- Non-abrasive cotton pads (e.g. Webril Handi-pads)
- Digital multimeter

### B.5    Etching Procedure

- Lay 20 ITO slides on paper towels with the ITO side face-up. Check that each slide is face-up by measuring the resistance across the surface with a digital multimeter. The ITO side also has a blue reflective tint that can be seen by eye when viewed at a glancing angle to the light.
- Apply a single brush-stroke of nail polish through the center of each slide. Try to apply a thick, even coat. Allow the nail polish to dry for about 30 min.
- Apply a second coat of nail polish to each slide, and dry for 30 min.
- Place the slides in the Pyrex casserole dish with the nail polish side up. Place the casserole dish on a hot plate set to 70 °C inside the fume hood.
- Put on protective equipment for handling acid (neoprene gloves, goggles, lab coat).
- In the fume hood, mix the acid solution in a large beaker (150 mL). Using a glass volumetric pipette, add 50 mL of DI water. Then add 45 mL of hydrochloric acid, and 5 mL of nitric acid. Close and store acid containers immediately after use.
- Carefully pour the acid into the casserole dish, evenly covering the ITO slides. If some ITO slides float on the surface of the acid, lightly press them to the bottom of the dish using tweezers.
- After about 5 min, remove a slide with tweezers and check whether the ITO is completely etched away around the nail polish. If not, wait another 5 min.
- When the etching is complete, turn off the hot plate. Use the glass pipette to draw the acid out of the casserole dish, and put it in a waste container labeled for hydrochloric and nitric acid. Do not put the acid waste in a waste container with organic solvents.
- Neutralize the casserole dish and beaker by covering with an excess of baking soda. Place the casserole dish in the sink and fill with tap water. Neutralize the glass pipette by drawing in water and baking soda. Neutralize the tweezers and anything else that came in contact with the acid.

- Remove gloves and put on Butyl gloves for handling acetone.
- Put the dish back in the fume hood. Pour about 10 mL of acetone into a 50 mL beaker. Pour a small amount of acetone from the beaker onto a cotton pad and rub each slide until the nail polish is completely removed and the surface is clean. Lay the cleaned slides on paper towels inside the fume hood to dry. Dispose of used cotton pads in a solid waste container labeled for acetone.
- Clean the slides again with cotton pads and ethanol. Store them in a sealed, labeled glass container immersed in ethanol. Store the container away from sources of ignition.

## APPENDIX C

## 2DESS on TIPS-Pentacene Supplementary Information

### C.1   Fit to Linear Absorption

The linear absorption spectrum of $6,13-$ bis(triisopropylsilylethynyl pentacene) (TIPS pentacene) taken at 77 K was fit to a model $M$ of the form

$$M(\mathcal{E}; \text{param}) \equiv \sum_{i \in \{1,2\}} \text{PseudoVoigt}_i(\mathcal{E}; \mathcal{E}_{p_i}, A_i, \sigma_i, f_i)$$
$$+ \sum_{j \in \{3,4,5,6\}} \text{Lorentzian}_j(\mathcal{E}; \mathcal{E}_{p_j}, A_j, \sigma_j) + C \qquad (3.1)$$

where the dominant peaks at 1.93 eV and 1.96 eV were fit to the empirical pseudo-Voigt profile representing a transition that is both homogeneously and inhomogeneously broadened, and the rest of the features were modeled as Lorentzian lines. A constant baseline offset was included as well. It was found that using a pseudo-Voigt profile instead of a Lorentzian profile significantly improved the quality of the fit near the wings of the strongest features. Lorentzians were used for the remaining features because the signal-to-noise of those features was insufficient to resolve the differences between these two lineshapes at the wings. This model was fit using nonlinear least-squares using the Levenberg-Marquardt algorithm as implemented in the lmfit-py package[1]. The values of the fit parameters and the error bounds are shown in Table C.1.

### C.2   Fit to Stark Spectrum

To obtain a model for the Stark spectrum, derivatives of the Gaussian and Lorentzian lineshape functions were evaluated to second order. For completeness, they are listed below with the nor-

malization used in the fitting

$$G(\mathcal{E}; \mathcal{E}_p, A, \sigma) = \frac{A}{\sigma\sqrt{2\pi}} \exp\left(-\frac{(\mathcal{E} - \mathcal{E}_p)^2}{2\sigma^2}\right) \tag{3.2}$$

$$G'(\mathcal{E}; \mathcal{E}_p, A, \sigma) = -\frac{(\mathcal{E} - \mathcal{E}_p)}{\sigma^2} G(\mathcal{E}; \mathcal{E}_p, A\sigma) \tag{3.3}$$

$$G''(\mathcal{E}; \mathcal{E}_p, A, \sigma) = \frac{1}{\sigma^2}\left(\frac{(\mathcal{E} - \mathcal{E}_p)^2}{\sigma^2} - 1\right) G(\mathcal{E}; \mathcal{E}_p, A\sigma) \tag{3.4}$$

$$L(\mathcal{E}; \mathcal{E}_p, A, \sigma) = \frac{A}{\pi\sigma}\left(\frac{1}{1 + \frac{(\mathcal{E} - \mathcal{E}_p)^2}{\sigma^2}}\right) \tag{3.5}$$

$$L'(\mathcal{E}; \mathcal{E}_p, A, \sigma) = -\frac{2\pi(\mathcal{E} - \mathcal{E}_p)}{A\sigma} L(\mathcal{E}; \mathcal{E}_p, A, \sigma)^2 \tag{3.6}$$

$$L''(\mathcal{E}; \mathcal{E}_p, A, \sigma) = \left(\frac{8\pi^2(\mathcal{E} - \mathcal{E}_p)^2}{A^2\sigma^2} L(\mathcal{E}; \mathcal{E}_p, A, \sigma) - \frac{2\pi}{A\sigma}\right) L(\mathcal{E}; \mathcal{E}_p, A, \sigma)^2 \tag{3.7}$$

$$\text{PseudoVoigt}(\mathcal{E}; \mathcal{E}_p, A, \sigma, f) = (1 - f)G(\mathcal{E}; \mathcal{E}_p, A, \sigma_g) + fL(\mathcal{E}; \mathcal{E}_p, A, \sigma) \tag{3.8}$$

$$\text{PseudoVoigt}'(\mathcal{E}; \mathcal{E}_p, A, \sigma, f) = (1 - f)G'(\mathcal{E}; \mathcal{E}_p, A, \sigma_g) + fL'(\mathcal{E}; \mathcal{E}_p, A, \sigma) \tag{3.9}$$

$$\text{PseudoVoigt}''(\mathcal{E}; \mathcal{E}_p, A, \sigma, f) = (1 - f)G''(\mathcal{E}; \mathcal{E}_p, A, \sigma_g) + fL''(\mathcal{E}; \mathcal{E}_p, A, \sigma) \tag{3.10}$$

In these equations, $\mathcal{E}$ is the transition energy, $\mathcal{E}_p$ is the mean peak position, $A$ is the amplitude, $\sigma$ is the linewidth. For the pseudo-Voigt profile, the factor $f$ represents the fraction between the Lorentzian and Gaussian lineshapes, and $\sigma_g = \frac{\sigma}{\sqrt{2\log 2}}$ to ensure that the full-width at half-maximum of both lineshapes is the same. In performing the fit to the Stark data, only the amplitudes of the lineshapes were allowed to vary. The other parameters were held fixed at the best-fit values obtained from the fit to the linear absorption spectrum (see Figure C.1).

### *References*

1. M. Newville et al.: LMFIT: Non-Linear Least-Square Minimization and Curve-Fitting for Python. 2014. doi: http://doi.org/10.5281/zenodo.11813.

| Lineshape | Peak Parameter | Value | Standard Error |
|---|---|---|---|
| PseudoVoigt 1 | $\mathcal{E}_p$ (mean) | 1.927 eV | $1.48 \times 10^{-5}$ eV |
| | A (amplitude) | $1.653 \times 10^{-2}$ | $7.17 \times 10^{-5}$ |
| | $\sigma$ (linewidth) | $8.956 \times 10^{-3}$ eV | $2.26 \times 10^{-5}$ eV |
| | f (fraction) | $5.506 \times 10^{-1}$ | $9.94 \times 10^{-3}$ |
| PseudoVoigt 2 | $\mathcal{E}_p$ (mean) | 1.959 eV | $1.19 \times 10^{-4}$ eV |
| | A (amplitude) | $2.482 \times 10^{-3}$ | $6.77 \times 10^{-5}$ |
| | $\sigma$ (linewidth) | $8.582 \times 10^{-3}$ eV | $2.17 \times 10^{-4}$ eV |
| | f (fraction) | $9.300 \times 10^{-1}$ | $5.71 \times 10^{-2}$ |
| Lorentzian 3 | $\mathcal{E}_p$ (mean) | 2.072 eV | $1.37 \times 10^{-4}$ eV |
| | A (amplitude) | $3.175 \times 10^{-3}$ | $8.23 \times 10^{-5}$ |
| | $\sigma$ (linewidth) | $9.887 \times 10^{-3}$ eV | $2.41 \times 10^{-4}$ eV |
| Lorentzian 4 | $\mathcal{E}_p$ (mean) | 2.103 eV | $1.11 \times 10^{-4}$ eV |
| | A (amplitude) | $1.117 \times 10^{-2}$ | $1.19 \times 10^{-4}$ |
| | $\sigma$ (linewidth) | $1.728 \times 10^{-2}$ eV | $1.81 \times 10^{-4}$ eV |
| Lorentzian 5 | $\mathcal{E}_p$ (mean) | 2.249 eV | $1.73 \times 10^{-3}$ eV |
| | A (amplitude) | $1.497 \times 10^{-3}$ | $4.75 \times 10^{-4}$ |
| | $\sigma$ (linewidth) | $1.772 \times 10^{-2}$ eV | $2.69 \times 10^{-3}$ eV |
| Lorentzian 6 | $\mathcal{E}_p$ (mean) | 2.278 eV | $2.03 \times 10^{-3}$ eV |
| | A (amplitude) | $3.532 \times 10^{-3}$ | $6.01 \times 10^{-4}$ |
| | $\sigma$ (linewidth) | $2.547 \times 10^{-2}$ eV | $2.62 \times 10^{-3}$ eV |
| Constant baseline | c | $2.19 \times 10^{-2}$ | $4.31 \times 10^{-4}$ |

**Table C.1** Least-squares fit parameters obtained by fitting the linear absorption spectrum of TIPS-pentacene to the model described above.
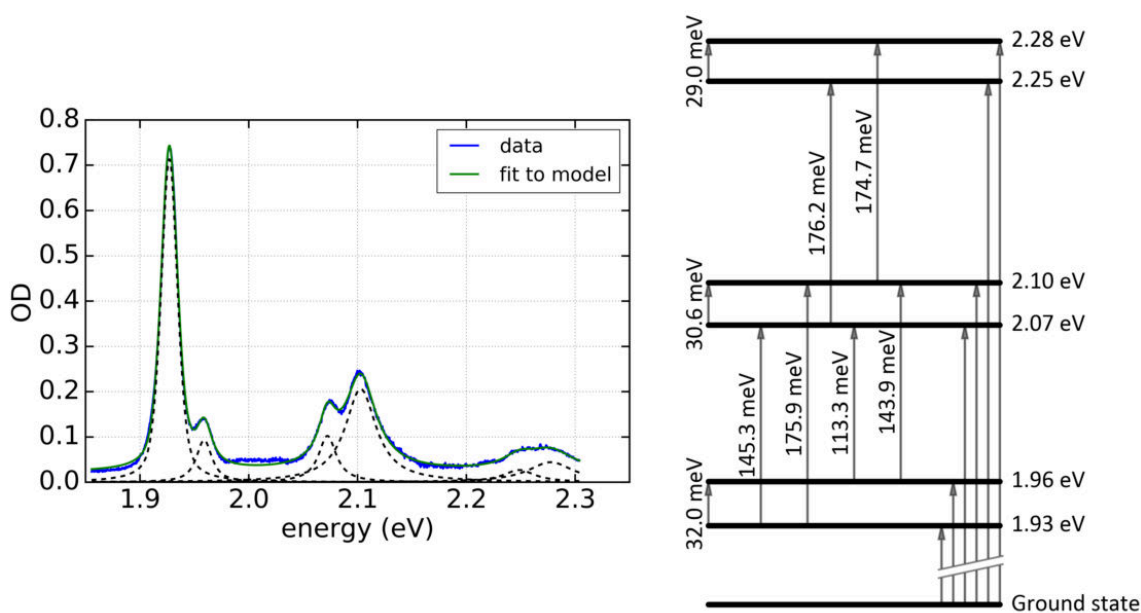
**Figure C.1** (left) fitting of the linear absorption spectrum of TIPS-pentacene. The data is shown in blue, the individual lineshapes are shown in dashed black, and the resultant model including a constant baseline offset is shown in green. (right) energy level diagram constructed from the best-fit mean peak positions.

| Lineshape | Peak Parameter | Value | Standard Error |
|---|---|---|---|
| PseudoVoigt 1 | d1 A (amplitude) | $3.41 \times 10^{-3}$ | $1.53 \times 10^{-5}$ |
| | d2 A (amplitude) | $2.89 \times 10^{-6}$ | $8.95 \times 10^{-8}$ |
| PseudoVoigt 2 | d1 A (amplitude) | $4.28 \times 10^{-4}$ | $1.83 \times 10^{-5}$ |
| | d2 A (amplitude) | $1.88 \times 10^{-7}$ | $9.24 \times 10^{-8}$ |
| Lorentzian 3 | d1 A (amplitude) | $8.63 \times 10^{-4}$ | $2.55 \times 10^{-5}$ |
| | d2 A (amplitude) | $6.84 \times 10^{-8}$ | $1.42 \times 10^{-7}$ |
| Lorentzian 4 | d1 A (amplitude) | $2.42 \times 10^{-3}$ | $5.97 \times 10^{-5}$ |
| | d2 A (amplitude) | $6.04 \times 10^{-6}$ | $5.83 \times 10^{-7}$ |
| Lorentzian 5 | d1 A (amplitude) | $4.80 \times 10^{-4}$ | $7.08 \times 10^{-5}$ |
| | d2 A (amplitude) | $3.41 \times 10^{-7}$ | $7.37 \times 10^{-7}$ |
| Lorentzian 6 | d1 A (amplitude) | $8.22 \times 10^{-4}$ | $1.26 \times 10^{-4}$ |
| | d2 A (amplitude) | $2.46 \times 10^{-6}$ | $1.99 \times 10^{-6}$ |

**Table C.2** A fit to the Stark spectrum to first and second derivatives of the lineshapes used in the linear absorption fit. As is seen from the parameter magnitudes, the fit is dominated by first derivatives, suggesting that the Stark signal of TIPS-pentacene in 3-methylpentane at 77 K is dominated by a change in polarizability rather than the presence of charge-transfer states.
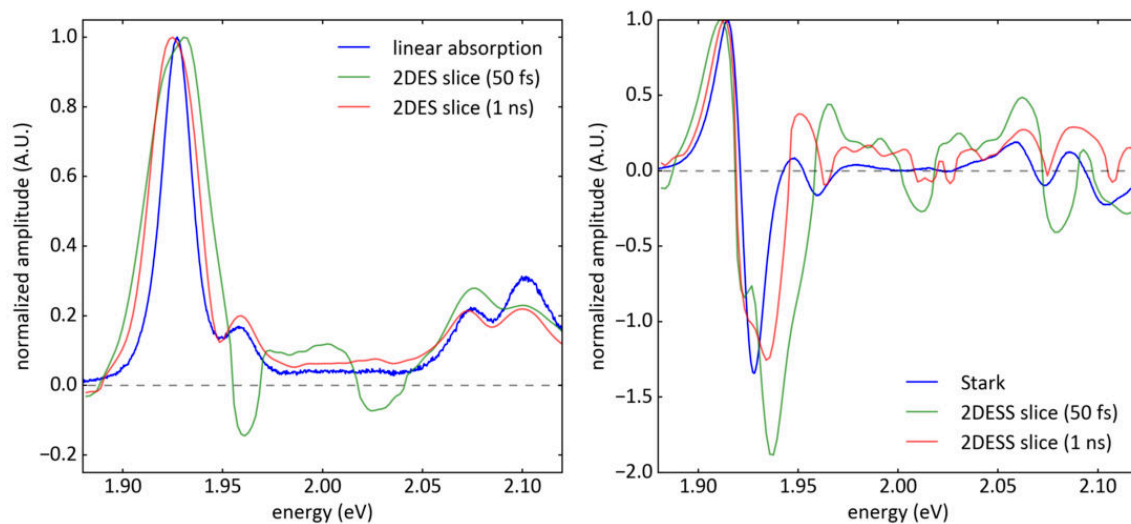
**Figure C.2** Comparison of a slice along the excitation-detection diagonal line of 2DES to linear absorption (left) and 2DESS to the Stark spectrum (right). The square-root of the absolute value of 2DES and 2DESS were taken and multiplied by the sign of the original data so that the traces have the same dependence on transition dipole moment as the linear and Stark data. All traces were then normalized to the maximum value. In both comparisons the diagonal slices taken from the 2D data show broader widths at early waiting times, likely indicating nonunitary processes such as energy transfer during the waiting time period. In the 2DES diagonal slice, small negative contributions may arise from excited state absorption at early times, causing deviations from the linear absorption.

## APPENDIX D
### Additional 2DESS Modeling Figures
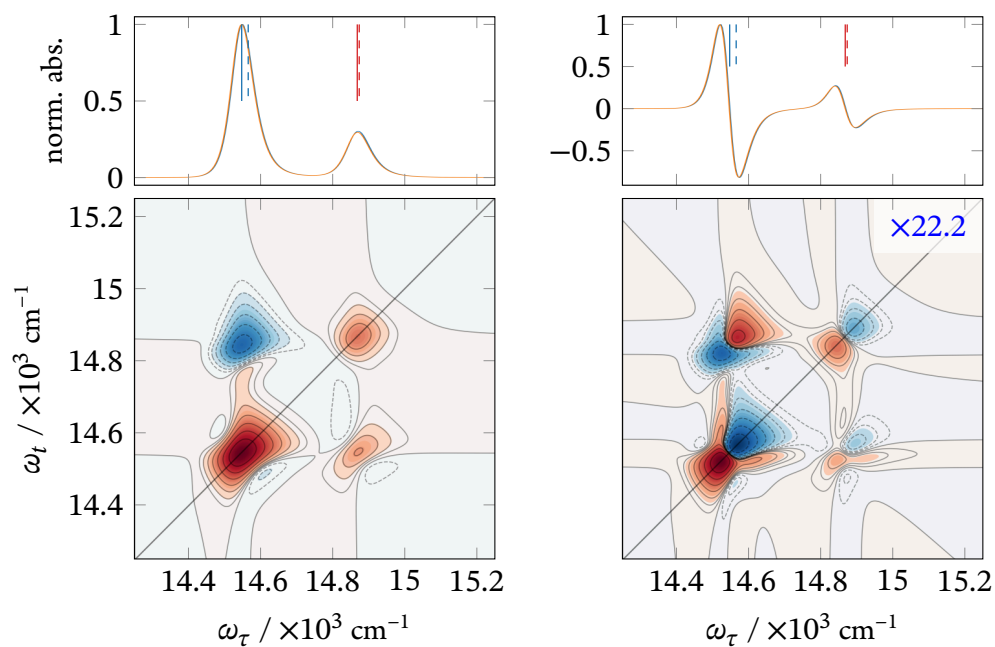


**Figure D.1** 2D and 2DESS spectra of $P_{D1}\,P_{D2}$ dimer calculated with $J_I$ spectral density and $\Delta\hat{\alpha}$ contribution only. The lower exciton position is shown in blue, shifting from 14,565 cm$^{-1}$ (solid) to 14,547 cm$^{-1}$ (dashed) upon coupling to the bath. The upper exciton (red) moves from 14,874 cm$^{-1}$ to 14,868 cm$^{-1}$.
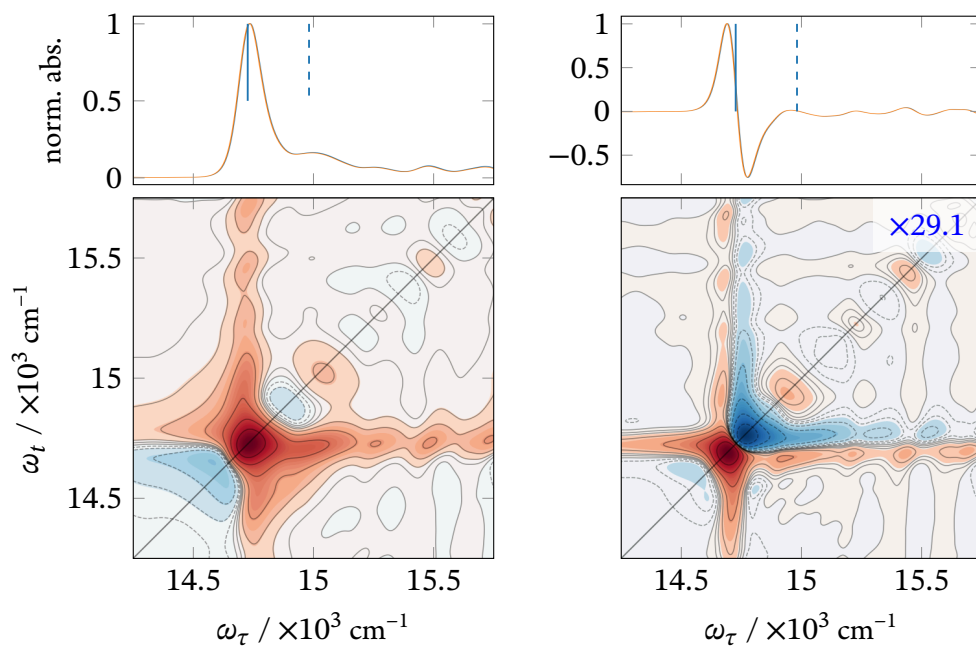
**Figure D.2** 2D and 2DESS spectra of $P_{D1}$ calculated with $J_{II}$ spectral density and $\Delta\widehat{\alpha}$ contribution only. The position of $P_{D1}$ is shown in blue. Upon coupling to the bath, the peak shifts from 14,982 cm$^{-1}$ to 14,726 cm$^{-1}$.
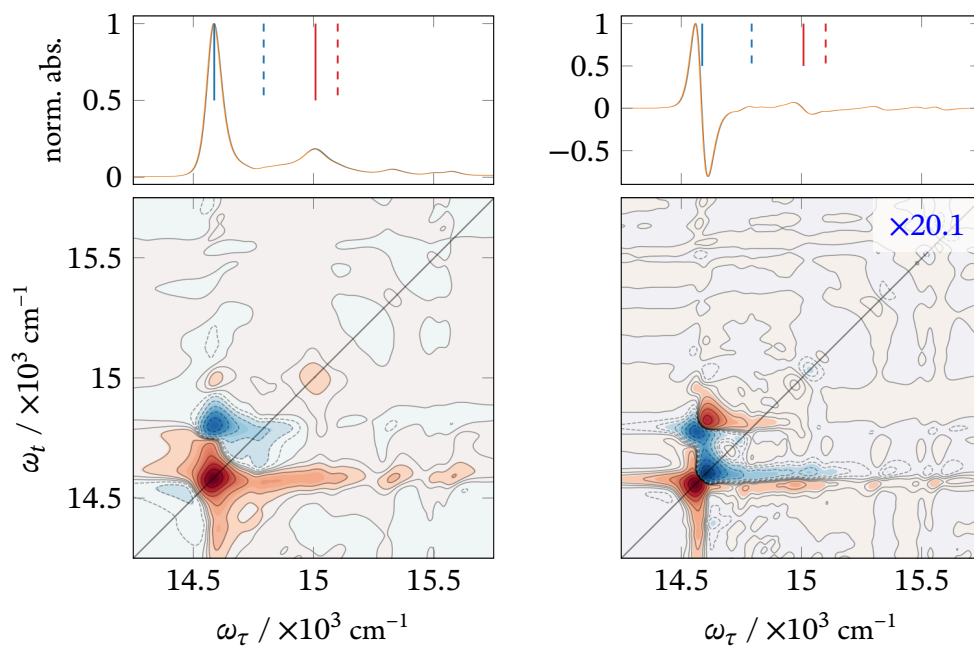
**Figure D.3** 2D and 2DESS spectra of $P_{D1}P_{D2}$ calculated with $J_{II}$ spectral density and $\Delta\hat{\alpha}$ contribution only. The lower exciton position is shown in blue, shifting from $14{,}793\,\mathrm{cm^{-1}}$ (solid) to $14{,}587\,\mathrm{cm^{-1}}$ (dashed) upon coupling to the bath. The upper exciton (red) moves from $15{,}100\,\mathrm{cm^{-1}}$ to $15{,}101\,\mathrm{cm^{-1}}$.